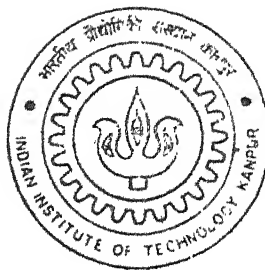


# **Investigation of Flow Past a Ram-Air Parachute**

**By**

**Anup Kumar Rai**



**DEPARTMENT OF AEROSPACE ENGINEERING**

**Indian Institute of Technology Kanpur**

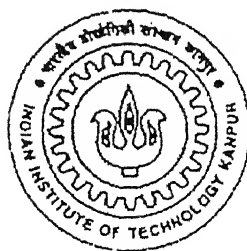
**MARCH, 2002**

# Investigation of Flow Past a Ram-Air Parachute

*A Thesis Submitted  
in Partial Fulfillment of the Requirements  
for the Degree of  
Master of Technology*

by

Anup Kumar Rai



Department of Aerospace Engineering  
Indian Institute of Technology, Kanpur

March, 2002

3 FEB 2003 / AE

पुष्पलाल काशीनाथ केनकर पुस्तकालय

भारतीय प्रौद्योगिकी संस्थान कानपुर

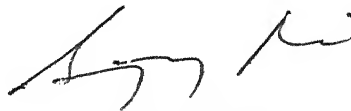
अवधि क्र० A-141802



A141802

## Certificate

This is to certify that the work contained in the thesis entitled "Investigation of Flow past a Ram-Air Parachute." by Mr. Anup Kumar Rai, Indian Institute of Technology, Kanpur, has been carried out under my guidance and it has not been submitted elsewhere for a degree.



Dr. Sanjay Mittal  
Associate Professor,  
Department of Aerospace Engineering,  
Indian Institute of Technology, Kanpur.

March 2002



# Acknowledgements

I take this opportunity to express my indebtedness and deep sense of gratitude to my thesis supervisor Dr. Sanjay Mittal for introducing me into the exciting field of CFD. His inspiring guidance, systematic approach and extensive care helped to shape my thesis as well as my personal attitude towards academics.

I am grateful to my colleagues in the CFD laboratory, namely, Satya Prakash, Vinod Guleria, Vikas Goel and Bhaskar for help I received from them on various occasions. I also thank all the people who have directly or indirectly helped in the completion of the thesis.

I extend my profound thanks to my friends Ayush Jha, Ashish Gupta, Gajendra Pandey, Dalton Maurya, Dhananjay Rao, Omprakash Seresta, Kapil Varshney and all of my friends at Hall-5, who have made my stay here a most memorable one.

Finally, I express my sincere gratitude to my parents and all family members for providing constant source of motivation and best wishes.

Anup Kumar Rai,  
Indian Institute of Technology, Kanpur,  
India.

# Contents

List of Figures	v
Abstract	xi
1 Introduction	1
1.1 Parachutes . . . . .	3
1.1.1 Ram Air Parachute . . . . .	4
1.1.2 Aerodynamics of Ram Air Parachute . . . . .	4
1.1.3 Construction of Ram Air Parachute . . . . .	5
1.1.4 Geometry of Ram Air Parachute . . . . .	5
1.2 Description of Problem . . . . .	6
1.3 Literature survey . . . . .	6
1.4 Thesis organization . . . . .	7
2 Numerical Technique and Procedure	8
2.1 Pre-processing . . . . .	9
2.1.1 Smoothing the Airfoil . . . . .	9

2.1.2	Mesh Generation . . . . .	9
2.2	Governing Equations . . . . .	12
2.3	Finite Element Formulation . . . . .	13
2.4	Turbulence Modeling . . . . .	14
2.4.1	Desirable features of Turbulence model . . . . .	15
2.4.2	Baldwin-Lomax Turbulence Model . . . . .	15
2.4.3	Simplification of Baldwin-Lomax Turbulence Model . . . . .	17
2.5	Boundary and Initial Conditions . . . . .	17
2.5.1	On Body Surface . . . . .	18
2.5.2	Inflow and Outflow Boundary Conditions . . . . .	18
2.5.3	Boundary Conditions on Side walls, Top and Bottom walls . . . . .	18
2.6	Numerical Procedure . . . . .	19
2.7	Post processing . . . . .	19
<b>3</b>	<b>Results and Discussions</b>	<b>21</b>
3.0.1	Flow past a LS(1)0417 airfoil . . . . .	23
3.0.2	Comparision between flow past Clarck-Y and LS(1)0417 airfoil . . .	25
3.0.3	Flow past ram-air parafoil . . . . .	25
3.0.4	Effect of the size and location of the leading edge cut. . . . .	29
3.1	Flow past a Ram-Air Parachute for $Re = 10^6$ . . . . .	30
3.1.1	Computational domain . . . . .	30
3.1.2	Boundary Condition . . . . .	30

---

3.1.3	Observations . . . . .	31
4	Conclusions	33
5	Scope for Future work	35
	Bibliography	37

# List of Figures

- 1 Flow past a LS(1) 0417 airfoil: a typical finite element mesh employed for computations and its close-ups at  $\alpha = 7.5^0$ . The mesh consists of 31,685 nodes and 63,024 triangular elements. . . . . 42
- 2  $\alpha = 7.5^0$ , laminar flow past a LS(1) 0417 airfoil: pressure(left), vorticity(right) fields from top to bottom  $Re = 500$ ,  $Re = 5000$  and  $Re = 10^4$ . . . 43
- 3  $Re = 10^6$ ,  $\alpha = 7.5^0$  turbulent flow past a LS(1) 0417 airfoil: close-up view of the finite element mesh, vorticity and pressure fields for steady state solution. . . . . 44
- 4  $\alpha = 15^0$  laminar flow past a LS(1) 0417 airfoil: pressure(left), vorticity(right) fields from top to bottom  $Re = 500$ ,  $Re = 5000$  and  $Re = 10^4$ . . . 45
- 5  $Re = 10^6$  turbulent flow past a LS(1) 0417 airfoil at  $\alpha = 15^0$ : pressure (left) and vorticity (right) fields during one cycle of the lift coefficient variation for the developed unsteady solution. . . . . 46
- 6  $\alpha = 17^0$ , laminar as well as turbulent flow past a LS(1) 0417 airfoil: pressure(left), vorticity(right) fields from top to bottom  $Re = 500$ ,  $Re = 5000$ ,  $Re = 10^4$  and  $Re = 10^6$ . . . . . 47
- 7  $Re = 10^6$  turbulent flow past a LS(1) 0417 airfoil at  $\alpha = 7.5^0$ ,  $15^0$ : time histories of the lift and drag coefficients and their power spectra. . . . . 48
- 8 Flow past a LS(1) 0417 airfoil: time histories of the lift and drag coefficients,  $Re = 10^4$  for  $0 \leq t \leq 30$ ,  $Re = 10^5$  for  $30 \leq t \leq 31.5$ ,  $Re = 10^6$  for  $31.5 \leq t \leq 42$ . The turbulence model was turned on at  $t = 30.0$ . . . . . 49

9	Flow past a LS(1) 0417 airfoil: time histories of the lift and drag coefficients, $Re = 10^4$ for $0 \leq t \leq 40$ , $Re = 10^5$ for $40 \leq t \leq 80$ , $Re = 10^6$ for $80 \leq t \leq 86$ . The turbulence model was turned on at $t = 40$ . . . . .	50
10	Flow past a ram-air parafoil with modified lower surface LS(1)0417 section: a typical finite element mesh employed for computations and its close-ups: The mesh consists of 21,409 nodes and 42,376 triangular elements $x_{cut} = 0.1c$ , $\theta_{cut} = 135^\circ$ . . . . .	51
11	$\alpha = 7.5^\circ$ flow past a ram air parafoil with modified lower surface LS(1) 0417 section: pressure(left), vorticity(right) fields from top to bottom $Re = 500$ , $Re = 5000$ and $Re = 10^4$ . . . . .	52
12	$Re = 10^4$ laminar flow past a ram air parafoil with modified lower surface LS(1)0417 section $x_{cut} = 0.1c$ and $\theta_{cut} = 135^\circ$ at $\alpha = 7.5^\circ$ : pressure (left) and vorticity (right) fields during one cycle of the lift coefficient variation for the developed unsteady solution. . . . .	53
13	$\alpha = 7.5^\circ$ flow past a ram air parafoil with modified lower surface LS(1) 0417 section: pressure(left), vorticity(right) fields from top to bottom $Re = 500$ , $Re = 5000$ and $Re = 10^4$ . . . . .	54
14	$Re = 10^4$ laminar flow past a ram air parafoil with modified lower surface LS(1)0417 section $x_{cut} = 0.1c$ and $\theta_{cut} = 135^\circ$ at $\alpha = 15^\circ$ : pressure (left) and vorticity (right) fields during one cycle of the lift coefficient variation for the developed unsteady solution. . . . .	55
15	$Re = 10^4$ laminar flow past a ram air parafoil with modified lower surface LS(1)0417 section $x_{cut} = 0.1c$ and $\theta_{cut} = 135^\circ$ at $\alpha = 7.5^\circ, 15^\circ$ : time histories of the lift and drag coefficients and their power spectra. . . . .	56
16	$Re = 10^6$ turbulent flow past a ram air parafoil with modified lower surface LS(1)0417 section $x_{cut} = 0.1c$ and $\theta_{cut} = 135^\circ$ at $\alpha = 7.5^\circ$ : pressure (left) and vorticity (right) fields during one cycle of the lift coefficient variation for the developed unsteady solution. . . . .	57

- 17  $Re = 10^6$  turbulent flow past a ram air parafoil with modified lower surface LS(1)0417 section  $x_{cut} = 0.1c$  and  $\theta_{cut} = 135^\circ$  at  $\alpha = 7.5^\circ$ : pressure (left) and vorticity (right) fields during one cycle of the lift coefficient variation for the developed unsteady solution. . . . . 58
- 18  $Re = 10^6$  turbulent flow past a ram air parafoil with modified lower surface LS(1)0417 section  $x_{cut} = 0.1c$  and  $\theta_{cut} = 135^\circ$  at  $\alpha = 7.5^\circ$ : pressure (left) and vorticity (right) fields during one cycle of the lift coefficient variation for the developed unsteady solution. . . . . 59
- 19  $Re = 10^6$  turbulent flow past a ram air parafoil with modified lower surface LS(1)0417 section  $x_{cut} = 0.1c$  and  $\theta_{cut} = 135^\circ$  at  $\alpha = 15^\circ$ : pressure (left) and vorticity (right) fields during one cycle of the lift coefficient variation for the developed unsteady solution. . . . . 60
- 20  $\alpha = 7.5^\circ$ , laminar flow past a ram air parafoil LS(1) 0417 section: pressure(left), vorticity(right) fields from top to bottom  $Re = 500$ ,  $Re = 5000$  and  $Re = 10^4$ . . . . . 61
- 21  $Re = 10^6$  turbulent flow past a ram air parafoil with LS(1)0417 section  $x_{cut} = 0.05c$  and  $\theta_{cut} = 135^\circ$  at  $\alpha = 7.5^\circ$ : pressure (left) and vorticity (right) fields during one cycle of the lift coefficient variation for the developed unsteady solution. . . . . 62
- 22  $\alpha = 15^\circ$ , laminar flow past a ram air parafoil with LS(1) 0417 section: pressure(left), vorticity(right) fields from top to bottom  $Re = 500$ ,  $Re = 5000$  and  $Re = 10^4$ . . . . . 63
- 23  $Re = 10^6$  turbulent flow past a ram air parafoil with LS(1)0417 section  $x_{cut} = 0.05c$  and  $\theta_{cut} = 135^\circ$  at  $\alpha = 15^\circ$ : pressure (left) and vorticity (right) fields during one cycle of the lift coefficient variation for the developed unsteady solution. . . . . 64
- 24  $Re = 10^6$  turbulent flow past a ram air parafoil with modified lower surface LS(1)0417 section  $x_{cut} = 0.1c$  and  $\theta_{cut} = 135^\circ$  at  $\alpha = 7.5^\circ, 15^\circ$ : time histories of the lift and drag coefficients and their power spectra. . . . . 65

- 25  $Re = 10^6$  turbulent flow past a ram air parafoil with LS(1)0417 section  $x_{cut} = 0.05c$  and  $\theta_{cut} = 135^\circ$  at  $\alpha = 7.5^\circ, 15^\circ$ : time histories of the lift and drag coefficients and their power spectra. . . . . 66
- 26  $Re = 10^6$  turbulent flow past a ram air parafoil with LS(1)0417 section at  $\alpha = 7.5^\circ$ : time histories of the lift and drag coefficients and their power spectra for modified lower surface and exact LS(1)0417 for two configuration of leading edge cut. . . . . 67
- 27 Flow past a ram-air parafoil with modified lower surface LS(1)0417 section  $x_{cut} = 0.1c$ ,  $\theta_{cut} = 135^\circ$ : time histories of the lift and drag coefficients,  $Re = 10^3$  for  $0 \leq t \leq 50$ ,  $Re = 5 \times 10^3$  for  $50 \leq t \leq 70$ ,  $Re = 10^4$  for  $70 \leq t \leq 90$ ,  $Re = 5 \times 10^4$  for  $90 \leq t \leq 130$ ,  $Re = 10^5$  for  $130 \leq t \leq 170$ ,  $Re = 10^6$  for  $170 \leq t \leq 198$ . The turbulence model was turned on at  $t = 90.0$ . . . . . 68
- 28 Flow past a ram-air parafoil with modified lower surface LS(1)0417 section  $x_{cut} = 0.1c$ ,  $\theta_{cut} = 135^\circ$ : time histories of the lift and drag coefficients,  $Re = 5 \times 10^2$  for  $0 \leq t \leq 50$ ,  $Re = 10^3$  for  $50 \leq t \leq 100$ ,  $Re = 5 \times 10^3$  for  $100 \leq t \leq 150$ ,  $Re = 10^4$  for  $150 \leq t \leq 200$ ,  $Re = 10^5$  for  $200 \leq t \leq 210$ ,  $Re = 10^6$  for  $210 \leq t \leq 235$ . The turbulence model was turned on at  $t = 200.0$ . . . . . 69
- 29 Flow past a ram-air parafoil with LS(1)0417 section  $x_{cut} = 0.05c$ ,  $\theta_{cut} = 135^\circ$ : time histories of the lift and drag coefficients,  $Re = 5 \times 10^2$  for  $0 \leq t \leq 50$ ,  $Re = 10^3$  for  $50 \leq t \leq 100$ ,  $Re = 10^4$  for  $100 \leq t \leq 150$ ,  $Re = 10^5$  for  $150 \leq t \leq 163$ ,  $Re = 10^6$  for  $163 \leq t \leq 190$ . The turbulence model was turned on at  $t = 150.0$ . . . . . 70
- 30 Flow past a ram-air parafoil with  $x_{cut} = 0.05c$ ,  $\theta_{cut} = 135^\circ$ : time histories of the lift and drag coefficients,  $Re = 5 \times 10^2$  for  $0 \leq t \leq 50$ ,  $Re = 10^3$  for  $50 \leq t \leq 100$ ,  $Re = 5 \times 10^3$  for  $100 \leq t \leq 150$ ,  $Re = 10^4$  for  $150 \leq t \leq 190$ ,  $Re = 10^5$  for  $190 \leq t \leq 200$ ,  $Re = 10^6$  for  $200 \leq t \leq 204$ . The turbulence model was turned on at  $t = 190.0$ . . . . . 71



31	$Re = 10^6$ turbulent flow past a ram-air parafoil with LS(1)0417 section and with modified lower surface at $\alpha = 7.5^0$ : variation of the pressure coefficient along the outer surface of the parafoil corresponding to the peak value of the lift coefficient for two configurations of the leading edge cut. . . . .	72
32	Flow past a Five cell ram-air parachute with Clarck-Y section: a typical 2D section of the finite element mesh employed for the computations and its close-up view at $\alpha = 7.5^0$ , each 2D section consists of 5,821 nodes and 11,410 triangular elements. The 3D mesh consists of 2,36,721 nodes and 4,56,400 wedge elements. . . . .	73
33	Top view and front view of mesh for five cell Ram-air parachute. . . . .	74
34	Five cell Ram-air parachute lying in a rectangular box. . . . .	75
35	3D view of Five cell Ram-air parachute: mesh on the parachute fabric. . .	76
36	$Re = 10^6$ turbulent flow past a Five cell ram-air parachute with Clarck-Y section: pressure(left) and z-vorticity(right) at mid span, quarter span, wing tip and close to wing tip away from the parachute surface. . . . .	77
37	$Re = 10^6$ turbulent flow past a Five cell ram-air parachute with Clarck-Y section: pressure(left) and x-vorticity(right) at various y-z sections. The location of the various section from top to bottom are $x/c=0.1, 0.5, 1.0, 2.0$ and $3.0$ . The origin is located at the leading edge of basic airfoil without cut. . . . .	78
38	$Re = 10^6$ turbulent flow past a Five cell ram-air parachute with Clarck-Y section: magnitude of velocity(left) and magnitude of vorticity(right) at various y-z sections. The location of the various section from top to bottom are $x/c=0.1, 0.5, 1.0, 2.0$ and $3.0$ . The origin is located at the leading edge of basic airfoil without cut. . . . .	79
39	$Re = 10^6$ turbulent flow past a Five cell ram-air parachute with Clarck-Y section: y-vorticity(left) and z-vorticity(right) at various y-z sections. The location of the various section from top to bottom are $x/c=0.1, 0.5, 1.0, 2.0$ and $3.0$ . The origin is located at the leading edge of basic airfoil without cut. . . . .	80

- 40  $Re = 10^6$  turbulent flow past a Five cell ram-air parachute with Clarck-Y section: at various 2D span wise sections: variation of the pressure coefficient along the outer surface of the parafoil. . . . . 81
- 41  $Re = 10^6$  turbulent flow past a Five cell ram-air parachute with Clarck-Y section at various 2D chord wise sections: variation of the pressure coefficient along the outer surface of the parachute. . . . . 82
- 42  $Re = 10^6$  turbulent flow past a five cell ram-air parachute with Clarck-Y section: time histories of lift and drag coefficients and lift/drag ratio. . . . 83
- 43  $Re = 10^6$  turbulent flow past a five cell ram-air parachute with Clarck-Y section: isosurface corresponding to magnitude of velocity = 0.95. . . . . 84
- 44  $Re = 10^6$  turbulent flow past a five cell ram-air parachute with Clarck-Y section: isosurface corresponding to x-vorticity = 2.00. . . . . 84
- 45  $Re = 10^6$  turbulent flow past a five cell ram-air parachute with Clarck-Y section: magnitude of velocity and parachute surface. . . . . 85
- 46  $Re = 10^6$  turbulent flow past a five cell ram-air parachute with Clarck-Y section: pressure and parachute surface. . . . . 86
- 47  $Re = 10^6$  turbulent flow past a five cell ram-air parachute with Clarck-Y section, parachute fabric and shedding on y-z section plane away from the parachute surface, for various componenets: Left from top to bottom, magnitude of velocity, x-velocity, y-velocity, z-velocity, and Right from top to bottom pressure, x-vorticity, y-vorticity, z-vorticity. . . . . 87

# Abstract

This thesis reports computational results for 2-D as well as 3-D turbulent flows past a Ram-air Parachute. The incompressible Reynolds averaged Navier Stokes equations, in conjunction with Baldwin-Lomax model for turbulence closure are solved using stabilized finite element formulations. The finite element mesh consists of a structured mesh close to the body and an unstructured part generated using Delaunay triangulation away from the body. The mesh, in 3D is generated by stacking, along the spanwise direction, 2D grids that have been obtained via a mesh generator already available. The points lying on the parachute surface are moved by appropriate amount so that surface resembles the final shape of the parachute. Linear elasticity equations are utilized to relocate the rest of the points in the 3D volume mesh. A simplified version of the Baldwin-Lomax model is utilized in 3D. Results have been presented for 2D,  $Re = 10^6$  flow past a LS(1)0417 airfoil at angle of attack  $7.5^\circ$  and  $15^\circ$ . The leading edge cut is an important design parameter for the ram-air parachute. Different cut configurations for the LS(1)0417 airfoil have been studied. Results have been presented for  $Re = 10^6$  flow past a five-cell Ram-Air parachute with leading edge cut at  $\alpha = 7.5^\circ$ . Computations for both laminar and turbulent flows have been carried out. It is observed that for the same leading edge cut configuration, the Clark-Y section results in higher lift-to-drag ratio value than the LS(1)0417 section. While the 2D flow with the Clark-Y section results in an unsteady flow, the 3D computations show a steady flow. Compared to the 2D flow, the 3D flow is associated with a lower lift to drag ratio. Perhaps, it is the wing tip vortices that are responsible for that effect.

# Chapter 1

## Introduction

Computational Fluid Dynamics(CFD) is judicial combination of fluid dynamics, applied mathematics, numerical methods and computer programming. It has made tremendous advancement in recent times, particularly in last two decades. Many complex problems of fluid dynamic related to turbulence, transition and separation can be solved using computers. CFD is a separate distinctive form supplementing both experimental fluid dynamics and theoretical fluid dynamics with its own technique. It has its own difficulties offering new perspective in the study of physical process.

During the past thirty years software has been developed for hierarchy of approximations of Navier-Stokes equations. Begining at the the simplest end of linear potential formulations, useful developments have taken place in solution of non linear full potential equations, in solution of Euler equations and, at the other complex extremes, in the solution of Reynolds-Averaged Navier-Stokes equations. The recent growth in speed and memory of computers, particularly in last five years, coupled with the growth in parallel architectures and algorithms, have even made possible achievements in Large Eddy Simulation (LES) for modest geometry and even the ultimate possibility of Direct Numerical Simulation (DNS) for the simplest of geometries.

For the design of all such vehicles the knowledge of forces and moments acting on the vehicle is absolutely indispensable. While these can also be determined experimentally, there are three compelling motivations for vigorous pursuit of CFD. *Firstly*, wind tunnel have rarely been able to simulate flight Reynolds No. and it is also subjected to wall and support interferences. *Secondly*, wind tunnel consumes large amount of energy which

impose a significant restrictions in coming years. *Thirdly*, experimental methods proved to be very expensive regarding cost and time to generate data even on limited variants of alternate or slightly changed vehicle configurations. If many variants are to be tried, time and money becomes unaffordable. Also it is difficult to attract and retain personal willing to do experiments.

From all the above we can say that this branch of scientific computing which is popularly known as *Computational Fluid Dynamics* has emerged as important design tool because of the rapid development in the available computing power, adaptability and above all low cost. Due to these features CFD finds its tremendous applications in research as well as in various industries such as *Aerospace, Automobile, Industrial manufacturing, Civil engineering, environmental, navel architecture* etc.

In all real flow situations the physical laws of conservation applies. These refer to conservations respectively of mass, momentum and energy. The equation of state completes the set which needed to be solved if some or all parameters controlling the flow are unknown. These laws can be expressed in terms of basic mathematical equations. These equations in their most general form are either integral equations or partial differential equations.<sup>1</sup>

1. Mass Conservation Equation:

$$\frac{\partial \rho}{\partial t} + \frac{\partial}{\partial x_j} (\rho u_j) = 0 \quad (1.1)$$

2. Momentum Conservation Equation:

$$\frac{\partial (\rho u_i)}{\partial t} + \frac{\partial}{\partial x_j} (\rho u_j u_i + p \delta_{ij} - \tau_{ij}) = 0 \quad (1.2)$$

3. Energy Conservation Equation:

$$\frac{\partial e}{\partial t} + \frac{\partial}{\partial x_j} [u_j (e + p) - u_i \tau_{ij} - q_{ij}] = 0 \quad (1.3)$$

4. Equation of state:

$$p = \rho R t \quad (1.4)$$

---

<sup>1</sup>We will use only incompressible flow equations for this thesis.

If a real flow can be "modelled" by a similar but simplified system then degree of complexity in handling the resulting equations may be considerably reduced. Historically, the lack of mathematical tools available to the engineers necessitates that considerable simplified assumptions should be made. These simplifications depends upon particular problem but are not arbitrary. In fact judgment is required to decide which parameter in flow process might be reasonably ignored, at least to the first approximation.

The basic philosophy behind CFD is to replace the integrals or partial derivatives in the governing equations with algebraic form. These algebraic equations are solved to obtain the value of various flow field variables at discrete points in time and space. There are three most common discretization techniques namely, *Finite difference methods*, *Finite volume methods*, *Finite element methods*. The activity in CFD is studied under three headings *Pre-processing*, *Processing*, *Post-Processing*. Pre-Processing involves discretization of solution domain( Grid generation) and proper implementations of boundary conditions. In Processing, governing equations are discretized into algebraic equations and solution is obtained at grid points by solving matrix system. Lastly, Post-processing involves analysis of obtained solution to obtain some important aerodynamic coefficients like  $C_d$ ,  $C_l$ . For all this one should have thorough knowledge of both computer programming and physics of problem. Apart from this good mathematical and geometrical knowledge are required for preprocessing. Processing requires highly efficient computers and good softwares are required for post-processing.

## 1.1 Parachutes

Parachute is said to have come into being by putting together prefix "para" and noun "chute". The french prefix "para" means "protect against" or "shelter from" as used in parasol("protect against"/"shelter from" sun). The french noun chute is based on old french word "cheute" which means falling or a declivity(downward slope or decent). So the word "parachute" means to protect against falling from height. Parachute is complex aerodynamic decelator. It retards the passage of an object by materially increasing the resistive surface area. Parachutes are being used for variety of applications that includes sport activities, payload recovery, military applications, emergency escape from an aircraft, sky diving and flood relief efforts. There are many types of parachutes; each type being tailored and design to meet a particular requirement. To name a few there are low porosity fast opening fabric parachutes for emergency escape from aircraft, flat

circular porous fabric parachute being used by paratroopers. But one parachute which is particularly stealing the limelight is Ram-Air parachute.

### 1.1.1 Ram Air Parachute

The introduction of ram-air parachutes marked a turning point in parachute design. This is one of the most interesting and potentially important parachute developed in recent years. Ram-Air parachute unlike conventional, round-canopy parachutes, it has large lift-to-drag ratio and, therefore, possess a high degree of maneuverability. Ram-Air parachutes have been quite popular among the sports and defense communities because of their excellent gliding capabilities, maneuverability and high endurance limit. When inflated it resembles a low aspect-ratio wing. It is, however, entirely constructed of fabric which allows it to be packed as a conventional canopy.

### 1.1.2 Aerodynamics of Ram Air Parachute

The Ram-air parachute is quite different from the conventional round canopy parachute. When inflated, it resembles a low aspect-ratio flying wing. It is made out of very low porosity fabric and composed of cells which give the wing its shape. The aerodynamics of Ram-Air parachute is very complex. It involves 3-D unsteady turbulent flows past rapidly deforming boundaries. There is a cut on the leading edge of wing so that *Ram-Air pressure* maintains the wing shape in gliding flight. It is desirable for a profile to have high lift-to-drag ratio ( $L/D$ ) for good aerodynamic performance. The  $L/D$  ratio is related to glide angle of parachute. A parachute with large value of  $L/D$  will, typically, have high range and endurance limit. The typical trajectory of profile consists of inflation stage and steady-state glide stage. The aerodynamic performance of parafoil in this stage is extremely important for success of overall design of parafoil. A basic airfoil section having good lift-to-drag ratio is chosen and cut is applied at leading edge. The leading edge cut allows to enter the Ram-Air inside parafoil and force the fabric to take its desired aerodynamic shape. The location and size of cut plays an important role in performance of parachute system. A small sized cut placed close to stagnation point of basic airfoil section will cause little change to airflow and is desirable for good aerodynamic performance. However, too small a leading edge cut may lead to longer (and sometimes unacceptable) duration of inflation time of the parachute. On the other hand, a very large cut leads

to poor aerodynamic performance is associated with large snatch force on the parachute during inflation due to small inflation time. An optimal size of leading edge cut is one of the key ingredients of Ram-Air parachute design. Theoretically, increase in aspect-ratio should improve  $L/D$  and therefore glide angle. But this is not true in actual practice, As span increases, so do the required number of suspension lines and, therefore, line drag. Also, it has been studied that there is breathing of parachute while coming down.

### 1.1.3 Construction of Ram Air Parachute

Ram-Air parachute is a flying wing made of a very low porosity fabric and composed of various cells which give the wing its shape. A parafoil consists of two fabric panels which form upper and lower surfaces of the wing. Fabric ribs are inserted between these surfaces to define the aerodynamic shape. The pitch and bank control is obtained by steering lines. Pennants along the lower surface of the parafoil transfer the aerodynamic load to suspension line and also aid to improve the lateral stability of the vehicle. They are also useful in improving the efficiency of parafoil by preventing or minimizing the span-wise flow of air. The Clarck-Y airfoil section with a cut at leading edge is quite popular with parafoil designers because of its relative ease in fabrication (as its base is flat). The basic section of Ram-Air parafoil is 12% thick Clarck-Y airfoil. The location and size of leading edge cut are denoted by  $x_{cut}$  and  $\theta_{cut}$ . The  $x_{cut}$  is the distance from the leading edge of the airfoil along the chord line where the cut is applied and  $\theta_{cut}$  is the angle of the cut with free-stream direction.

### 1.1.4 Geometry of Ram Air Parachute

This section of the report describe the geometry of the 3D model parachute used for computation. A 12% thick Clarck-Y airfoil with leading edge cut having  $x_{cut} = 0.1c$  and  $\theta_{cut} = 135^\circ$  is used for Ram-Air parachute. The span of wing is  $1.432c$ . The Aspect-Ratio(AR) of wing is 1.432. The structures which determine the shape of wings are the fabric ribs and the support lines. There are a total of five cells and six ribs including side walls. Each cell is flanked by ribs on either side.



## 1.2 Description of Problem

The aerodynamics of parachute is very complex. It involves 3-D unsteady flow past rapidly deforming boundaries. The real world fluid flow problems related to aerospace engineering are viscous in nature that too involving high Reynolds number. Incompressible Navier-Stokes equations are solved. Computations for both Laminar and turbulent flows are carried out. The flows that has been computed in the present work are:

1.  $Re = 10^6$  flow past a LS(1)0417 airfoil.
2.  $Re = 10^6$  flow past a ram-air parafoil with LS(1)0417 section and with modified lower surface,  $\alpha = 7.5^\circ$ ;  $x_{cut} = 0.1$  and  $\theta_{cut} = 135^\circ$ .
3.  $Re = 10^6$  flow past a five cell Ram-Air parachute with Clarck-Y section.  $\alpha = 7.5^\circ$ ,  $x_{cut} = 0.1$  and  $\theta_{cut} = 135^\circ$ .

The unsteady incompressible RANS equations in primitive variables formulation have been solved using a well proven stabilized finite element method with SUPG(streamline-upwind/Petrov-Galerkin) and PSPG(pressure-stabilizing/Petrov-Galerkin) stabilization terms, that has been applied to various flow problems earlier. The resulting non linear equation system is solved using GMRES in conjunction with diagonal pre-conditioner. Baldwin-Lomax model is employed for turbulence closure.

## 1.3 Literature survey

An overview of 2D computation of flow past Ram-air parachute can be found in article of Mittal, Saxena and Singh [2]. They have used finite element methods to study the aerodynamics of parachute for both laminar and turbulent flows. They also studied the effect of size and location of leading edge cut. The article by Strickland and Higuchi [8] presents state of art concerning the aerodynamic capabilities of parachute. Applications of parafoils have been described in review article by Nicolaidides et. al. [6]. Also the above article summarizes the results obtained from various wind tunnel and free flight tests for cross parachute. An overview of recent advancement in parachute technology can be obtained in the article by Denis [5]. Benney and Stein have developed computational fluid-structure interaction model for parachute inflation. They assumed axisymmetric

deformation of canopy during deformation. More on aerodynamics of parachutes can be obtained from article by Lingard [7]. Ross [9] has utilized potential flow computations in two and three dimensions to study the effect of the leading edge cut for the *LS1-0417* airfoil. Mittal [12] studied the performance of high aspect-ratio elements for incompressible flows. This study is useful in the context of present work where high aspect ratio elements are being utilized close to the parachute surface. Turbulent flows are modeled using an algebraic model for closure. The Baldwin-Lomax turbulence model [11] has been implemented in much simpler form for the 3D computations.

## 1.4 Thesis organization

Subsequent chapters of this thesis have been organized in the following manner.

- Chapter 2 deals with the mathematical formulation i.e. the governing equations, numerical techniques based upon the finite element (FEM) formulation, appropriate boundary conditions and implementation details.
- In chapter 3 computational results are presented and discussed.
- Chapter 4 contains the concluding remarks of present thesis.
- Chapter 5 talks about scope for future work in the area.

## Chapter 2

# Numerical Technique and Procedure

All the computations as mentioned in chapter 1 are carried using stabilized finite element solver for incompressible Navier-Stokes equations. The turbulent viscosity is modelled using Baldwin-Lomax model [11]. A *finite element* is a subregion of discretized continuum. It is of finite size (not infinitesimal) and usually of small geometry than that of continuum. This method enable us to convert a problem with infinite number of degrees of freedom to one with finite number in order to simplify the solution process. The finite element starts with piecewise approximation to dependent variables. Various methods of this class exist, all requiring an integral representation of the partial differential equation to be constructed. The classical finite element method for structural mechanics are based on variational principles. But for many engineering problems, particularly in fluid flow, more general approaches, such as the method of weighted residuals are used. The primary advantage of FEM is its ability to handle a complex geometry.

The major activities involved in any finite element analysis can be typically classified into three routines:

1. Pre-processing
2. Processing
3. Post-processing

## 2.1 Pre-processing

As the name suggests Pre-processing is before processing. It refers to all the tasks to be performed before we can solve the flow using N-S solver. The major pre-processing activities are smoothing the airfoil, generating the mesh, optimization of mesh, deforming the mesh in required form and applying the necessary boundary conditions. The other important activity is to automate the grid generation procedure so that different grids can be generated for different configurations like airfoil and parafoil at different angles of attack and parafoil for different cut configurations.

### 2.1.1 Smoothing the Airfoil

The airfoil geometry obtained from the literature contain very few points. These points are not sufficient to generate a fine mesh which can resolve the flow field properly. So, to increase the number of points on the airfoil, we used a NAG routine E02BAF which fits cubic B-splines.

### 2.1.2 Mesh Generation

The first step in *Computational Fluid Dynamic* is to discretize the general region of interest. This representation may be structured, unstructured, hybrid or multi block. This process of discretization of region of interest is called "Mesh Generation" or "Grid Generation". The grid generated must be boundary-conforming, represents the complete region of interest, as well as exhibit grid point densities appropriate for resolution of relevant flow physics of widely separate length scales. Grid generation is one of the most important part of CFD analysis because with a poor mesh one cannot expect good results even with higher order accurate methods. In-fact it is by far the most time consuming aspect of entire CFD process. Therefore, the goal of grid generation thrust is to develop technology to speed the grid generation process and to improve its quality. In finite element mesh, mesh is basically a set of points, with certain connectivity which one obtains by discretization of the domain of flow. Because of this spatial discretization, the continuum of space is replaced by a finite number of points where numerical value of variables has to be determined. For the simulations in the present study, the space domain is discretized using hybrid grid.

## 2-Dimensional Mesh

For our case before generating 3-D mesh it is required to have good 2-D mesh for Ram-Air parafoil. This 2-D mesh is available from earlier work in lab. Here the region close to the body consists of structured mesh called band of structured mesh, while the rest is filled with unstructured mesh. Unstructured meshes are very useful to capture the complex geometries, at the same time they take into account the complexity of the flow. Structured meshes have logical indexing scheme for the nodes while, the unstructured meshes have a irregular connectivity. In the structured mesh generation the points are distributed in any ratio uniform or geometric progression or exponentially varying. In our cases, structured meshes are constructed using lines normal to the surface of the body. Triangular elements have been considered which are supposed to be ideal for the complex geometries. Filling up the whole domain with structured mesh would be very costly and controlling the density of points would be difficult. So, unstructured mesh is used in the region far from the body.

For the unstructured mesh generation, among various algorithms available for triangulation, Delaunay approach has proved to be very efficient. The most important property of a Delaunay mesh is that for each element in the mesh, its circumcircle which encompasses all nodes defining that element contains no other nodes of the mesh. This produces elements with very optimal aspect ratio.

## 3-Dimensional Mesh

Following are the steps in generation of three dimensional mesh.

1. Three dimensional mesh for straight Ram-Air wing is obtained by stacking two dimensional mesh one behind the others. Since we have triangular elements in 2D mesh, we can get prismatic elements from this stacking procedure. Forty one 2D slices are stacked together to make whole three dimensional domain. Out of them 21 middle slices are on the parachute and we call them para-slices, rest slices contributes for grid around parachute in span-wise direction. Span of para wing is 1.432c. There are six ribs including side walls which make five cells of parachute. The span of parachute is equally distributed on these five cells.
2. During inflation process air enters into the parachute through leading edge cut.

Consequently the straight parachute wing bends slightly in form of curved shell. From literature study we found approximate value of radius-of-curvature ( $R$ ) which is 0.6 times the span of para wing. Since our Aspect-ratio ( $AR$ ) is 1.432c, which means that  $R = 0.86c$ . In this step of grid generation mesh is deformed using automatic mesh moving scheme which is based upon displacements of boundaries. In this method the whole domain is modeled as linear elastic solid and modified equations of linear elasticity are used to solve internal node displacements based upon given boundary deformation.

3. After parachute is deformed then it is required to delete extra set of nodes from the non-para slices which otherwise may cause problem during processing (solving flow).
4. Once 3D parachute mesh is ready, it is required to generate its boundary information which helps in specifying boundary conditions. Also it is required to get the information about faces on the boundaries to get aerodynamic coefficients  $C_d$  and  $C_l$ . Lastly information about minimum distance of all nodes from para boundary are to be collected which will be used in implementation of turbulence-model.

## Data Structure

The basic data structure of the mesh consists of IEN-array and X-array.

The X-array i.e.  $x(nsd, numnp)$  which stores the x and y coordinates of the nodal points. Here,

$nsd$  stands for number of space dimension.

$numnp$  is the global node number.

IEN-array, i.e.  $ien(nen, numel)$  which defines the connectivity between the global nodal points and local node for a particular element. It contains the information of element numbering with respect to local and global node numbering. Here,

$nen$  stands for local node numbers,

$numel$  is the global element number.

for 2D

- $nsd = 2$
- $nen = 3$  for triangular elements,
- $nen = 4$  for quadrilateral elements.

for 3D

- $nsd = 3$
- $nen = 4$  for tetrahedral elements,
- $nen = 6$  for prismatic elements,
- $nen = 8$  for hexahedral elements.

## 2.2 Governing Equations

Let  $\Omega \subset R^{n_{sd}}$  and  $(0, T)$  be the spatial and temporal domains respectively, where  $n_{sd}$  is the number of space dimensions, and  $\Gamma$  denote the boundary  $\Omega$ . The spatial and temporal coordinates are denoted by  $\mathbf{x}$  and  $t$ . The Navier-Stokes equations governing incompressible fluid flow are

$$\rho \left( \frac{\partial \mathbf{u}}{\partial t} + \mathbf{u} \cdot \nabla \mathbf{u} - \mathbf{f} \right) - \nabla \cdot \sigma = 0 \quad \text{on } \Omega \text{ for } (0, T) \quad (2.1)$$

$$\nabla \cdot \mathbf{u} = 0 \quad \text{on } \Omega \text{ for } (0, T) \quad (2.2)$$

Hence,  $\rho$ ,  $\mathbf{u}$ ,  $\mathbf{f}$  and  $\sigma$  are the density, velocity, body force and the stress tensor, respectively. The stress tensor is written as the sum of its isotropic and deviatoric parts :

$$\sigma = -p\mathbf{I} + \mathbf{T}, \quad \mathbf{T} = 2\mu\epsilon(\mathbf{u}), \quad \epsilon(\mathbf{u}) = \frac{1}{2}((\nabla \mathbf{u}) + (\nabla \mathbf{u})^T) \quad (2.3)$$

where  $p$  and  $\mu$  are the pressure and coefficient of dynamic viscosity, respectively. Both the Dirichlet and Neumann type boundary conditions are accounted for, represented as

$$\mathbf{u} = \mathbf{g} \text{ on } \Gamma_g, \quad \mathbf{n} \cdot \sigma = \mathbf{h} \text{ on } \Gamma_h \quad (2.4)$$

where,  $\Gamma_g$  and  $\Gamma_h$  are complementary subsets of the boundary  $\Gamma$ . The initial condition on the velocity is specified on  $\Omega$  :

$$\mathbf{u}(\mathbf{x}, 0) = \mathbf{u}_0 \text{ on } \Omega \quad (2.5)$$

where,  $\mathbf{u}_0$  is divergence free.

## 2.3 Finite Element Formulation

Consider a finite element discretization of  $\Omega$  into subdomains  $\Omega^e$ ,  $e = 1, 2, \dots, n_{el}$ , where  $n_{el}$  is the number of elements. Based on this discretization, for velocity and pressure we define the finite element trial function spaces  $\mathcal{S}_u^h$  and  $\mathcal{S}_p^h$ , and weighting function spaces  $\mathcal{V}_u^h$  and  $\mathcal{V}_p^h$ . These function spaces are selected, by taking the Dirichlet boundary conditions into account, as subsets of  $[\mathbf{H}^{1h}(\Omega)]^{n_{sd}}$  and  $\mathbf{H}^{1h}(\Omega)$ , where  $\mathbf{H}^{1h}(\Omega)$  is the finite dimensional function space over  $\Omega$ . The stabilized finite element formulation of equation 2.1 and equation 2.2 is written as follows: find  $\mathbf{u}^h \in \mathcal{S}_u^h$  and  $p^h \in \mathcal{S}_p^h$  such that  $\forall \mathbf{w}^h \in \mathcal{V}_u^h, q^h \in \mathcal{V}_p^h$

$$\begin{aligned} \int_{\Omega} \mathbf{w}^h \cdot \rho \left( \frac{\partial \mathbf{u}^h}{\partial t} + \mathbf{u}^h \cdot \nabla \mathbf{u}^h - \mathbf{f} \right) d\Omega + \int_{\Omega} \epsilon(\mathbf{w}^h) : \sigma(p^h, \mathbf{u}^h) d\Omega + \int_{\Omega} q^h \nabla \cdot \mathbf{u}^h d\Omega \\ + \sum_{e=1}^{n_{el}} \int_{\Omega^e} \frac{1}{\rho} \left( \tau_{SUPG} \rho \mathbf{u}^h \cdot \nabla \mathbf{w}^h + \tau_{PSPG} \nabla q^h \right) \cdot \\ \left[ \rho \left( \frac{\partial \mathbf{u}^h}{\partial t} + \mathbf{u}^h \cdot \nabla \mathbf{u}^h - \mathbf{f} \right) - \nabla \cdot \sigma(p^h, \mathbf{u}^h) \right] d\Omega^e \\ + \sum_{e=1}^{n_{el}} \int_{\Omega^e} \delta \nabla \cdot \mathbf{w}^h \rho \nabla \cdot \mathbf{u}^h d\Omega^e = \int_{\Gamma_h} \mathbf{w}^h \cdot \mathbf{h}^h d\Gamma \quad (2.6) \end{aligned}$$

In the variational formulation given by equation 2.6, the first three terms and the right hand side constitute the Galerkin formulation of the problem. The first series of element level integrals are the SUPG and PSPG stabilization terms added to the variational formulations. In the current formulation  $\tau_{PSPG}$  is the same as  $\tau_{SUPG}$  and is given as

$$\tau = \left( \left( \frac{2\|\mathbf{u}^h\|}{h} \right)^2 + \left( \frac{4\nu}{h^2} \right)^2 \right)^{-\frac{1}{2}} \quad (2.7)$$

The second series of element level integrals are added to the formulation for numerical stability at high Reynolds numbers. This is a least squares terms based on the continuity equation. The coefficient  $\delta$  is defined as

$$\delta = \frac{h}{2} \|\mathbf{u}^h\|_z \quad (2.8)$$



where,

$$z = \begin{cases} (\frac{Re_u}{3}) & Re_u \leq 3 \\ 1 & Re_u > 3 \end{cases} \quad (2.9)$$

and  $Re_u$  is the cell Reynolds number. Both stabilization terms are weighted residuals, and therefore maintain the consistency of the formulation.  $h$  is the *element length* and various definitions have been used by researchers in the past. Mittal [12] conducted a systematic numerical study to investigate the effect of high aspect ratio elements on the performance of the finite element formulation for three commonly used definitions of  $h$ . The one which results in the least sensitivity of the computed flow to the element aspect ratio has been used for computations in the present work. According to this definition, the element length is equal to the minimum edge length of a triangular (3 noded) element. This fact is also used in 3D.

The time discretization of the variational formulation given by equation 2.6 is done via the generalized trapezoidal rule (Crank-Nicholson). For unsteady computations, we employ a second order accurate in time procedure. Equal in order basis functions for velocity and pressure (the P1P1 element) are used and a 4 point quadrature is employed for numerical integration. The semi-discrete formulation is used to simulate problems with fixed domains, and the DSD/SST (Deformable Spatial Domain/Stabilized Space Time) formulation is used to handle problems with moving boundaries and interfaces. The non-linear equation systems resulting from the finite element discretization of the flow equations are solved using the Generalized Minimal Residual (GMRES) technique. The pre-conditioning used in conjunction with the GMRES method is nodal block diagonal. Matrix free GMRES algorithm is used which reduces the memory requirements. The key advantage of the matrix free GMRES algorithm is direct computation of the result of matrix vector products in the GMRES algorithm which avoids the explicit formation of the element level matrices.

## 2.4 Turbulence Modeling

While computing any solution numerically we are replacing the continuum by a finite number of points. When the flow becomes turbulent there is a cascading of energy from the outer region to the inner layer of boundary layer. There are very high fluctuations which are not caught easily unless we make our mesh very fine. These high fluctuations in the turbulent boundary layer dissipates energy. We in turbulence modeling make an

effort to account for this dissipation by introducing a turbulent viscosity term which is diffusive in nature.

### 2.4.1 Desirable features of Turbulence model

The model of turbulence should :

- predict accurately a wide range of flows;
- be mathematically simple and involve small number of assumptions and model constants;
- be computationally stable and economical in computational time.
- be dimensionally correct.

### 2.4.2 Baldwin-Lomax Turbulence Model

In other turbulence models it is required the knowledge of height of boundary layer ( $\delta$ ). To remove this drawback and also to enable computation in the wake behind a body, Baldwin and Lomax(1978) [11] proposed a new turbulence model which uses magnitude of vorticity to estimate the boundary layer thickness. It uses two layer formulation to model the eddy viscosity.

$$\mu_t = \begin{cases} \mu_{ti} & \text{for } y \leq y_m \\ \mu_{to} & \text{for } y > y_m \end{cases} \quad (2.10)$$

where  $y$  is the normal distance from the wall and  $y_m$  is the smallest value of  $y$  at which the values of  $\mu_t$  from the inner and outer formulae are equal.

#### *Inner region*

In the inner layer, a classical mixing length model is used, and a Van Driest damping function is used to derive the eddy viscosity to zero near the wall.

$$\mu_{ti} = \rho l_m^2 |\Omega| \quad (2.11)$$

where,  $|\Omega|$  is the magnitude of vorticity given by,

$$|\Omega| = \sqrt{\left(\frac{\partial \bar{u}}{\partial y} - \frac{\partial \bar{v}}{\partial x}\right)^2 + \left(\frac{\partial \bar{v}}{\partial z} - \frac{\partial \bar{w}}{\partial y}\right)^2 + \left(\frac{\partial \bar{w}}{\partial x} - \frac{\partial \bar{u}}{\partial z}\right)^2} \quad (2.12)$$

$$l_m = \kappa y [1 - \exp(\frac{-y^+}{A^+})] \quad (2.13)$$

### Outer region

In the outer layer, a function, which is the product of the distance from the solid wall (or wake-line) and vorticity, is used to estimate the velocity scale. The location where the function is maximum gives the length scale. Klebanoff's intermittency factor is used to derive the viscosity to zero away from the viscous region.

$$\mu_{to} = \alpha C_{cp} \rho F_{wake} F_{Kleb}(y) \quad (2.14)$$

where,  $\alpha$  is the Clauser constant,  $C_{cp}$  is an additional constant and

$$F_{wake} = \min(y_{max} F_{max}, C_{wk} y_{max} u_{dif}^2 / F_{max}) \quad (2.15)$$

The quantities  $y_{max}$  and  $F_{max}$  are determined from the function

$$F(y) = y |\Omega| [1 - \exp(-y^+ / A^+)] \quad (2.16)$$

The quantity  $F_{max}$  is the maximum value of  $F(y)$  that occurs in a profile and  $y_{max}$  is the value of  $y$  at which it occurs. In wakes the exponential term of equation 2.16 is set to zero.

$$F_{Kleb} = [1 + 5.5(C_{Kleb} y / y_{max})^6]^{-1} \quad (2.17)$$

The quantity  $u_{dif}$  is the difference between the maximum and the minimum total velocity at a station, i.e.

$$u_{dif} = (\sqrt{\bar{u}^2 + \bar{v}^2 + \bar{w}^2})_{max} - (\sqrt{\bar{u}^2 + \bar{v}^2 + \bar{w}^2})_{min} \quad (2.18)$$

The second term in  $u_{dif}$  is taken to be zero(except in wakes).

The model constants are

$$A^+ = 26, C_{cp} = 1.6, C_{Kleb} = 0.3, C_{wk} = 0.25, \kappa = 0.41, \alpha = 0.0168$$

- The formulation of  $\nu_{to}$  can be used in wakes as well as in attached and separated boundary layers.
- The distribution of vorticity is used to determine the length scales so that the necessity to determine the outer edge of the boundary layer (or wake) is removed.

- The function  $F_{Kleb}$  is Klebnoff's intermittency factor with  $\delta$  replaced by  $y_{max}/C_{Kleb}$ .
- The constants in the Baldwin-Lomax model are determined by requiring agreement with the C-S model for constant pressure boundary layer.

### 2.4.3 Simplification of Baldwin-Lomax Turbulence Model

For 3D flows it is unaffordable to do computations in wake behind the body, much simplified form of Baldwin-Lomax model is used for the computation of turbulent flows. Only the law of inner layer has been implemented.

$$\mu_t = \rho l_m^2 |\Omega| \quad (2.19)$$

where,  $|\Omega|$  is the magnitude of vorticity given by,

$$|\Omega| = \sqrt{\left(\frac{\partial \bar{u}}{\partial y} - \frac{\partial \bar{v}}{\partial x}\right)^2 + \left(\frac{\partial \bar{v}}{\partial z} - \frac{\partial \bar{w}}{\partial y}\right)^2 + \left(\frac{\partial \bar{w}}{\partial x} - \frac{\partial \bar{u}}{\partial z}\right)^2} \quad (2.20)$$

$l_m$  is the mixing length given by,

$$l_m = \kappa y [1 - \exp(\frac{-y^+}{A^+})] \quad (2.21)$$

where,

$$y^+ = yv^*/\nu$$

$$v^* = \sqrt{\frac{\tau_w}{\rho}}, \text{ known as friction velocity.}$$

$\tau_w$  is the shear stress on the wall.

The model constants are:

$$y^+ = 26, \kappa = 0.41$$

## 2.5 Boundary and Initial Conditions

The computational domain is defined by the 11 boundaries.

1. Upper surface of parachute.

2. Lower surface of parachute.
3. Cut surface of parachute (only Ribs).
4. Bottom wall.
5. Downstream Boundary.
6. Top wall.
7. Upstream Boundary.
8. Left side wall.
9. Right side wall.
10. Interior nodes (only Ribs).
11. Parachute surface.

### 2.5.1 On Body Surface

For viscous flow over para surface boundaries (1, 2, 3), no-slip condition is applied, which means that  $u$ ,  $v$ ,  $w$  are set to zero on fabric part of parachute.

### 2.5.2 Inflow and Outflow Boundary Conditions

For The inflow boundary (7) conditions are fixed at free stream values. But outflow(5) boundary kept free from any boundary condition.

### 2.5.3 Boundary Conditions on Side walls, Top and Bottom walls

For side wall boundaries (8, 9) and top wall boundaries (4, 6) it is required to give Neumann type boundary conditions as there is no flow across these boundaries. So it is required to set normal component of velocity to zero.

## 2.6 Numerical Procedure

Numerical solutions are obtained in the following sequences. Initially starting with steady laminar flow at very low Reynolds number ( $Re = 10$ ) and then gradually increasing to Reynolds number ( $Re = 1 \times 10^6$ ). Computations are carried out for various Reynolds No in both steady and unsteady laminar flows. Some computations are also carried on turbulent flows.

## 2.7 Post processing

The process of CFD includes discretization of region of interest into grid. Then solving the fluid dynamic model for calculation of flow-field at grid points and analysis of computed solution. The phase of analysis is termed as *Post Processing*. Post processing of data generated can help the designer to check the result of his solver. Powerful Graphics workstations with powerful Graphic softwares are now available for advantages of CFD workers. We have advanced so much in computational capabilities that the data are produced in such a large size and at such fast rate that any computational aerodynamist cannot spend time in analyzing them. Sophisticated, 3D computer Graphics techniques are now commonly used in all scientific and engineering applications to represent experimental and computed data. Several scientific concepts can only be really understood by plotting the data, which is somewhat easy for 2D cases, but when 3D comes into picture, visualization of data is more important. We can't get much information by just looking at the data. That's why the need of data visualization comes out to interpret and understand data usefully.

Result data of present work is visualized through our homemade softwares, *Post2d* and *Post3d*. These softwares are written in 'C' Language using OpenGL libraries. I would like to thanks to Mr. Mukul and Mr. Bankoti who developed these extremely useful softwares.

Following facilities are presented for graphical presentation of results of three-dimensional simulation.

1. Mesh
2. Colored velocity vectors
3. Contours plotting for any *dof* on any section as colored lines
4. ISO-surface plotting for any *dof*
5. Shading of any given boundary using given color band
6. Lighting effects
7. Saving the colored image in *tiff* format through software itself
8. Reading input files in zipped format

But at present, above said software works only with hexahedral elements, it is required to change ien-array from prismatic to hexahedral just to see the mesh and analyze the solution through this software.

# Chapter 3

## Results and Discussions

This chapter presents the results of our 2-D as well as 3-D simulations of flow past Ram-air Parachute. The problems in order of their appearance in this chapter are :

- Flow past LS(1)0417 airfoil.
- $Re = 10^4$  flow past LS(1)0417 ram-air parafoil.
- $Re = 10^6$  flow past LS(1)0417 ram-air parafoil.
  - Ram-air parafoil with LS(1)0417 section at angles of attack  $\alpha = 7.5^\circ, 15^\circ$ .
  - Ram-air parafoil for different leading edge cut geometries.
- $Re = 10^6$  flow past Five-cell Ram-air parachute with Clark-Y section.

All the computations reported in this chapter are carried out on the Digital, Silicon-Graphics and Sun workstations at IIT Kanpur in 64 bit precision. The incompressible Reynolds Averaged Navier Stokes equations, in conjunction with the Baldwin Lomax algebraic turbulence model for turbulence closure, are solved using stabilized finite element formulations. To stabilize the computations against spurious numerical oscillations in advection dominated flows and to enable the use of equal order interpolation velocity-pressure elements, streamline-upwind/Petrov-Galerkin and pressure-stabilizing/Petrov-Galerkin stabilization techniques are employed. In this technique, stabilizing terms are added to the basic Galerkin formulation (Chapter 3). Equal-in-order linear basis functions for velocity and pressure are used and a 3 point quadrature is employed for numerical



integration. The time integration of the equations is carried out via the time accurate version of the generalised trapezoidal rule (Crank-Nicholson). The nonlinear implicit equation system resulting from the finite element discretization of the flow equations are solved using the Generalized Minimal RESidual (GMRES) technique in conjunction with diagonal preconditioners.

The finite element meshes used in various computations consist of a structured triangular element mesh on the body and an unstructured mesh generated via Delaunay's triangulation, elsewhere. This type of grid has the ability of handling fairly complex geometries while still providing the desired resolution close to the body to effectively capture the boundary layer flow, especially in the context of unsteady flows.

All these examples involve air flow with  $M_\infty \rightarrow 0$  and  $\gamma = 1.4$ . The additional non-dimensional quantities encountered in discussing the results are :

- Strouhal number.

$$S_t = \frac{fd}{\|u_\infty\|}$$

- Pressure coefficient.

$$C_p = \frac{(p - p_\infty)}{\frac{1}{2}\rho_\infty\|u_\infty\|^2}$$

- Drag coefficient.

$$C_d = \frac{D}{\frac{1}{2}\rho_\infty\|u_\infty\|^2 A}$$

- Lift coefficient.

$$C_l = \frac{L}{\frac{1}{2}\rho_\infty\|u_\infty\|^2 A}$$

- Moment coefficient.

$$C_m = \frac{M}{\frac{1}{2}\rho_\infty\|u_\infty\|^2 Al}$$

where,  $f$  is vortex shedding frequency,  $d$  is diameter/characteristic length,  $A$  is the reference area,  $l$  is the reference length,  $D$  is the drag force,  $L$  is the lift force and  $M$  is the pitching moment.

The basic section for the ram-air parafoil is the LS(1)0417 airfoil. The location and size of the leading edge cut are denoted by  $x_{cut}$  and  $\theta_{cut}$ . The  $x_{cut}$  is the distance from

the leading edge of the airfoil along the chord length where the cut is applied and  $\theta_{cut}$  is the angle of the cut with the free-stream direction.

First, results are presented for  $Re = 10^6$  turbulent flow past a clean LS(1)0417 airfoil at  $7.5^\circ, 15^\circ$  and  $17^\circ$ . Next, laminar flow computations ( $Re = 10^4$ ) for a ram-air parachute with  $x_{cut} = 0.1c$  and  $\theta_{cut} = 135^\circ$  are carried out at  $7.5^\circ, 15^\circ$  angles of attack. Results for turbulent flow computations ( $Re = 10^6$ ) for  $7.5^\circ, 15^\circ$  angles of attack are presented and analysed in comparison to those for laminar flow at  $Re = 10^4$  for the same configuration. All the values of the lift and drag coefficients and the Strouhal number, reported in the parafoil results section, have been non-dimensionalized with respect to the chord length of the clean airfoil (without the cut) and freestream speed.

### 3.0.1 Flow past a LS(1)0417 airfoil

#### Computational domain

Figure 1 shows close-up view of the finite element mesh used for the computations for LS(1)0417 airfoil. The 17% thick clean LS(1)0417 airfoil at  $\alpha = 7.5^\circ$  resides in a rectangular domain whose upstream and downstream boundaries are located at 5 and 11 chord lengths from the leading edge, respectively. The upper and lower boundaries lie at 5 chord lengths each from the leading edge. The mesh on the body is structured and extends  $\frac{1}{4}$  of chord length. A fictitious boundary is inserted in order to increase the density of nodes near the body and in the wake. The fine finite element mesh consists of 63,024 triangular elements and 31,685 nodes. The mesh is designed such that in the direction normal to the wall the first element thickness is  $2 \times 10^{-4}c$ .

The structured mesh box used to facilitate the implementation of Baldwin-Lomax model.

#### Boundary conditions

The no slip condition is specified for the velocity on the airfoil surface and freestream values are assigned for the velocity at the upstream boundary. At the downstream boundary a Neumann type boundary condition for the velocity is specified that corresponds to zero viscous stress vector. On the upper and lower surface boundaries the component of ve-

locity normal to the component of stress vector along these boundaries is prescribed zero value. The Reynolds number based on the chord length of the airfoil, freestream velocity and the viscosity of the fluid is  $10^6$ .

## Observations

Figure 1, shows the close-up of the finite element mesh and Figure 2, shows pressure and vorticity fields for the laminar flow steady state solution past a clean LS(1)0417 airfoil at  $\alpha = 7.5^\circ$  for  $Re = 500, 5000, 10^4$ . From the figure it can be observed that the flow structure for  $Re = 5000$  and  $Re = 10^4$  are similar, flow separates on both upper and lower surfaces near trailing edge. Figure 3, shows the finite element mesh and the pressure and vorticity fields for the steady state solution past a clean LS(1)0417 airfoil at  $7.5^\circ$  angle of attack. The Reynolds number is  $10^6$  and flow has been computed with the Baldwin-Lomax turbulence model. From figure it is observed that, the flow is attached to the airfoil except for a small region near the trailing edge on the upper surface. Figure 4, shows pressure and vorticity fields for the laminar flow steady state solution past a clean LS(1)0417 airfoil at  $\alpha = 15^\circ$  for  $Re = 500, 5000, 10^4$ . From Figure 4 it can be observed that, the flow separates near leading edge on the upper surface. Figure 5, shows  $Re = 10^6$  turbulent flow past a clean LS(1)0417 airfoil at  $\alpha = 15^\circ$ , pressure and vorticity fields during one cycle of the lift coefficient variation for developed unsteady flow. From Figure 5, it can be observed that the flow is attached on the lower surface while the flow separates right the leading edge on the upper surface. Figure 6, shows pressure and vorticity fields for both laminar and turbulent flow ( $Re = 10^6$ ) steady state solution past a clean LS(1)0417 airfoil at  $\alpha = 17^\circ$  for  $Re = 500, 5000, 10^4$  and  $10^6$ . From Figure 6, it can be observed that even for the laminar flow case, flow separates near the leading edge on the upper surface while flow on lower surface is almost similar as in case of  $\alpha = 7.5^\circ$  and  $15^\circ$ . Figure 7, shows time histories of the lift and drag coefficients and their power spectra for  $Re = 10^6$  turbulent flow past a clean LS(1)0417 airfoil at  $\alpha = 7.5^\circ, 15^\circ$ . From figure 7, the steady state lift and drag coefficients are 0.76, 0.031, at  $\alpha = 15^\circ$  and 0.50, 0.015 at  $\alpha = 7.5^\circ$  respectively. Figure 8, shows time histories of the lift and drag coefficients, for flow past a clean LS(1)0417 at  $7.5^\circ$  angle of attack, starting from laminar flow ( $Re = 10^4$ ) at  $t = 0$  to turbulent flow ( $Re = 10^6$ ) before  $Re = 10^4$  flow is steady and turbulence model was turned on at  $t = 30.00$ . Figure 8, shows time histories of the lift and drag coefficients, for flow past a clean LS(1)0417 at  $15^\circ$  angle of attack, starting from laminar flow ( $Re = 10^4$ ) to turbulent flow ( $Re = 10^6$ ) before  $Re = 10^4$  flow is steady and

turbulence model was turned on at  $t = 40.00$ .

### 3.0.2 Comparison between flow past Clarck-Y and LS(1)0417 airfoil

By comparing, flow past clean LS(1)0417 airfoil with earlier computed clean Clarck-Y airfoil for the steady state turbulent flow at  $7.5^\circ$  angle of attack it is observed that flow structures for both the airfoil are similar. The steady state lift and drag coefficients for clean Clarck-Y are 1.38 and 0.0204, whereas the same for clean LS(1)0417 are 0.50 and 0.015 respectively.

### 3.0.3 Flow past ram-air parafoil

The present parafoil section has been obtained from the LS(1)0417 airfoil discussed in previous section with  $x_{cut} = 0.1c$  and  $\theta_{cut} = 135^\circ$ . The following sections details the finite element mesh used for calculations, boundary conditions and the observations of the turbulent flow computations along with the discussions for differences observed as compared to laminar flows results.

#### Computational domain

Figure 10 shows a typical finite element mesh and its close up employed for the computations. The 2D model of ram-air parafoil resides in a rectangular computational domain whose upstream and downstream boundaries are located at 5 and 11 chord lengths from the leading edge, (which is the leading edge of the upper surface), respectively. The upper and lower boundaries are placed at 5 chord lengths, each from the leading edge. To study the effect of cut, flow inside and outside the parafoil is simulated. Hence, the mesh exists both outside as well as inside the airfoil. As in the case of LS(1)0417 parafoil, a structured mesh is employed on the body and the rest of the domain is filled with triangles via automatic mesh generator using Delaunay's algorithm. The structured mesh extends  $\frac{1}{4}$  chord length on the parafoil surface. The automatic mesh generator is capable for obtaining the meshes at different angles of attack and different parafoil configurations by making changes in input file. The fabric of the parafoil is assumed to be impervious and thickness of the parafoil is neglected. However, to simulate the pressure differential

across the fabric two sets of nodes, one for the external and other for the internal flow, are utilized. The density of the nodes near the parafoil and in the wake is controlled by inserting the fictitious boundary. The finite element mesh used for the various calculations consist of approximately 21,000 nodes and 42,000 triangular elements. The structured mesh is designed such that in the direction normal to the body the first element thickness is  $2 \times 10^{-4}c$ .

## Boundary conditions

The fabric of the parafoil is assumed to be impervious and no slip condition is specified for the velocity on the parafoil surface and freestream values are assigned for the velocity at the upstream boundary. At the downstream boundary a Neumann type boundary condition for the velocity is specified that corresponds to zero viscous stress vector. On the upper and lower surface boundaries the component of velocity normal to the component of stress vector along these boundaries is prescribed zero value. The Reynolds number is based on the chord length of the original LS(1)0417 airfoil, freestream velocity and the viscosity of the fluid.

$x_{cut} = 0.1c$ ,  $\theta_{cut} = 135^\circ$ ,  $Re = 10^4$  **laminar flow past a ram-air parafoil**

From the computational results for LS(1)0417 airfoil it is observed that the flow is attached for major part of the chord length. However, in the case of ram-air parafoil, due to the leading edge cut, the fluid fills up inside the parafoil and becomes virtually stagnant. Therefore, high pressure responsible for inflating the parafoil and giving its shape is expected. The sharp corners at the leading edge cut are expected to result in separated flows on the outer surface of the parafoil. Figure 11, shows  $\alpha = 7.5^\circ$  laminar flow past a ram-air parafoil with modified lower surface LS(1)0417 section, pressure and vorticity fields for various reynolds numbers. The various Reynolds number considered are  $Re = 500, 5000$  and  $10^4$ . From Figure 11, it can be observed that vortex shedding pattern changes significantly from  $Re = 5000$  to  $Re = 10^4$ . In case of laminar flow, Figures 12, shows  $\alpha = 7.5^\circ$ , the vorticity and pressure fields during one cycle of the lift coefficient for the developed unsteady solution. Figure 13, shows  $\alpha = 15^\circ$  laminar flow past a ram-air parafoil with modified lower surface LS(1)0417 section, pressure and vorticity fields for various reynolds numbers. The various Reynolds number considered are  $Re = 500, 5000$  and  $10^4$ . Figure 14, shows  $\alpha = 7.5^\circ$ , the vorticity and pressure fields during one cycle of

the lift coefficient variation for the developed unsteady solution. From Figure 12, 14 it can be observed that the vortex shedding pattern changes significantly with angle of attack. As the angle of attack increases, the vortex-shedding frequency decreases and vortices become stronger. At larger angles of attack the flow on the lower surface stays attached but it separates on the upper surface right at the leading edge of the cut. The shear layer rolls up and leads to vortex formation. The flow separation at the leading edge results in the formation of unsteady vortical structures that contribute in increase in suction on the upper surface. These dynamic low pressure zones causes unsteady lift acting on the parafoil. The wake for  $\alpha = 7.5^\circ$  is much narrower and more organized compared with that for  $\alpha = 15^\circ$ . Massively separated flow right at the leading edge of the parafoil, is observed for  $\alpha = 15^\circ$ . During each cycle of the time variation of the lift coefficient, one counter clockwise rotating vortex is released from the lower surface at trailing edge. For the  $\alpha = 7.5^\circ$  flow, the shear layer that is formed due to the separation of the flow at the leading edge of the upper surface of the parafoil rolls up, and a clockwise rotating vortex is released, during each cycle of the variation of the lift coefficient. Figure 15, shows the time histories of the lift and drag coefficients and their power spectra at  $\alpha = 7.5^\circ, 15^\circ$  angles of attack. The time-averaged values of the aerodynamic coefficients is also shown in the figure. Compared with  $\alpha = 7.5^\circ$ , the average lift and drag coefficient for  $\alpha = 15^\circ$  is higher. From the power spectra of the aerodynamic coefficients, in addition to the dominant frequency, there exists different other frequencies due to the presence of the secondary and tertiary vortical structures.

$x_{cut} = 0.1\hat{c}$ ,  $\theta_{cut} = 135^\circ$ ,  $Re = 10^6$  **turbulent flow past a ram-air parafoil**

Turbulent flow past a parafoil with the same leading edge cut as in the previous section is computed for  $\alpha = 7.5^\circ$  and  $15^\circ$ . Figure 16, 19 show the pressure and vorticity fields during one cycle of the lift coefficient for the temporally periodic solution for  $\alpha = 7.5^\circ$  and  $15^\circ$  respectively. Compared with the laminar flow for  $\alpha = 7.5^\circ$  the flow in the present case is quite different. The vortices are larger and wake are more organized. The time histories of the lift and drag coefficients and their power spectra are shown in Figure 24. The mean values of the lift and drag coefficients are 0.44 and 0.11 respectively. For the LS(1)0417 airfoil without a leading edge cut the corresponding values are 0.50 and 0.015. The leading edge cut leads to a loss of lift and a very large increase in drag. The lift to drag ratio reduces from 33.33 to 4.00. It can be observed that the  $C_d$  and  $C_l$  for turbulent flow results varies temporally periodically as compared to the laminar flows where

temporal variation is non-periodic. It can be observed that in addition to the dominant, certain other frequencies corresponding to the secondary and tertiary are also present in the power spectra of the aerodynamic coefficients. The peak value of the lift coefficient corresponds to the instant when the large clockwise rotating vortex is fully developed and sits on the upper surface of the parafoil causing an increased suction. During each cycle of lift coefficient a clockwise rotating vortex is shed from the upper surface and a counter-clockwise rotating vortex is shed from the lower surface at the trailing edge. Figure 27,28 show the time histories of the lift and drag coefficients starting from laminar flow ( $Re = 10^3$ ) to turbulent flow ( $Re = 10^6$ ) at angles of attack  $7.5^\circ$ ,  $15^\circ$  respectively. Figure 31, shows the variation of pressure coefficient on the outer surface of the parafoil corresponding to the peak value of the lift coefficient. The pressure distribution on a LS(1)0417 airfoil without a leading edge cut is also shown in the same figure for comparison. The pressure distribution on the outer surface of the parafoil and the LS(1)0417 airfoil are quite different. The leading edge cut results in a significant loss in lift because of two major effects. As can be noticed from the pressure coefficient distribution on the LS(1)0417 airfoil, the region near the leading edge contributes significantly to the total lift. Also, the reduced value of the suction on the upper and high pressure on the lower surfaces cause a loss in pressure differential across the airfoil, thereby reducing the net lift acting on the parafoil. The presence of vortex on the upper surface on the parafoil does contribute to the lift. However, this is an unsteady effect and its contribution to the time-averaged value is not large enough to make up for overall loss in lift.

$x_{cut} = 0.05c$ ,  $\theta_{cut} = 135^\circ$ , flow past a ram-air parafoil

Figure 20, 22 show  $\alpha = 7.5^\circ, 15^\circ$  laminar flow past a ram-air parafoil with LS(1)0417 section, pressure and vorticity fields for  $Re = 500, 5000$  and  $10^4$ . Figure 21, 23 show  $\alpha = 7.5^\circ$ , turbulent flow ( $Re = 10^6$ ) past a ram-air parafoil with LS(1)0417 section, pressure and vorticity fields during one cycle of the lift coefficient variation for the developed unsteady flow solution. From Figure 21 it can be observed that flow is separated near the trailing edge on the lower surface while on the upper surface flow is separated right at the leading edge. The time histories of the lift and drag coefficients and their power spectra for turbulent flow ( $Re = 10^6$ ) are shown in Figure 25. Figure 29, 30 show time histories of the lift and drag coefficients starting from laminar flow ( $Re = 500$ ) at  $t = 0$  to turbulent flow ( $Re = 10^6$ ) at  $t = 190$ . Before  $Re = 500$  flow is steady the turbulence model was turned on at  $t = 150$ .

### 3.0.4 Effect of the size and location of the leading edge cut.

The results in previous section clearly indicate that the flow past LS(1)0417 airfoil changes quite significantly when a leading edge cut is applied to it. The flow past a parafoil section is associated with high drag and a lower lift coefficient. Hence, this suggests that the location and size of the cut is an important aerodynamic design parameter for a ram-air parachute. In order to investigate the effect, computations are carried out for a parafoil at  $7.5^\circ$  angle of attack with two configurations of leading edge cut: (a)  $x_{cut} = 0.1c$ ,  $\theta_{cut} = 135^\circ$  and (b)  $x_{cut} = 0.05c$ ,  $\theta_{cut} = 135^\circ$ . The flow on the upper surface for both cases look very similar. However, there are differences in the flow on the lower surface of the parafoil. The case with  $x_{cut} = 0.05c$  is associated with completely attached flow while there are separation bubbles close to the leading edge in other case. From the time histories of aerodynamic coefficients for two cases as shown in figure 26, it is clear that the aerodynamic performance of the parafoil with  $x_{cut} = 0.05c$  and  $\theta_{cut} = 135^\circ$  is the best. A summary of the time averaged values of the aerodynamic coefficients is presented in Table 1. It can be observed from the table that the Case 2 results in the best value of the lift-to-drag ratio and therefore, this parafoil may be expected to have the best gliding performance. A very small cut, close to the stagnation point of the airfoil is expected to lead to the best aerodynamic performance. However, the location of the stagnation point changes with the angle of attack and a very small cut may lead to an unacceptable duration of the inflation stage. Therefore, the configuration of the leading edge cut is, usually a compromise between good aerodynamic performance in the glide stage and certain other issues related to the inflation stage of the parafoil. To compare the results with Clark-Y parafoil earlier computed, a summary of the time averaged values of the aerodynamic coefficients is presented in Table 2.

Case	$x_{cut}$	$\theta_{cut}$	$C_l$	$C_d$	$C_l/C_d$
1	0.1 c	$135^\circ$	0.40	0.13	3.07
2	0.05 c	$135^\circ$	0.38	0.11	3.45

Table 1:  $Re = 10^6$  turbulent flow past a ram-air parafoil with LS(1)0417 section for two configurations of the leading edge cut: time values of the lift and drag coefficients.

Case	$x_{cut}$	$\theta_{cut}$	$C_l$	$C_d$	$C_l/C_d$
1	0.1 c	$135^\circ$	0.99	0.29	3.41
2	0.05 c	$135^\circ$	1.09	0.19	5.74



Table 2:  $Re = 10^6$  turbulent flow past a ram-air parafoil with Clarck-Y section for two configurations of the leading edge cut: time values of the lift and drag coefficients.

### 3.1 Flow past a Ram-Air Parachute for $Re = 10^6$

As mentioned earlier Clarck-Y airfoil is most commonly used Ram-air parachute section. In this work also we have used the same geometry with  $x_{cut} = 0.1$  and  $\theta_{cut} = 135^\circ$ . Following sections discusses about computational domain, boundary conditions used for calculation and observations of turbulent flow computations.

#### 3.1.1 Computational domain

As it is said earlier that to solve flow equations computationally, it is required to have a computational domain. Here also we have used a cuboidal computational domain. Figure 32 shows the typical 2D finite element mesh and its close up used to make 3D mesh. Figure 33 shows top view and front view of mesh for Five-cell Ram-air parachute. Figure 33 shows Five-cell Ram-air parachute lying in a rectangular box. The size of domain used is  $16 \times 10 \times 3.73$ . Figure 35 shows mesh on the fabric of Five-cell Ram-air parachute, whose upstream and downstream boundaries are located at distance 5 and 11 of chord length from leading edge respectively also the side walls of domain are at distance of 1.145 of chord length. The first element thickness in the normal direction from upper and lower surfaces is  $1 \times 10^{-3}$  of the chord length. Also the elements near the side ribs have thickness of  $4 \times 10^{-2}$  of the chord length. There are approximately 236721 number of nodes and 456400 number of elements in Finite Element mesh. Initially mesh for straight wing was generated by stacking given 2D mesh and after that mesh moving scheme is used to deform the mesh in form of inflated wing. This deformation is approximated from literature review. Mesh is made reasonably fine near wing tips to capture tip vortices. Mesh is symmetrical about  $X-Y$  plane. This 3D mesh was already available.

#### 3.1.2 Boundary Condition

Both Dirichlet and Neumann type boundary conditions are applied. Since the fabric of parachute is assumed impervious, no-slip boundary condition is applied on the parachute

surface. Figure 28 shows the mesh on the fabric surface of Ram-Air parachute drawn using no-slip boundary conditions. On the upstream boundary free-stream value of component of velocities is applied. At the downstream boundary a Neumann type boundary condition for the velocity is specified that corresponds to zero viscous stress vector. On the rest of the boundaries *i.e Top surface, Bottom surface, and side walls*, Neumann type boundary condition is applied such that there is no flow across the boundaries. Velocity normal to these boundaries are specified zero. The Reynolds number is based upon chord length of original Clark-Y airfoil, free-stream velocity and viscosity of fluid.

### 3.1.3 Observations

#### Turbulent calculations at $Re = 1 \times 10^6$

The computations are initiated with steady state solution for  $Re = 10$ . The steady state solution is obtained by simply removing the unsteady terms from the governing equations. This is possible because the present method utilizes the implicit time-integrating procedure. The Reynolds number is then ramped upto  $Re = 250$ . After that unsteady calculations are initiated at  $Re = 500$  and goes upto  $Re = 10^6$  over a period of approximately 8000 time step with time size of  $10^{-3}$ . Figure 36 shows the pressure and z-vorticity fields at various x-y section along the span wise direction. At mid span section flow separates right at mid chord length on the upper surface as we move from mid span section to wing tip, separation point gets closer towards leading edge. Figure 37 shows pressure and x-vorticity, Figure 38 shows magnitude of velocity and magnitude of vorticity and Figure 39 shows y-vorticity and z-vorticity fields at various y-z sections, The location of various sections are,  $x/c = 0.1, 0.5, 1.0, 2.0, 3.0$ , where origin is located at the leading edge of basic airfoil without cut. As we ramped from  $x/c=0.1$  to  $x/c=3.0$ , It is observed that wing tip vortices gets stronger and comes closer. Figure 40 shows the variation of pressure coefficient along the outer surface of parafoil at various 2D span-wise sections. The location of various 2D sections are,  $z/b= 0.0, 0.1, 0.2, 0.3, 0.4, 0.5$ . From Figure 40 it is observed that pressure coefficient variation on the lower surface is almost similar on each span-wise 2D sections except wing tip section where suction is highest near trailing edge which diverges the intermediate flow towards wing-tip section trailing edge. This is the cause of span-wise flow on the lower surface. On the upper surface wing, tip slices shows the highest suction at  $x/c=0.5$  because of high pressure differential across upper and lower surface. This causes the flow to rolls-up as wing-tip vortices. In turbulent flow,

3D flow past five-cell Ram-air parachute is steady while 2D flow past ram-air parafoil at the same angle of attack is unsteady. By comparing pressure coefficient variation over 2D Clark-Y ram-air parafoil with 2D span-wise section of Five-cell Ram-air parachute, it is observed that suction peak and so adverse pressure gradient reduces in case of 3D flow. This reduction in suction peak is due to the span-wise velocity in 3D flow, and reduced adverse pressure gradient in case of 3D flow is responsible for steady flow. Figure 41 shows the variation of pressure coefficients along the outer surface of the Ram-air parachute, at various 2D chord-wise sections. The location of various 2D sections are,  $x/c=0.1, 0.25, 0.50, 0.9, 0.98$ . As we ramp from  $x/c=0.1$  to  $x/c=0.98$ , it is observed that adverse pressure gradient increases near wing-tip on the upper surface. Figure 43 shows isosurface corresponding to magnitude of velocity  $=0.95$ . Figure 44 shows isosurface corresponding to  $x$ -vorticity  $=2.00$ . Figure 45 shows magnitude of velocity fields on the mid section of parachute surface. Figure 46 shows the pressure fields on the mid section of parachute. From Figure 45, 46 as expected we observed two small vortices near the side ribs of parachute. These two vortices at the tip are due to span-wise flow from the lower surface to upper surface. These vortices rolls from lower surface to upper surface as the results of which pressure gradient decreases in that region. Loss in lift occurs at the tips due to the decrease in pressure differential. For an infinite wing at sub-sonic speeds, the up-flow in the front of the wing exactly balances the down-flow at the rear of the wing, so that no net downward movement of air past the wing results from the circulation. This is not true for a finite wing, for circulation or free vortex flow cannot end abruptly in a real fluid and the circulatory flow continues outside the wing in form of tip vortices. Figure 43 contains an ISO-surface for the velocity magnitude showing flow continues outside the wing in form of tip vortices. Figure 42 shows the time histories of lift and drag coefficients for the computations. The mean value of lift and drag coefficients are 0.60, 0.21 for 7100 time steps with each having approximate time-size of  $1 \times 10^{-3}$ . The average value of  $L/D$  ratio is 2.86. Figure 47 shows parachute fabric and variation of magnitude of velocity,  $x$ -velocity,  $y$ -velocity,  $z$ -velocity, pressure,  $x$ -vorticity,  $y$ -vorticity and  $z$ -vorticity. on  $y$ - $z$  section plane away from the parachute surface.

# Chapter 4

## Conclusions

A well proven stabilized finite element method has been utilized to solve the incompressible Reynolds Averaged Navier-Stokes equations in the primitive variable formulation. Results have been presented and discussed with reference to 2-D simulations:  $Re = 10^6$  flow past LS(1)0417 airfoil at  $\alpha = 7.5^\circ, 15^\circ$ ;  $Re = 10^6$  flow past ram-air parafoil with a leading edge cut;  $Re = 10^6$  flow past Five-cell Ram-air parachute with Clark-Y section.

$Re = 10^6$  flow past a LS(1)0417 airfoil at  $\alpha = 7.5^\circ, 15^\circ$  and a ram-air parafoil with a leading edge cut at angles of attack  $\alpha = 7.5^\circ, 15^\circ$  have been computed. The flow past LS(1)0417 airfoil, without a leading edge cut, for  $\alpha = 7.5^\circ$  is attached and steady. Flow past the LS(1)0417 airfoil with a leading edge cut is separated and unsteady even for small angles of attack. The sharp corners at the leading edge cut causes flow separation and results in unsteady flow. A significant loss in lift and increase in drag compared to the LS(1)0417 airfoil is observed. The flow inside the parafoil cell remains virtually stagnant resulting in high value of pressure that is responsible for giving the parafoil its shape. Results for ram-air parafoil for  $Re = 10^6$  have been compared with laminar flow results at  $Re = 10^4$ . Significant differences in the flow fields have been observed. The vortex shedding frequency for the parafoil at similar angles of attack is lower for turbulent flows as compared to laminar flows. Also the size of the vortices formed is bigger in case of turbulent flows. The vortex shedding frequency decreases with the increase in angle of attack for both laminar and turbulent flow cases. The effect of the configuration of the leading edge cut on the flow is investigated. In all the cases, that are considered, the flow remains unsteady. The leading edge cut has a strong influence on the lift-to-drag ratio. There is not much difference in flow observed on upper surface of parafoil

for different configurations, however, the flow quality on the lower surface improves as the leading edge cut becomes smaller and moves closer to the location of stagnation point for the basic airfoil section. It is observed that even though the time histories of the aerodynamic coefficients from the laminar and turbulent flow computations are quite different, their time averaged values are similar. It is observed that for the same leading edge cut configuration, the Clark-Y section results in higher lift-to-drag ratio value than the LS(1)0417 section.

The 3D surface geometry of parachute is extremely complex. A triangular element is stacked together to get a 3D mesh having 6 noded prismatic elements. Now, the entire mesh is assumed to be a big rubber block whose elements can go through relative deformation. The points lying on the parachute surface are moved by an appropriate amount so that surface resembles the final parachute surface. Then the linear elasticity equations are utilized to generate the rest of the 3D volume mesh. This 3D mesh was available in the Lab. Both laminar and turbulent flows have been computed. A well proven stabilized finite element method has been utilized to solve the incompressible Navier-Stokes equations in the primitive variable formulation. The turbulent flows have been computed using much simplified form of Baldwin-Lomax turbulence model. Only the law of inner layer has been implemented. While the 2D flow with the Clark-Y section results in an unsteady flow, the 3D computations show a steady flow. Compared to the 2D flow, the 3D flow is associated with a lower lift to drag ratio. Perhaps, it is the wing tip vortices that are responsible for that effect.

# Chapter 5

## Scope for Future work

In the present thesis, the Baldwin-Lomax turbulence model predicts the turbulent flows at  $Re = 10^6$  well for attached flows and feebly separated flows. But it does not predict the flow past airfoil at high angles of attack correctly. The Baldwin-Lomax turbulence model code has been modified for selecting the right peak of moment of vorticity function at a streamwise location. The algorithm implemented is the one proposed by Kallinderis, for peak selection. Re-calculation for the present case should be carried out using modified codes.

It is suggested that the modifications to Baldwin-Lomax turbulence model suggested by various researchers may be applied and the computations should be done to study the variations in the results. This research on the use of turbulence modelling could also be extended to more sophisticated models like  $k - \epsilon$  two-equation turbulence model.

- At present flow is simulated only on five cells of parachute, it is possible to simulate flows for higher number of cells and to study the effect of parachute aspect-ratio.
- In the present simulation the shape of parachute is assumed to be fixed. But as a result of unsteady flow, the shape of parachute gets modified one may observe flutter of parachute fabric.
- In the present simulation the shape of parachute is assumed to be fixed. But further calculations can be done for deforming boundaries of parachute. For this it is required to develop a structural model which can calculate the stresses on the parachute surface using membrane analysis as fabric of parachute surface behaves

as membrane. Further This model should be coupled with fluid model.

- This thesis present only the behavior of two aerodynamic coefficients  $C_d$  and  $C_l$ , there is sufficient scope is to study some other coefficients like  $C_{pitch}$ ,  $C_{yaw}$  and  $C_{roll}$  which are related to stability of parachute. These coefficients are already calculated through code.
- It would be better if all the codes be parallelized so as to run them on supercomputer to get quick results. Also in that case much fine mesh can be used to get better accuracy.

# Bibliography

- [1] F.M. WHITE: Viscous fluid flow. *McGraw-Hill, Inc.*
- [2] S. MITTAL. P. SAXENA, A. SINGH: Computation of 2D flows past ram-air parachutes. In press *Int. Journal of Num. Methods in Fluids*, 2000.
- [3] A. SINGH: B.Tech. Project Report, IIT Kanpur, 1998.
- [4] P. SAXENA: *Numerical Simulation of turbulent flows using the Baldwin-Lomax model*. M.Tech Thesis, IIT Kanpur, 2000.
- [5] D.R. DENNIS: Recent advance in parachute technology. *Aeronautical Journal*, pp. 333-341, 1983.
- [6] J.D. NICOLAIDES, R.J. SPEELMAN III, G.L.C MENARD :A review of parafoil applications. *Journal of Aircraft* 7, pp. 423-431, 1970
- [7] J.S. LINGARD: The aerodynamics of gliding parachutes. *AIAA Paper*, 14 pp. 285-311, 1982
- [8] J.H. STRICKLAND, H. HIGUCHI: Parachute aerodynamics: An assessment of prediction capability. *Journal of Aircraft*, 33, pp. 709-749, 1996.
- [9] J.C. ROSS: Computational aerodynamics in the design and analysis of ram-air inflated wings. AIAA Paper, 93-1228 RAes/AIAA 12th Aerodynamic Decelerator Systems Technology conference and seminar, London, 1993.
- [10] K. STEIN, R. BENNEY, T. TEZDUYAR, J. POTVIN: Fluid-Structure interactions of a cross parachute: Numerical Simulation. *Computer Methods in Applied Mechanics and Engineering*, Reprint, 2000
- [11] B. BALDWIN, H. LOMAX :(1978) Thin layer approximation and algebraic model for separated turbulent flows. *AIAA paper 78-257*.



- [12] S. MITTAL: On the performance of high aspect ratio elements for incompressible flows. *Computer Methods in Applied Mechanics and Engineering*, vol. 188, (1-3), pp. 269-287, year 2000.
- [13] W.L. GARRARD, T.E. TEZDUYAR, S.K. ALIABADI, V. KALRO, J. LUKER, S. MITTAL: Inflation analysis ram-air inflated gliding parachutes. *AIAA Paper*, 95-1565, 13th Aerodynamic Decelerator and Systems
- [14] S.K. ALIABADI, W.L. GARRARD, V. KALRO, S. MITTAL, T.E. TEZDUYAR, K.R. STEIN: Parallel finite element computations of the dynamics of large ram air parachutes. *AIAA Paper*, 95-1581, 13th Aerodynamic Decelerator and Systems Conference, pp. 278-293, Clearwater, Fl, 1995.
- [15] T. TEZDUYAR, V. KALRO, W. GARRARD: Parallel computational methods for 3D simulation of a parafoil with prescribed shape changes. Technical Report 96-082, AHPCRC, 1996
- [16] V. GUPTA, S. GUPTA : Fluid Mechanics. *McGraw-Hill, Inc.*
- [17] E. KREYSZIG: Advance Engineering Mathematics. *John Wiley and Sons, Inc.*

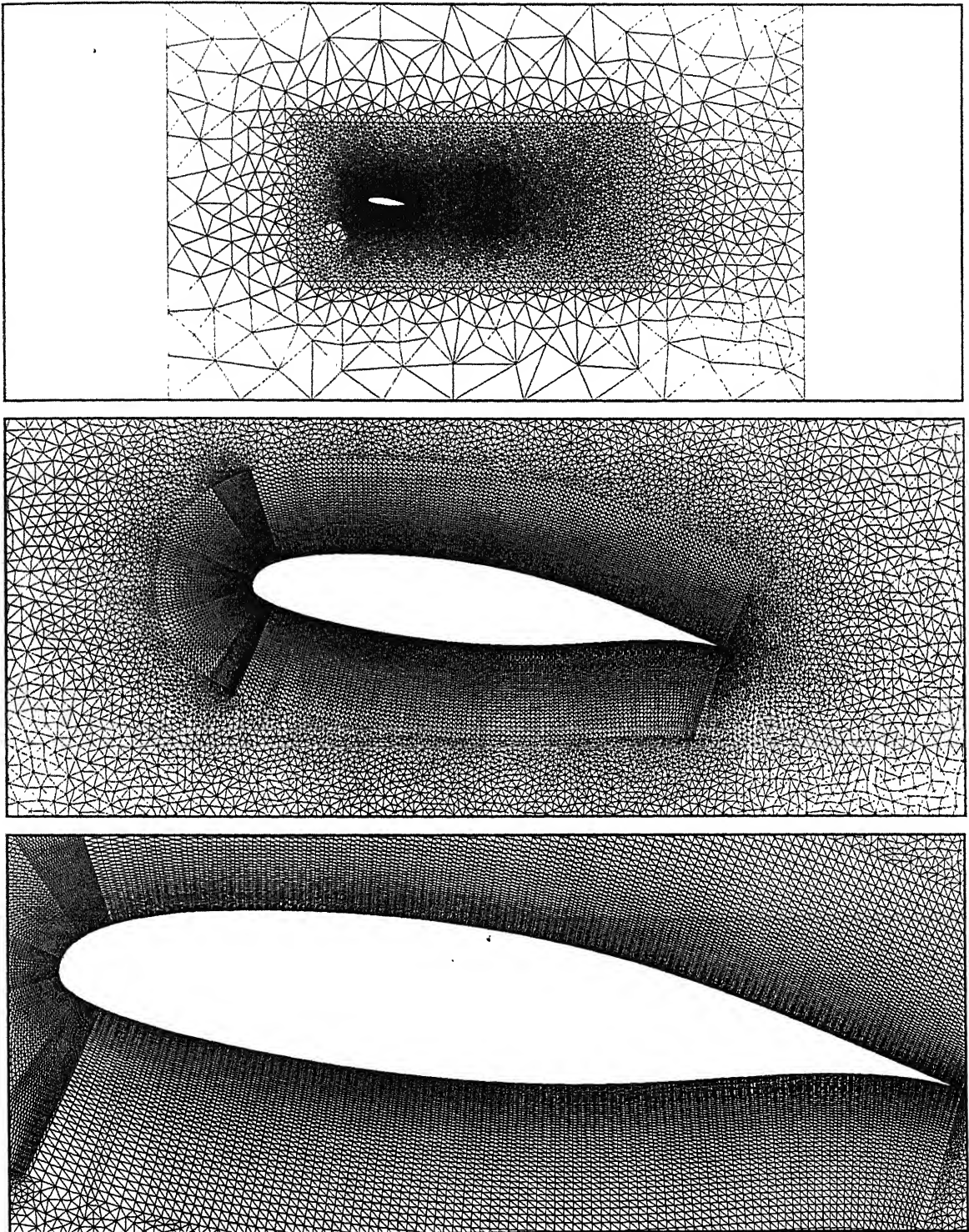


Figure 1: Flow past a LS(1) 0417 airfoil: a typical finite element mesh employed for computations and its close-ups at  $\alpha = 7.5^\circ$ . The mesh consists of 31,685 nodes and 63,024 triangular elements.

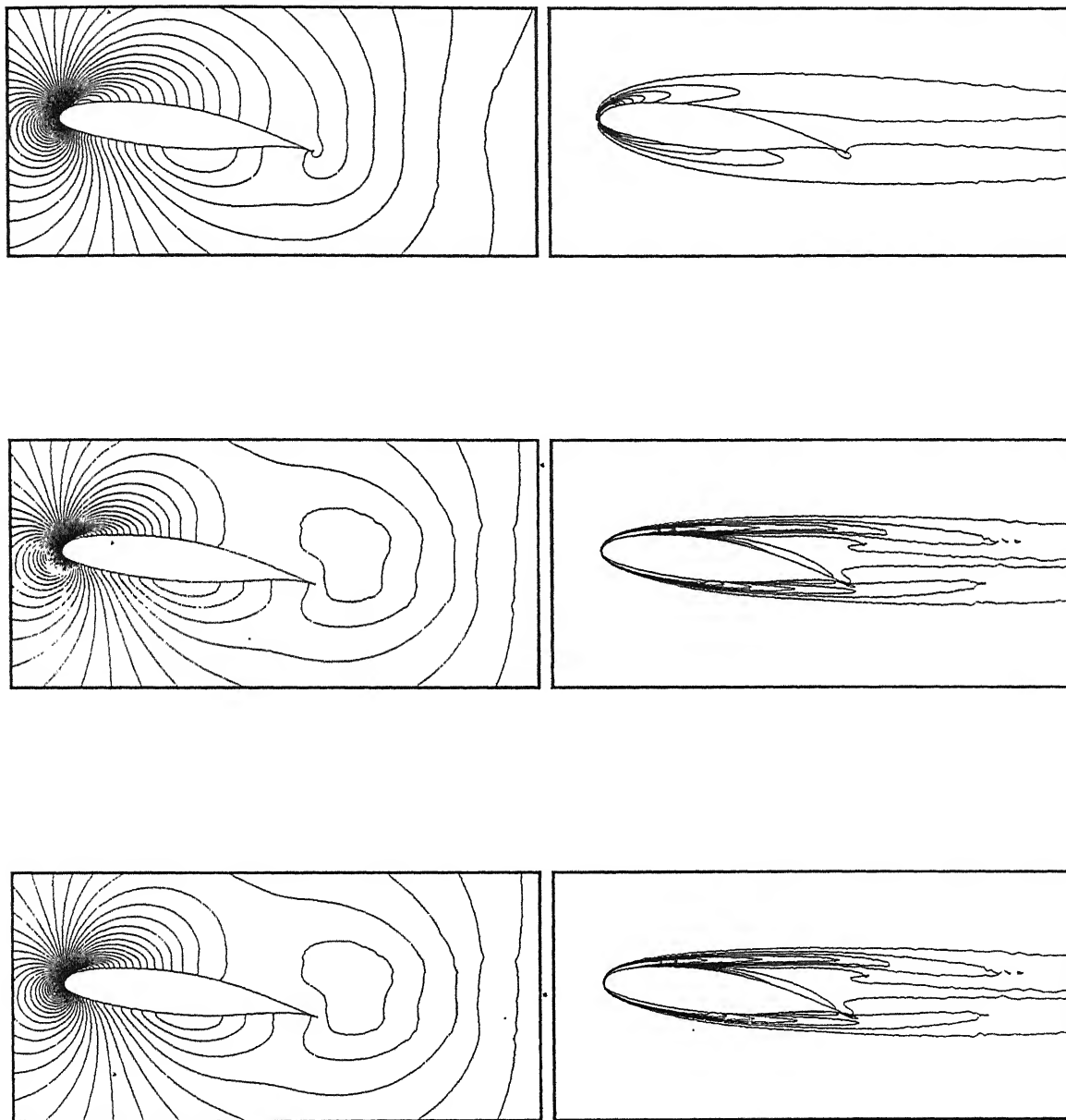
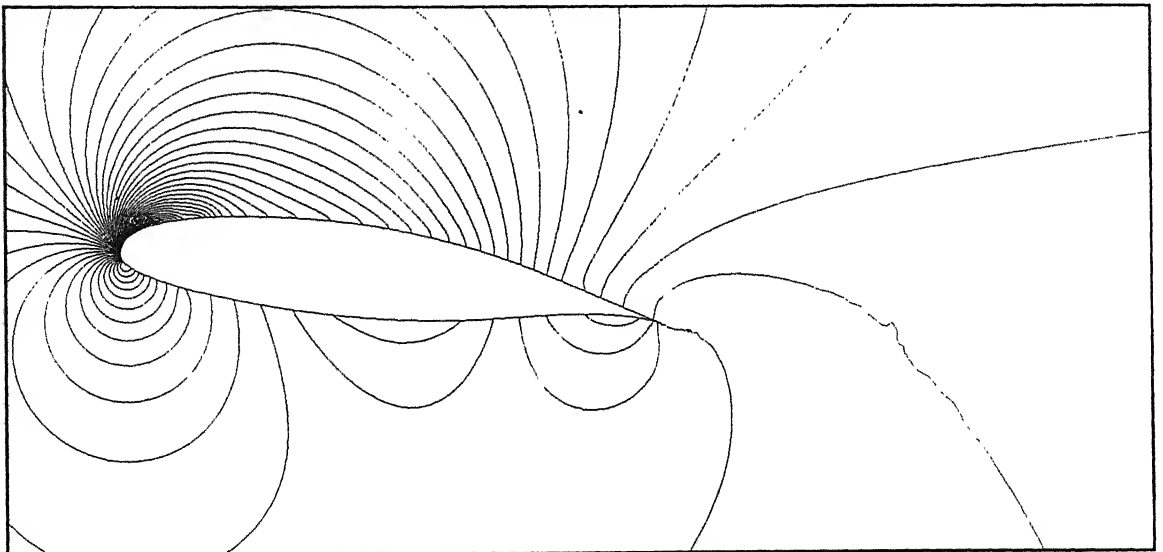
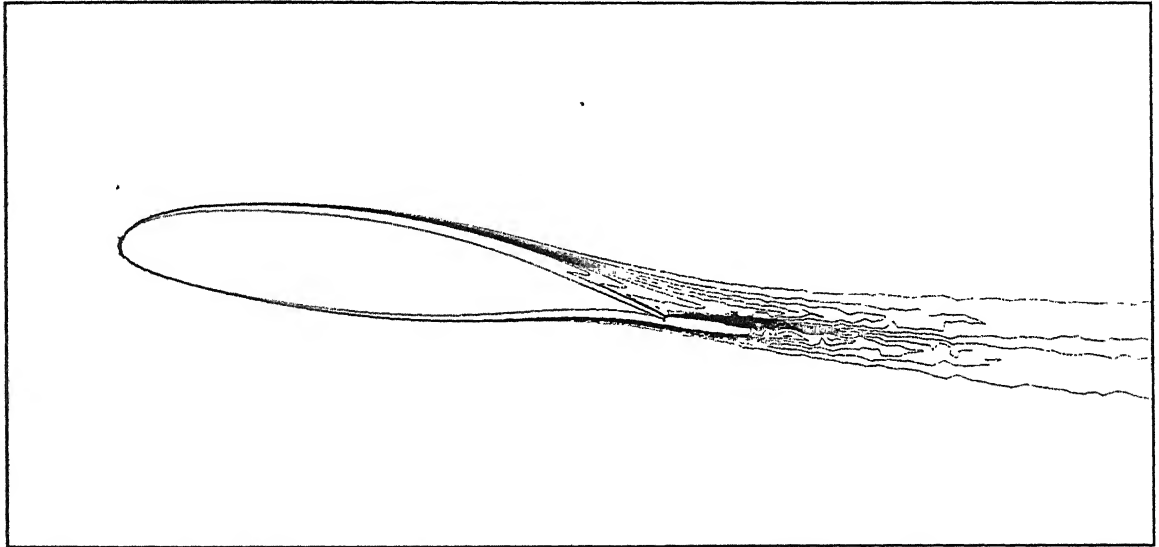
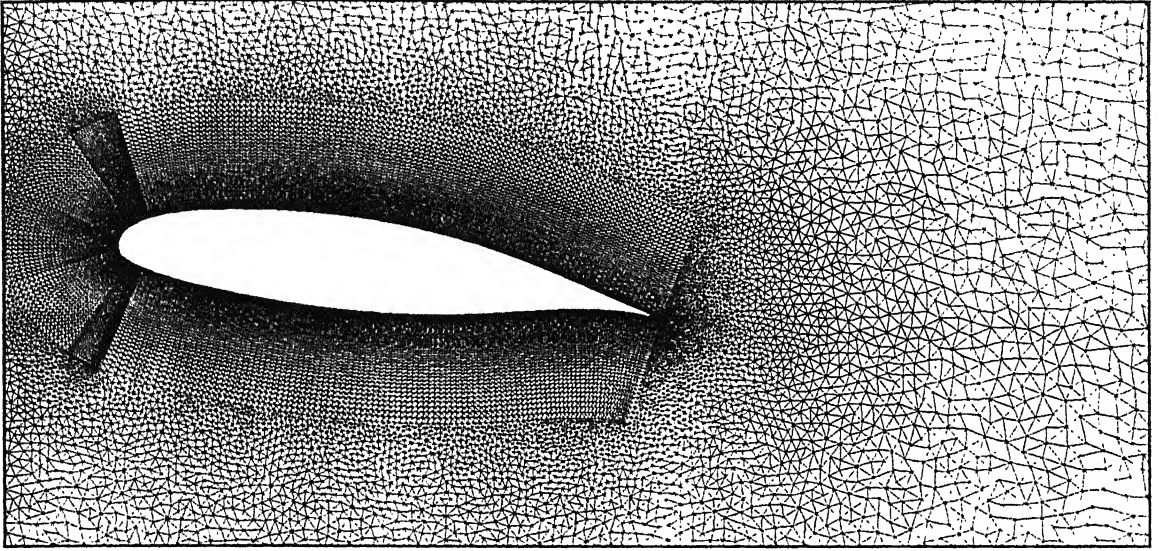


Figure 2:  $\alpha = 7.5^\circ$ , laminar flow past a LS(1) 0417 airfoil: pressure(left), vorticity(right) fields from top to bottom  $Re = 500$ ,  $Re = 5000$  and  $Re = 10^4$ .



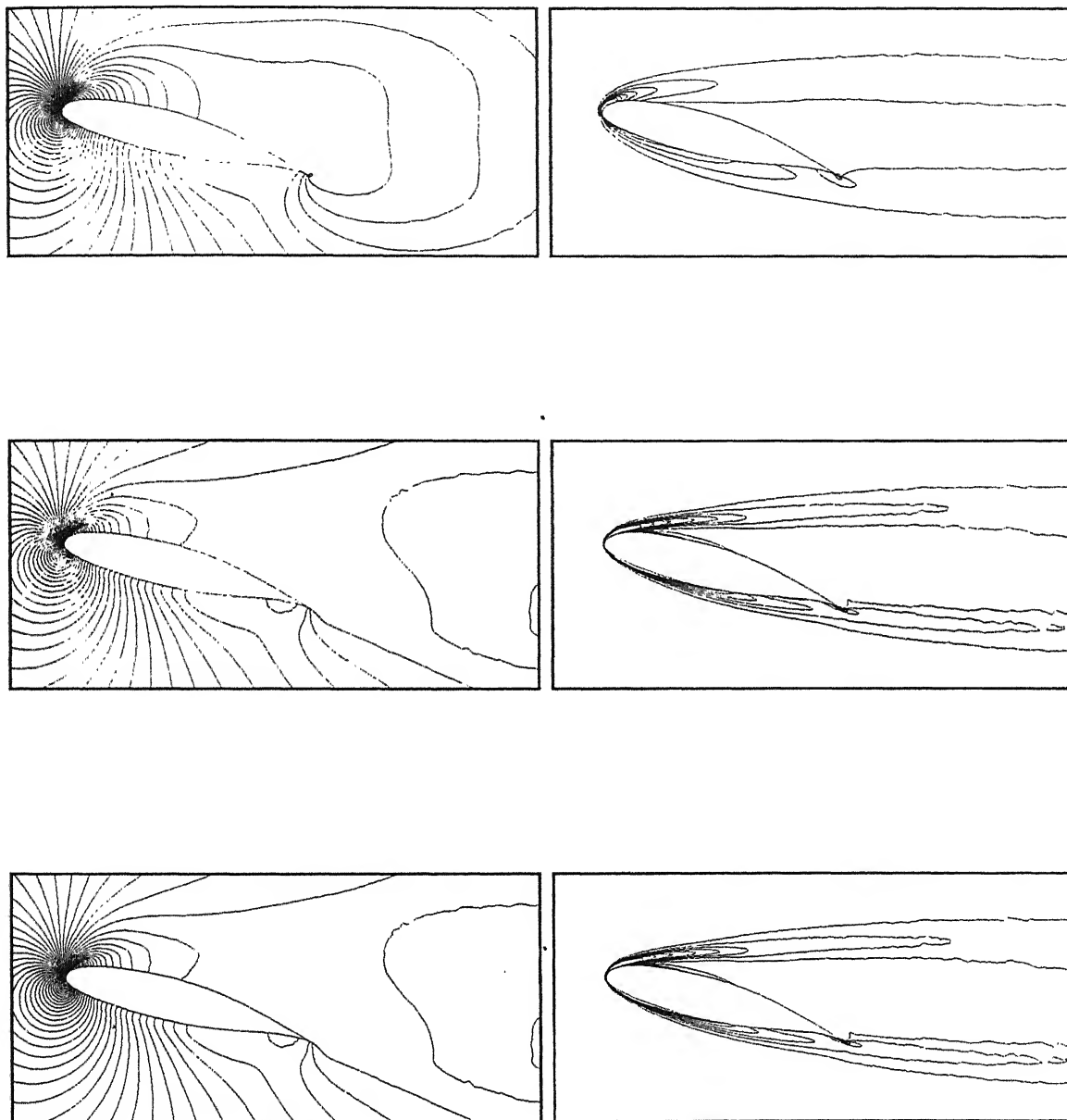


Figure 4:  $\alpha = 15^\circ$  laminar flow past a LS(1) 0417 airfoil: pressure(left), vorticity(right) fields from top to bottom  $Re = 500$ ,  $Re = 5000$  and  $Re = 10^4$ .

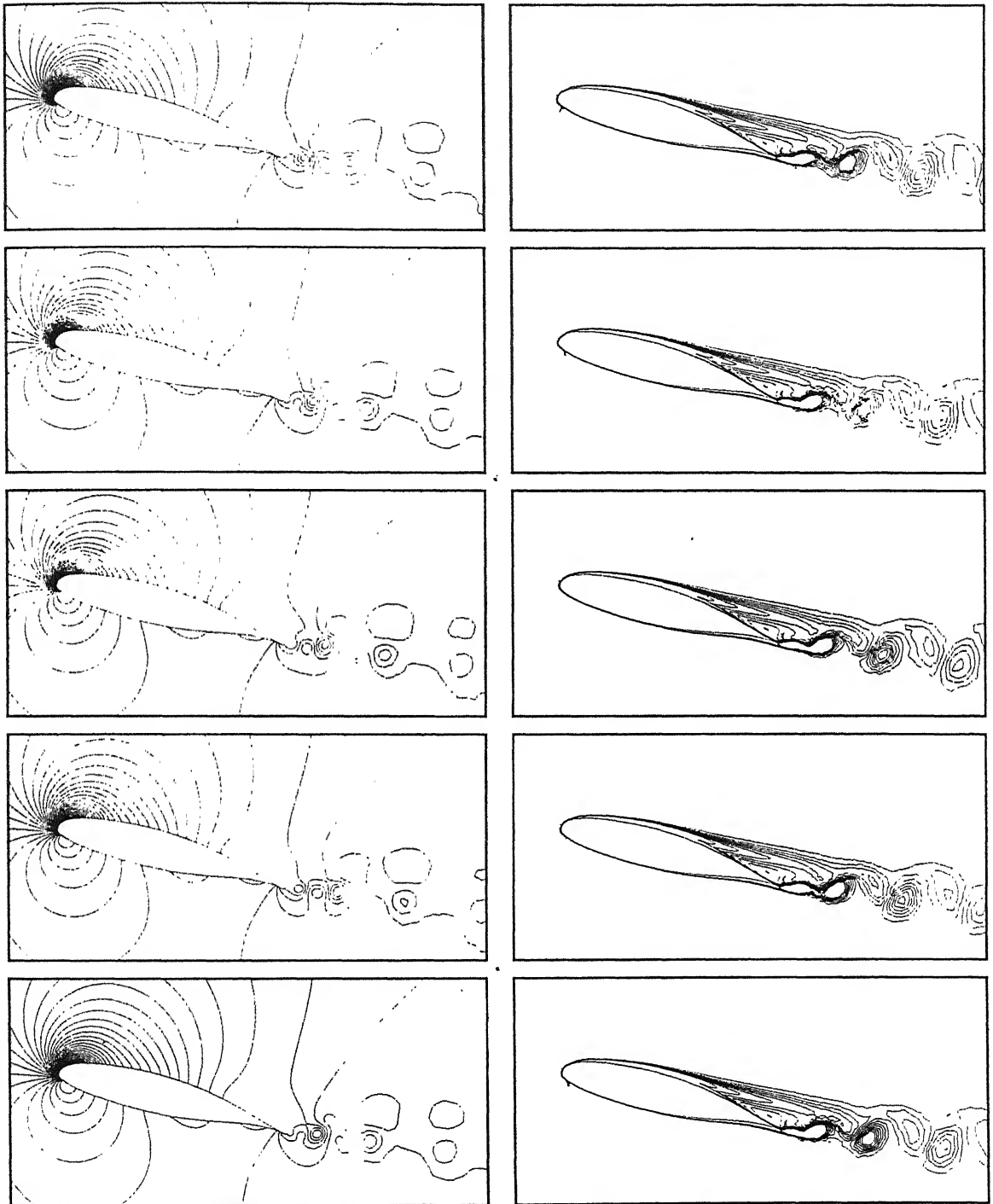


Figure 5:  $Re = 10^6$  turbulent flow past a LS(1) 0417 airfoil at  $\alpha = 15^\circ$ : pressure (left) and vorticity (right) fields during one cycle of the lift coefficient variation for the developed unsteady solution.

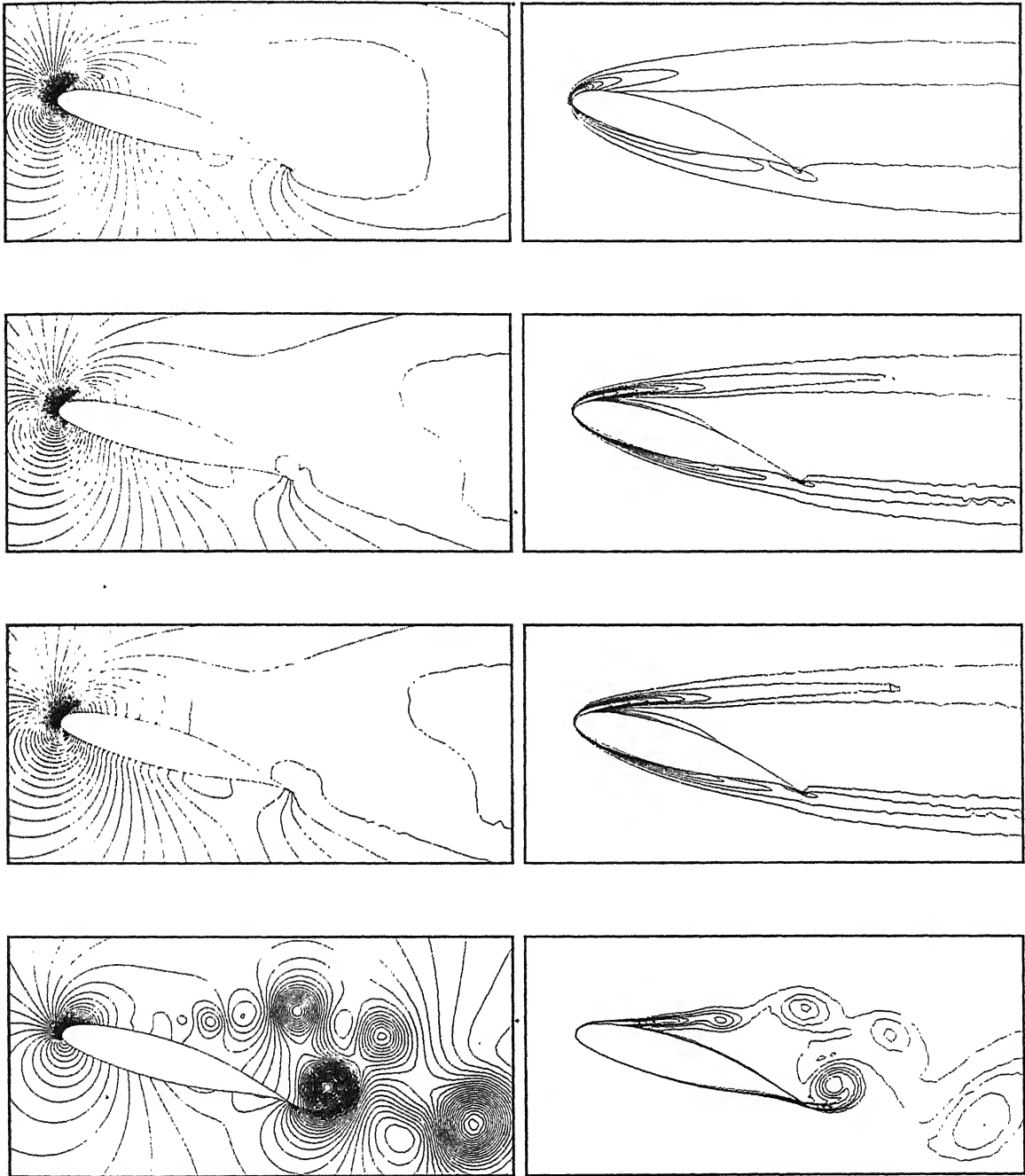


Figure 6:  $\alpha = 17^\circ$ , laminar as well as turbulent flow past a LS(1) 0417 airfoil: pressure(left), vorticity(right) fields from top to bottom  $Re = 500$ ,  $Re = 5000$ ,  $Re = 10^4$  and  $Re = 10^6$ .

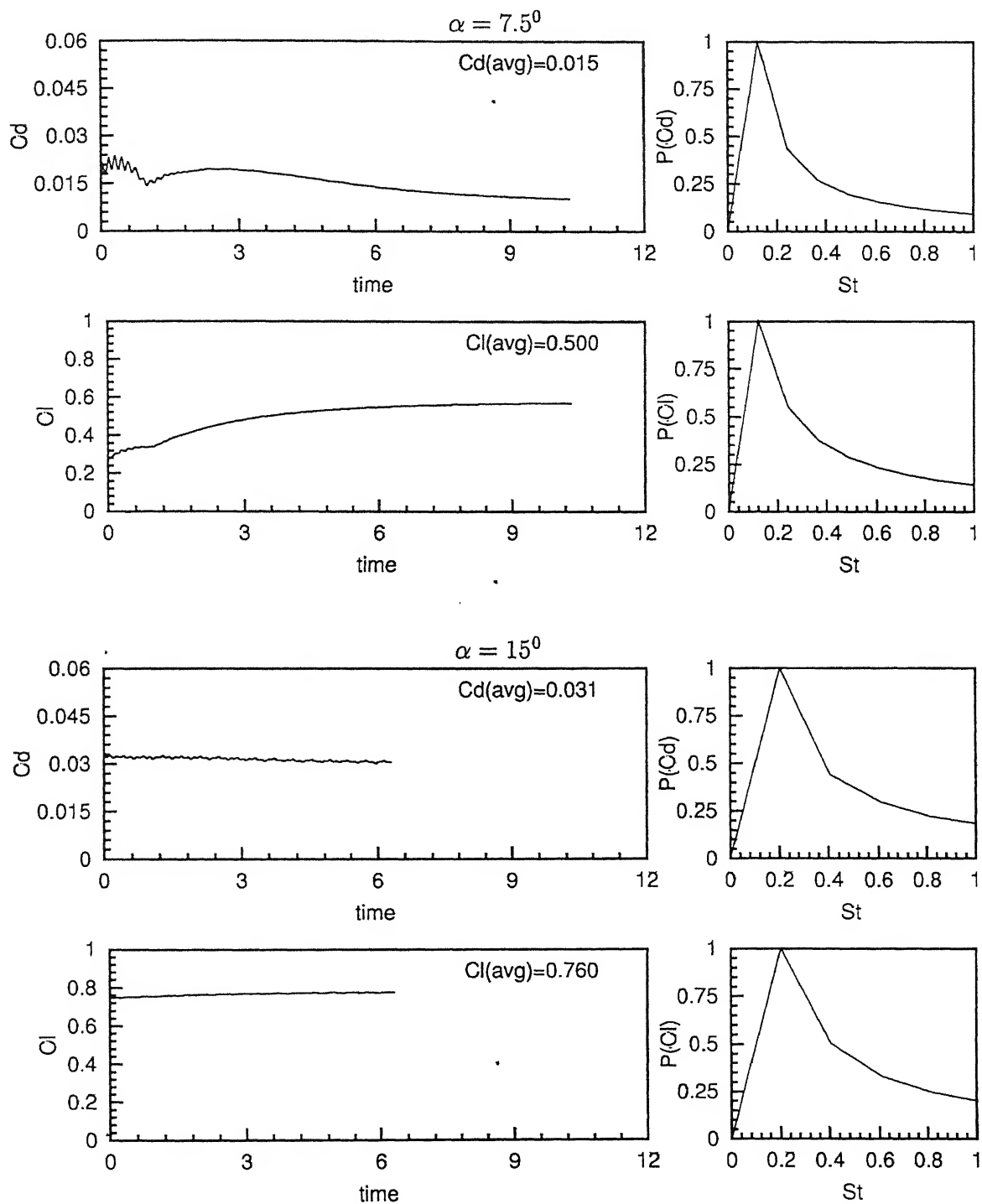


Figure 7:  $Re = 10^6$  turbulent flow past a LS(1) 0417 airfoil at  $\alpha = 7.5^\circ, 15^\circ$ : time histories of the lift and drag coefficients and their power spectra.



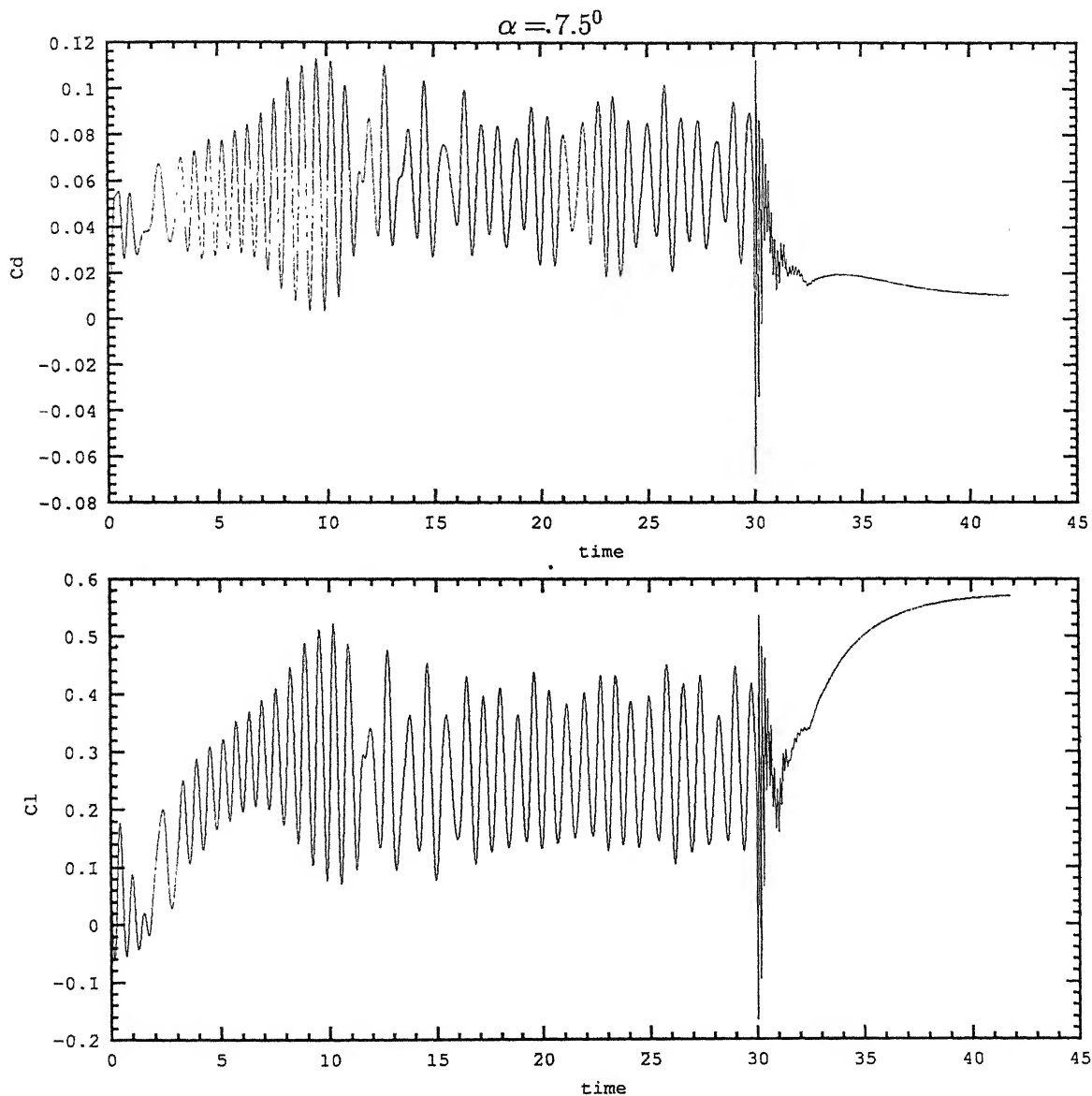


Figure 8: Flow past a LS(1) 0417 airfoil: time histories of the lift and drag coefficients,  $Re = 10^4$  for  $0 \leq t \leq 30$ ,  $Re = 10^5$  for  $30 \leq t \leq 31.5$ ,  $Re = 10^6$  for  $31.5 \leq t \leq 42$ . The turbulence model was turned on at  $t = 30.0$ .

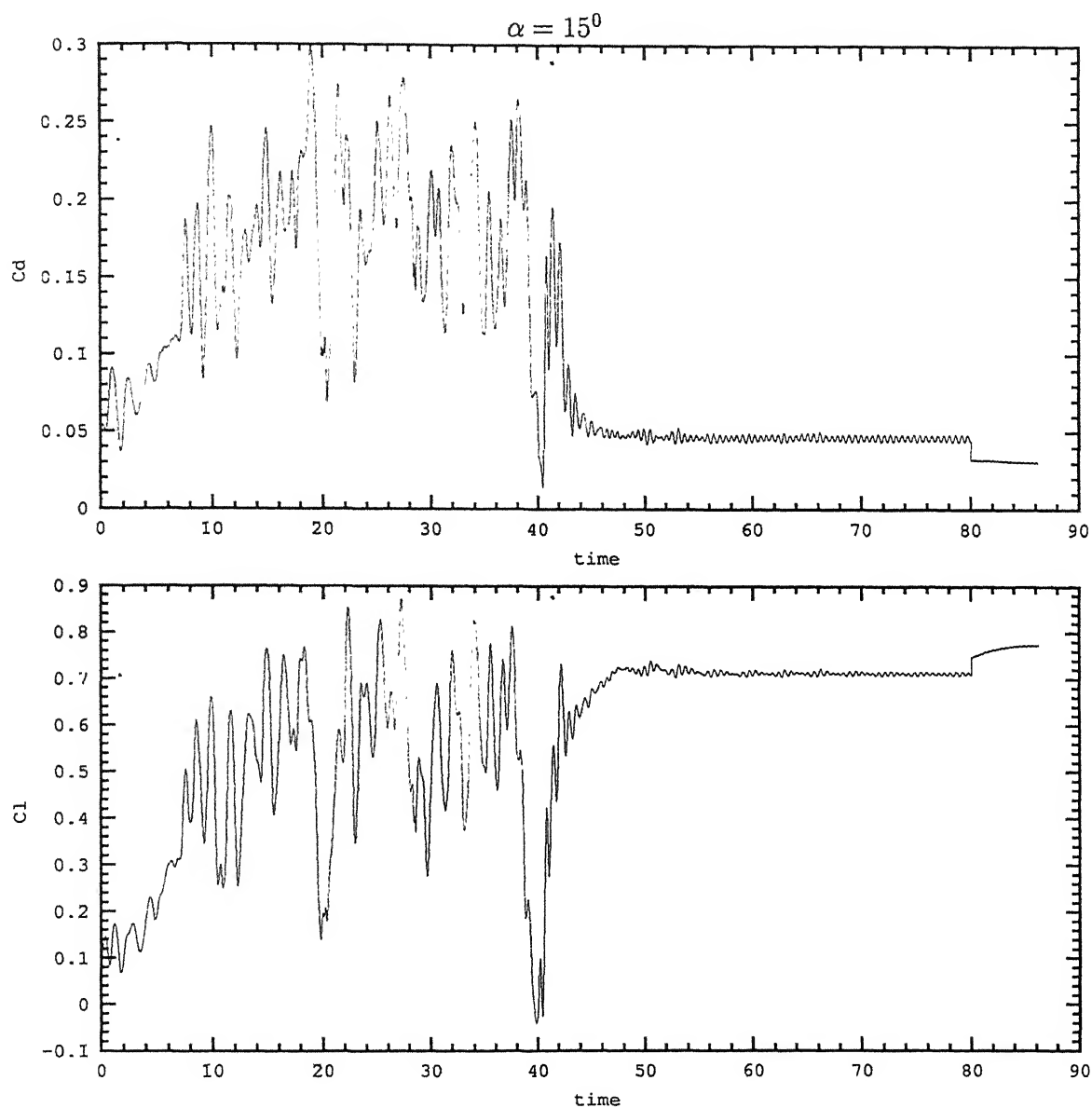


Figure 9: Flow past a LS(1) 0417 airfoil: time histories of the lift and drag coefficients,  $Re = 10^4$  for  $0 \leq t \leq 40$ ,  $Re = 10^5$  for  $40 \leq t \leq 80$ ,  $Re = 10^6$  for  $80 \leq t \leq 86$ . The turbulence model was turned on at  $t = 40$ .

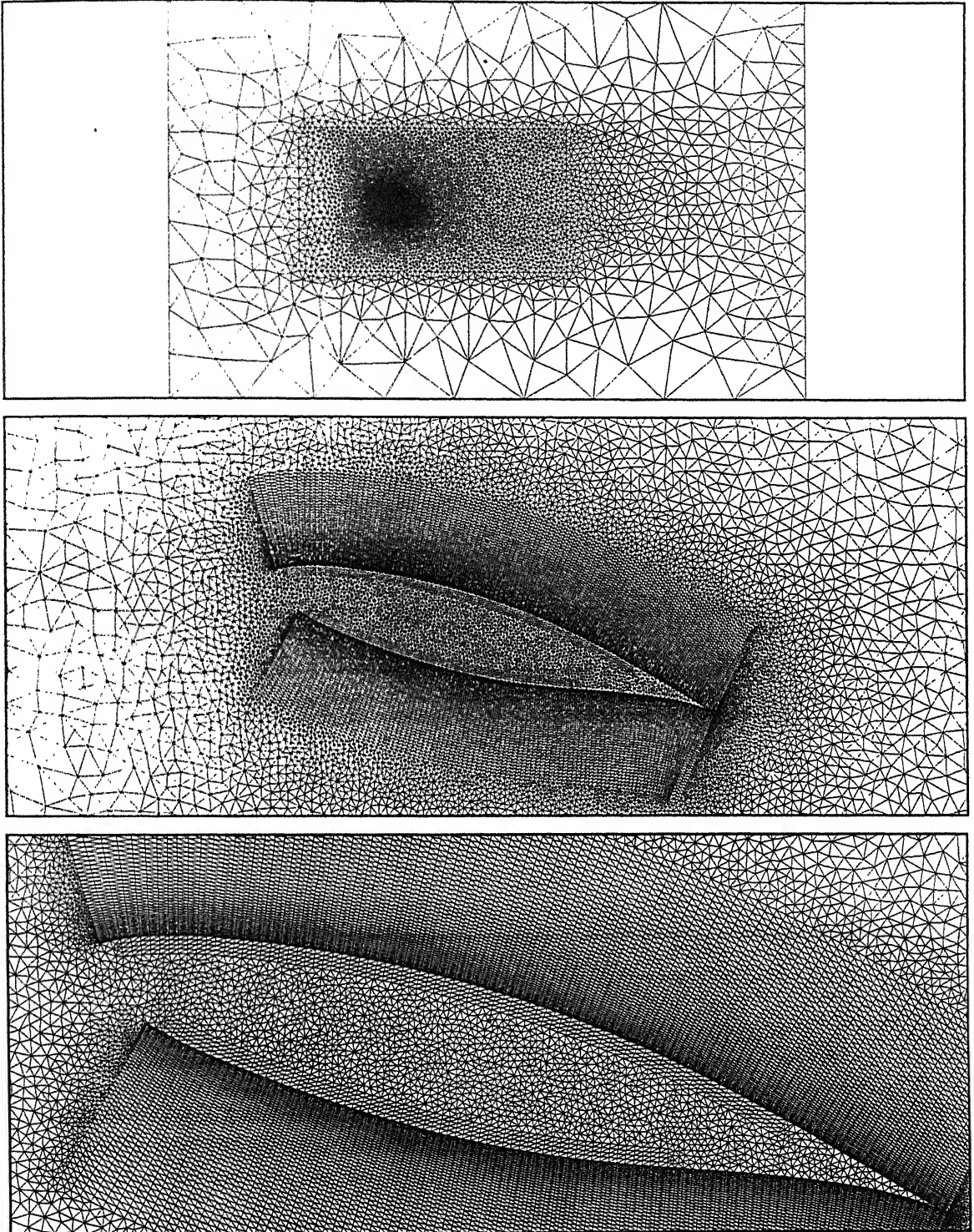


Figure 10: Flow past a ram-air parafoil with modified lower surface LS(1)0417 section: a typical finite element mesh employed for computations and its close-ups: The mesh consists of 21,409 nodes and 42,376 triangular elements  $x_{cut} = 0.1c$ ,  $\theta_{cut} = 135^\circ$ .

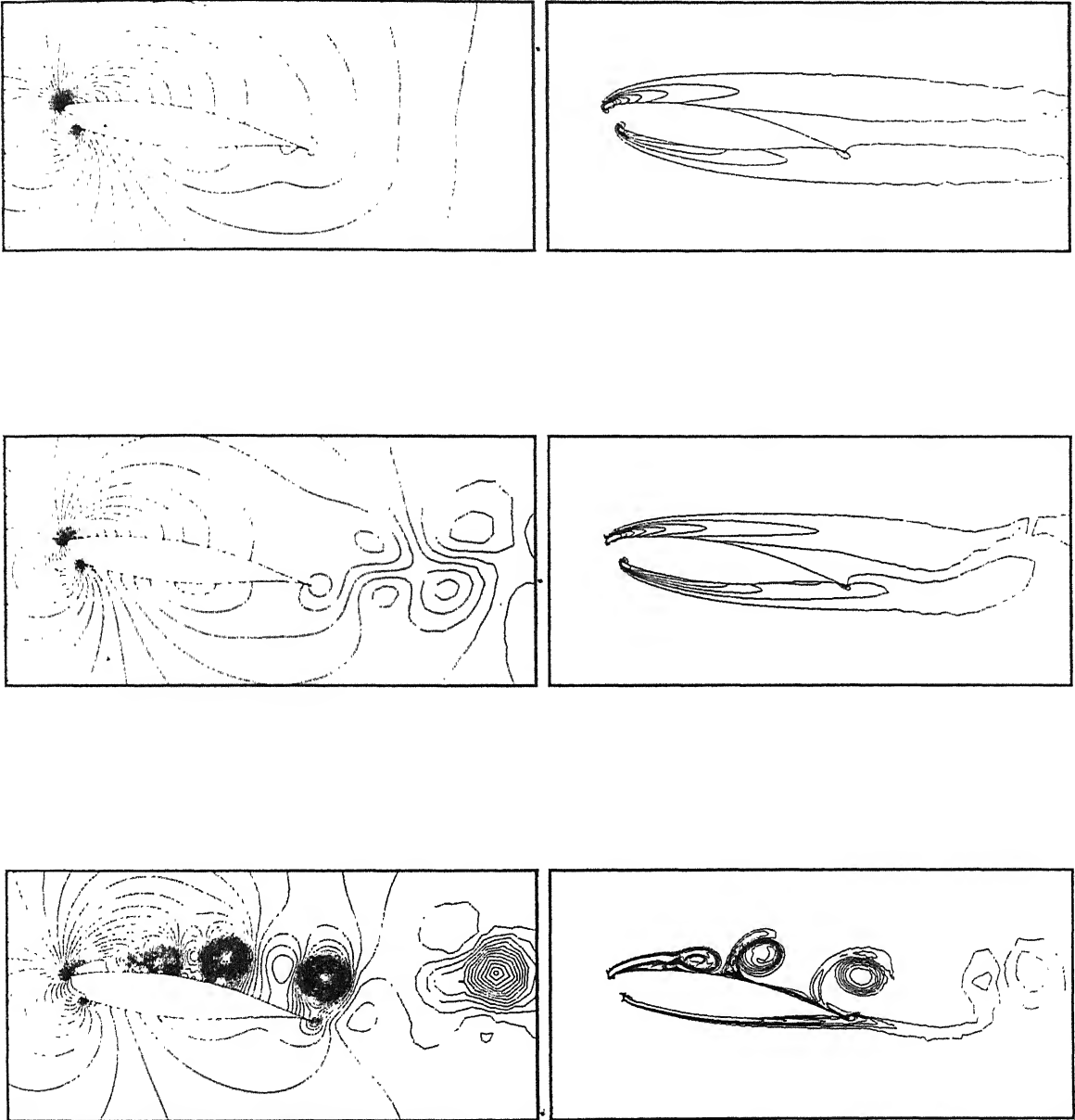


Figure 11:  $\alpha = 7.5^\circ$  flow past a ram air parafoil with modified lower surface LS(1) 0417 section: pressure(left), vorticity(right) fields from top to bottom  $Re = 500$ ,  $Re = 5000$  and  $Re = 10^4$ .

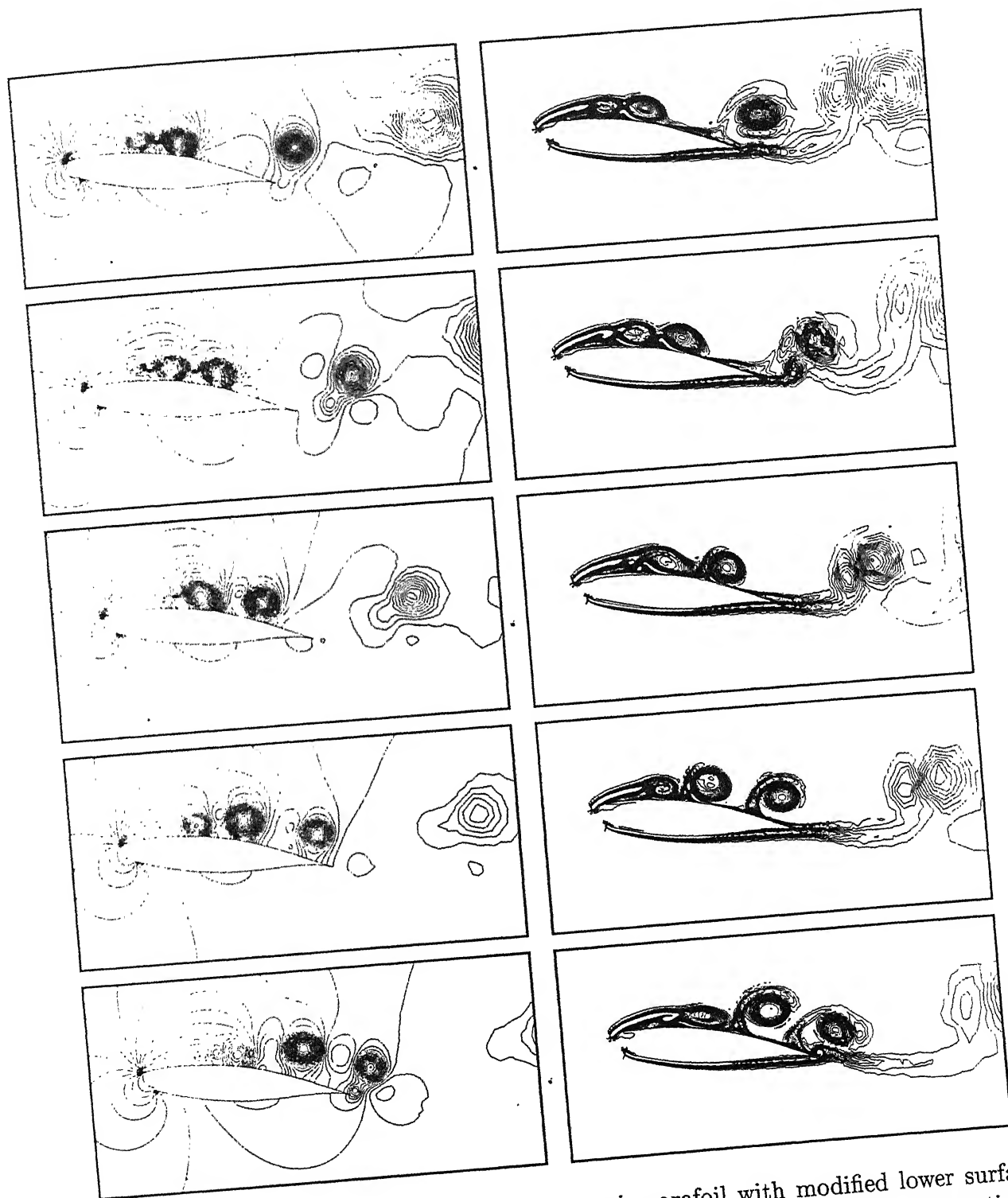


Figure 12:  $Re = 10^4$  laminar flow past a ram air parafoil with modified lower surface LS(1)0417 section  $x_{cut} = 0.1c$  and  $\theta_{cut} = 135^\circ$  at  $\alpha = 7.5^\circ$ : pressure (left) and vorticity (right) fields during one cycle of the lift coefficient variation for the developed unsteady solution.

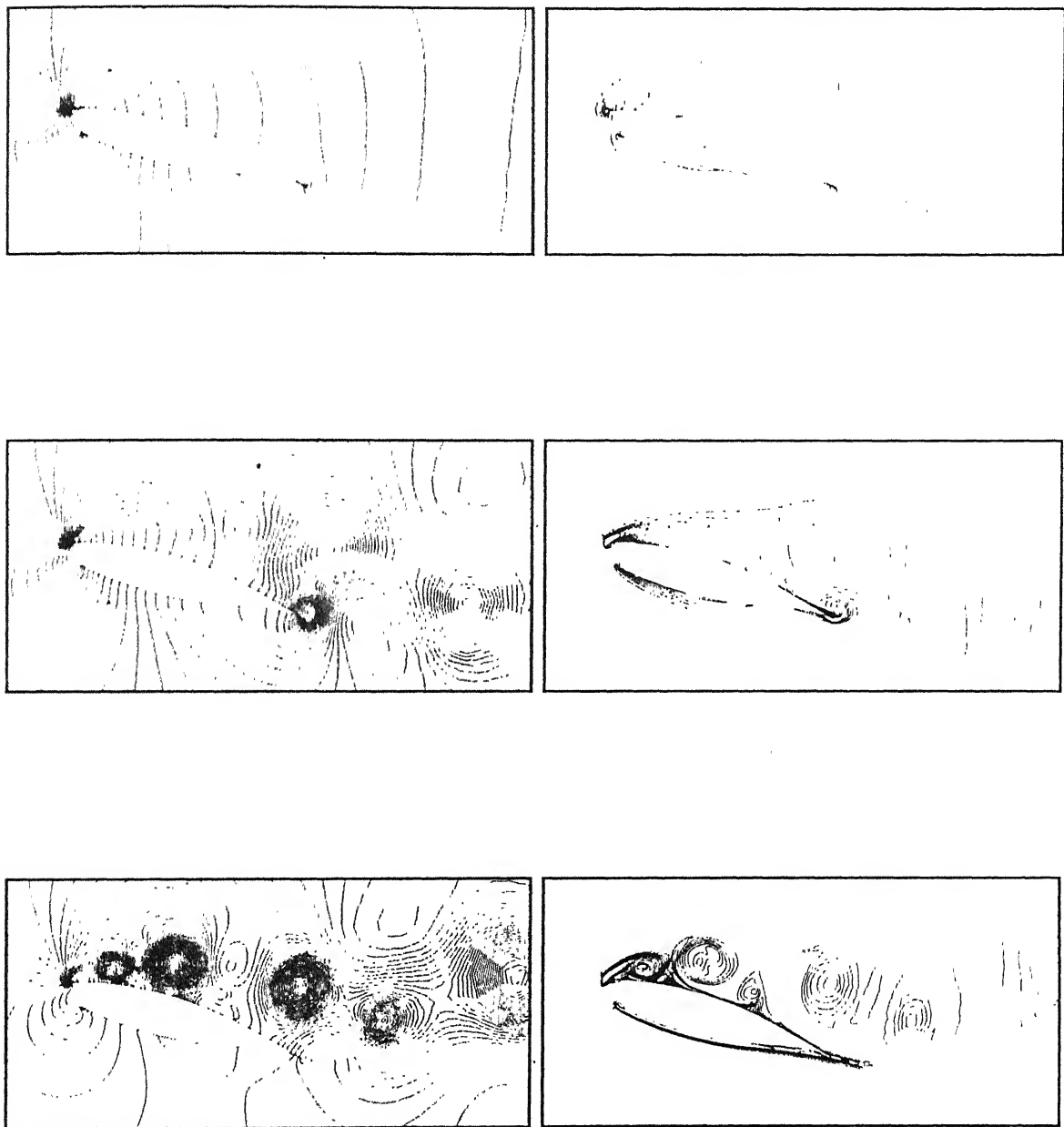


Figure 13:  $\alpha = 15^\circ$  laminar flow past a ram air parafoil with modified lower surface LS(1) 0417 section: pressure(left), vorticity(right) fields from top to bottom  $Re = 500$ ,  $Re = 5000$  and  $Re = 10^4$ .

पुरुषोत्तम काशीनाथ केनकर पुस्तकालय

भारतीय प्रौद्योगिकी संस्थान कानपुर

अवधि क्र० A 141802

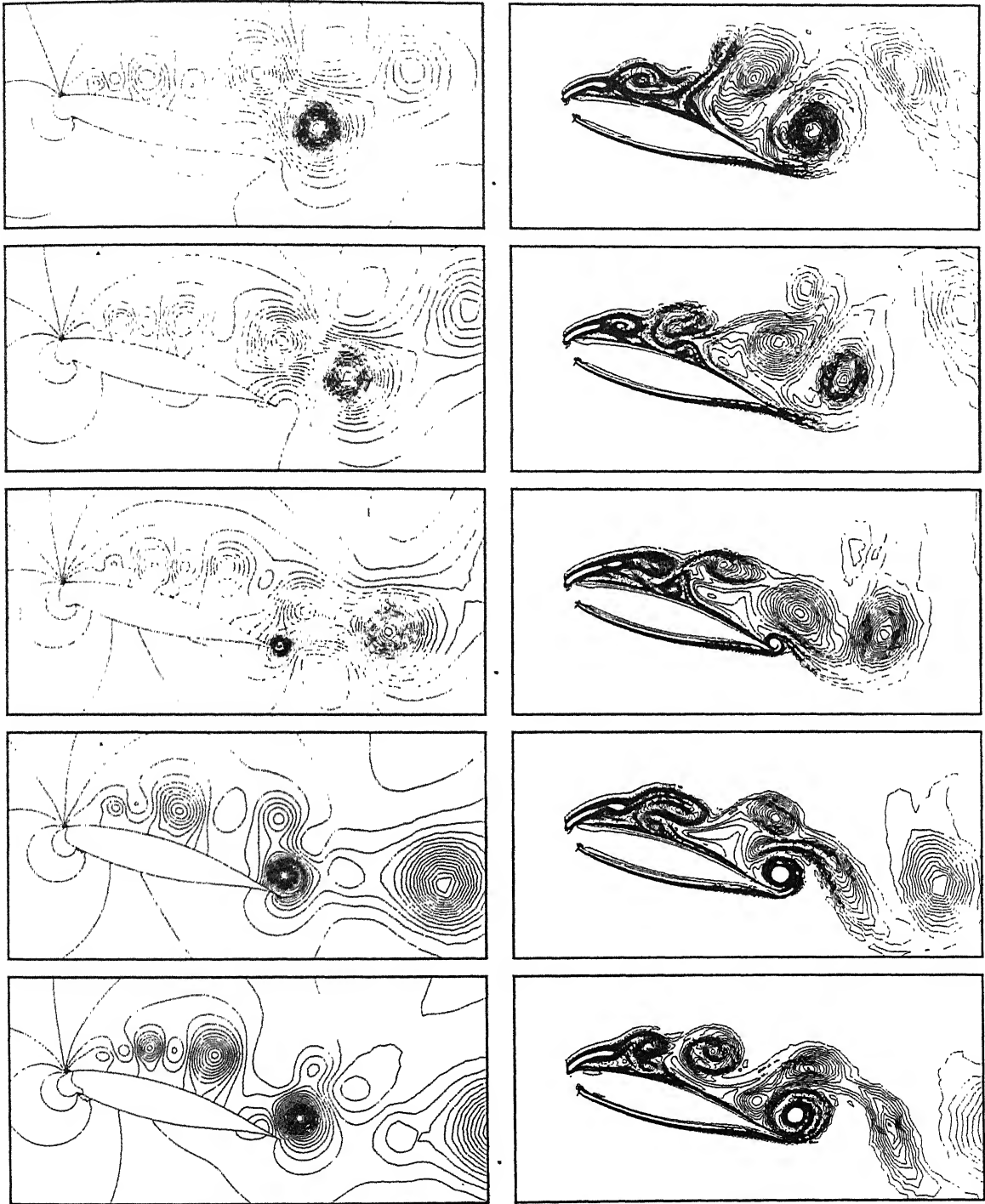


Figure 14:  $Re = 10^4$  laminar flow past a ram air parafoil with modified lower surface LS(1)0417 section  $x_{cut} = 0.1c$  and  $\theta_{cut} = 135^\circ$  at  $\alpha = 15^\circ$ : pressure (left) and vorticity (right) fields during one cycle of the lift coefficient variation for the developed unsteady solution.

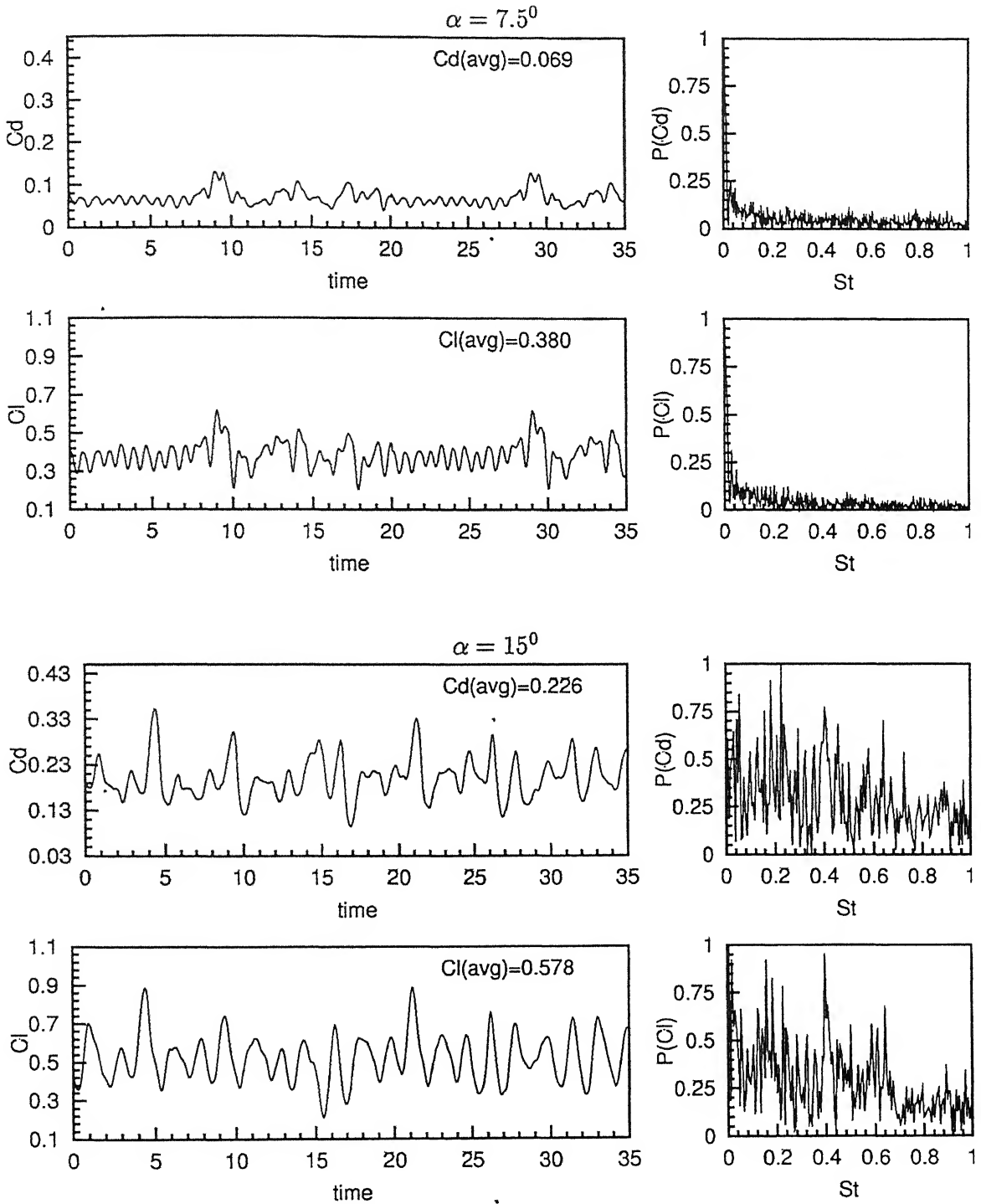


Figure 15:  $Re = 10^4$  laminar flow past a ram air parafoil with modified lower surface LS(1)0417 section  $x_{cut} = 0.1c$  and  $\theta_{cut} = 135^\circ$  at  $\alpha = 7.5^\circ, 15^\circ$ : time histories of the lift and drag coefficients and their power spectra.



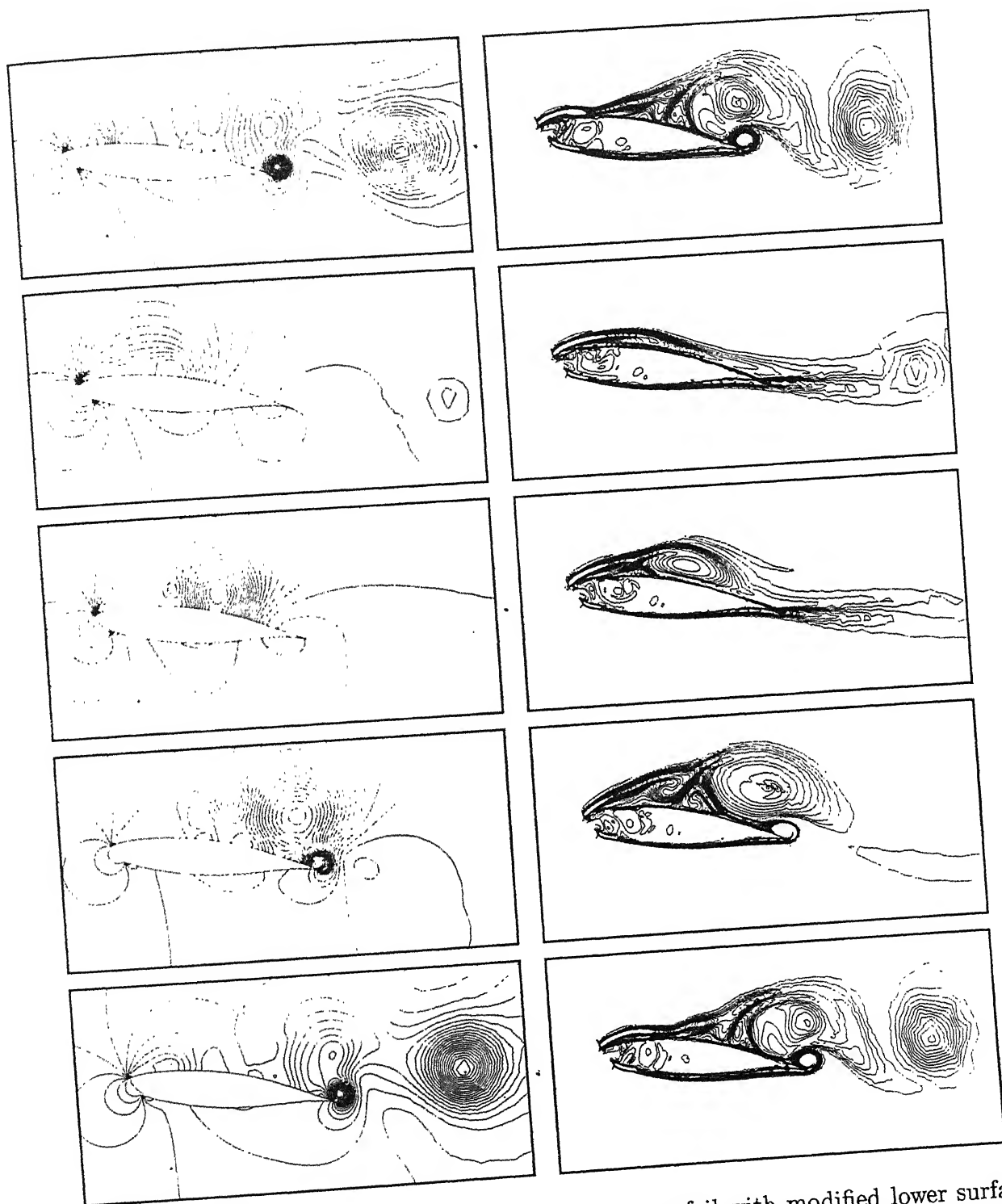
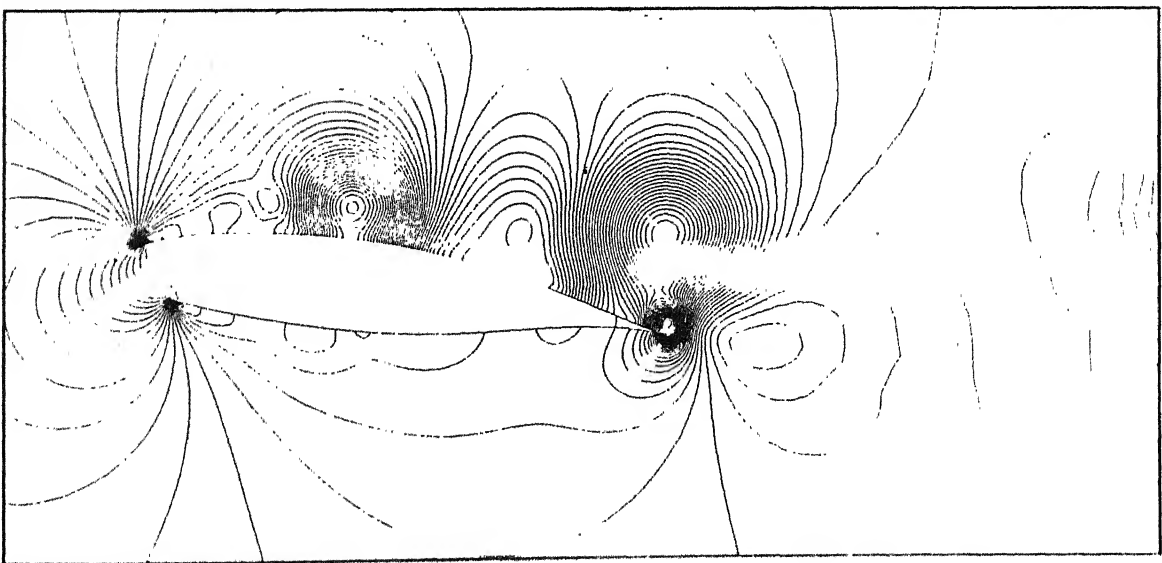
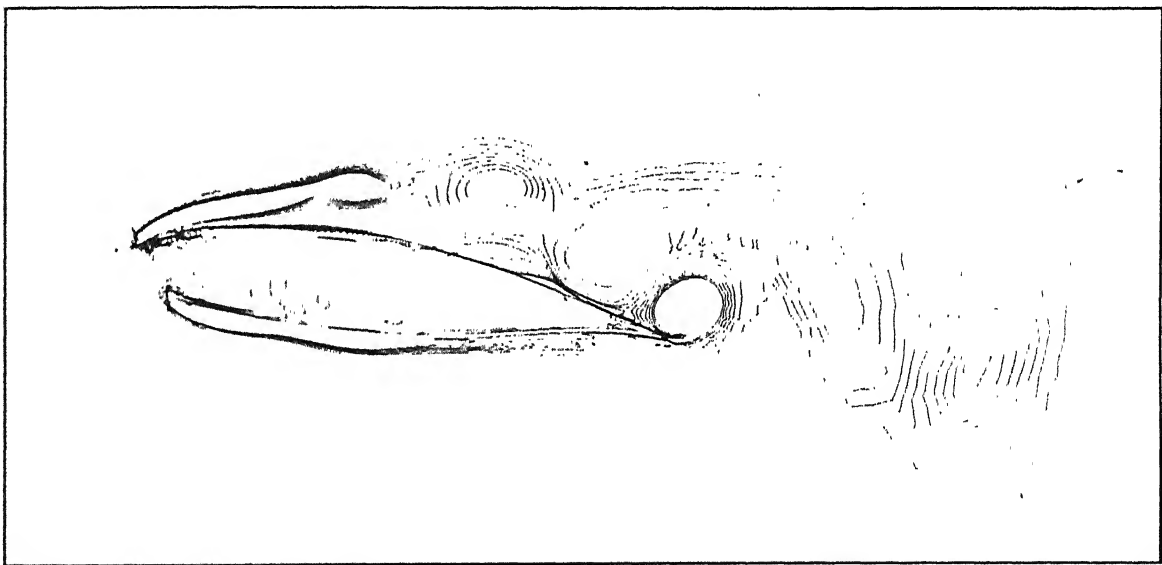
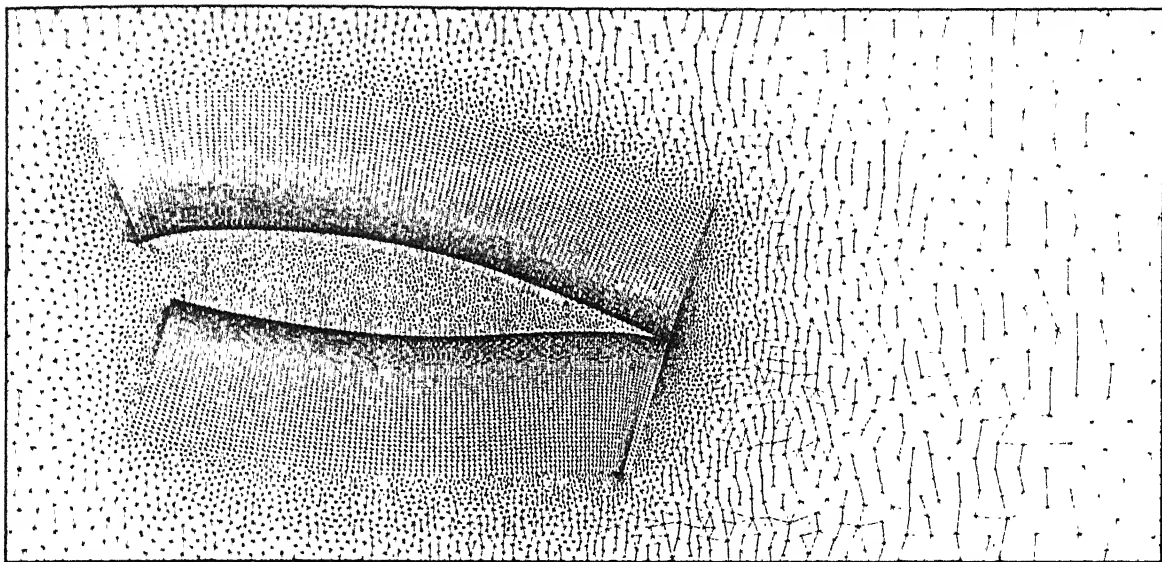


Figure 16:  $Re = 10^6$  turbulent flow past a ram air parafoil with modified lower surface LS(1)0417 section  $x_{cut} = 0.1c$  and  $\theta_{cut} = 135^\circ$  at  $\alpha = 7.5^\circ$ : pressure (left) and vorticity (right) fields during one cycle of the lift coefficient variation for the developed unsteady solution.



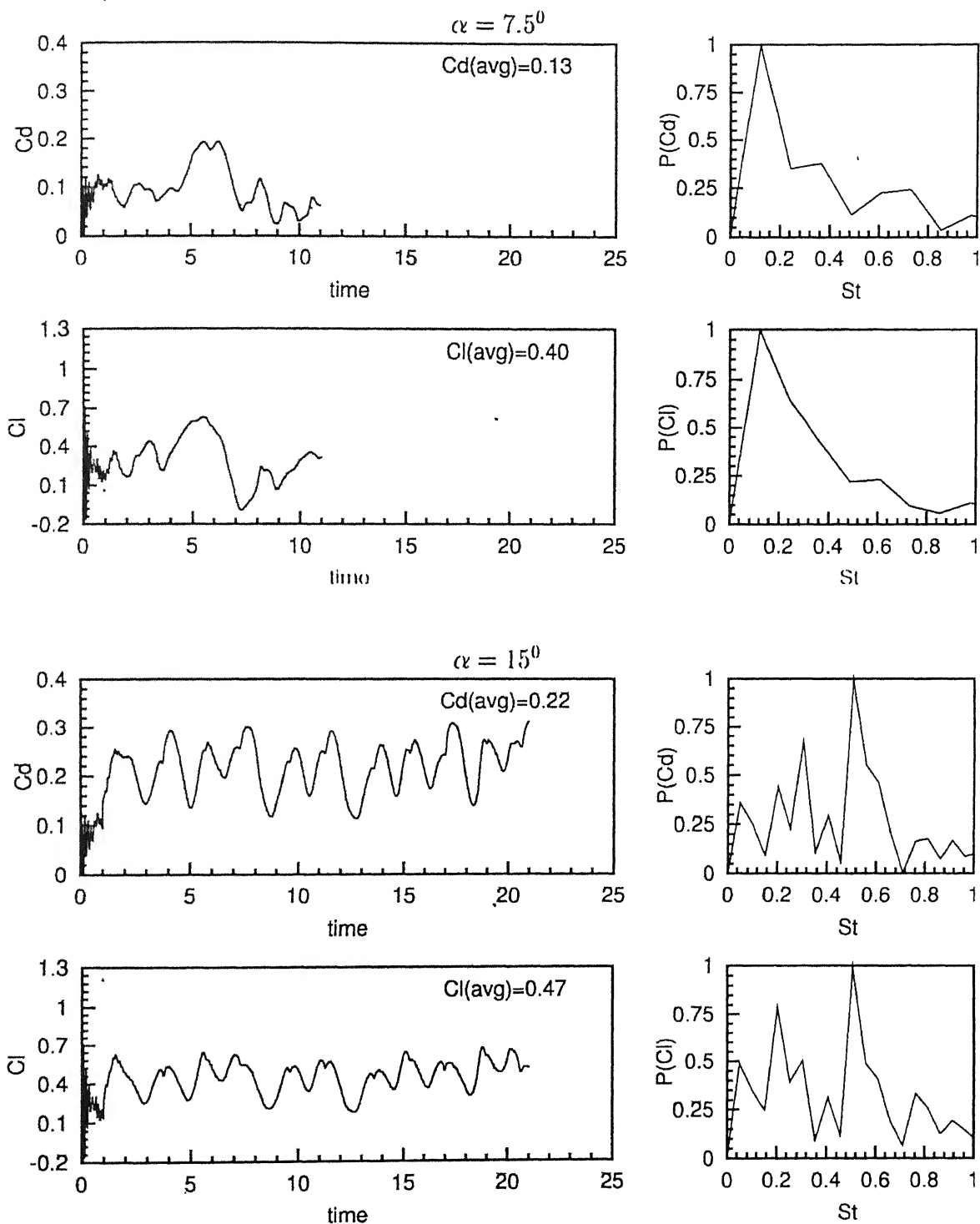


Figure 18:  $Re = 10^6$  turbulent flow past a ram air parafoil with LS(1)0417 section  $x_{cut} = 0.1c$  and  $\theta_{cut} = 135^\circ$  at  $\alpha = 7.5^\circ, 15^\circ$ : time histories of the lift and drag coefficients and their power spectra.

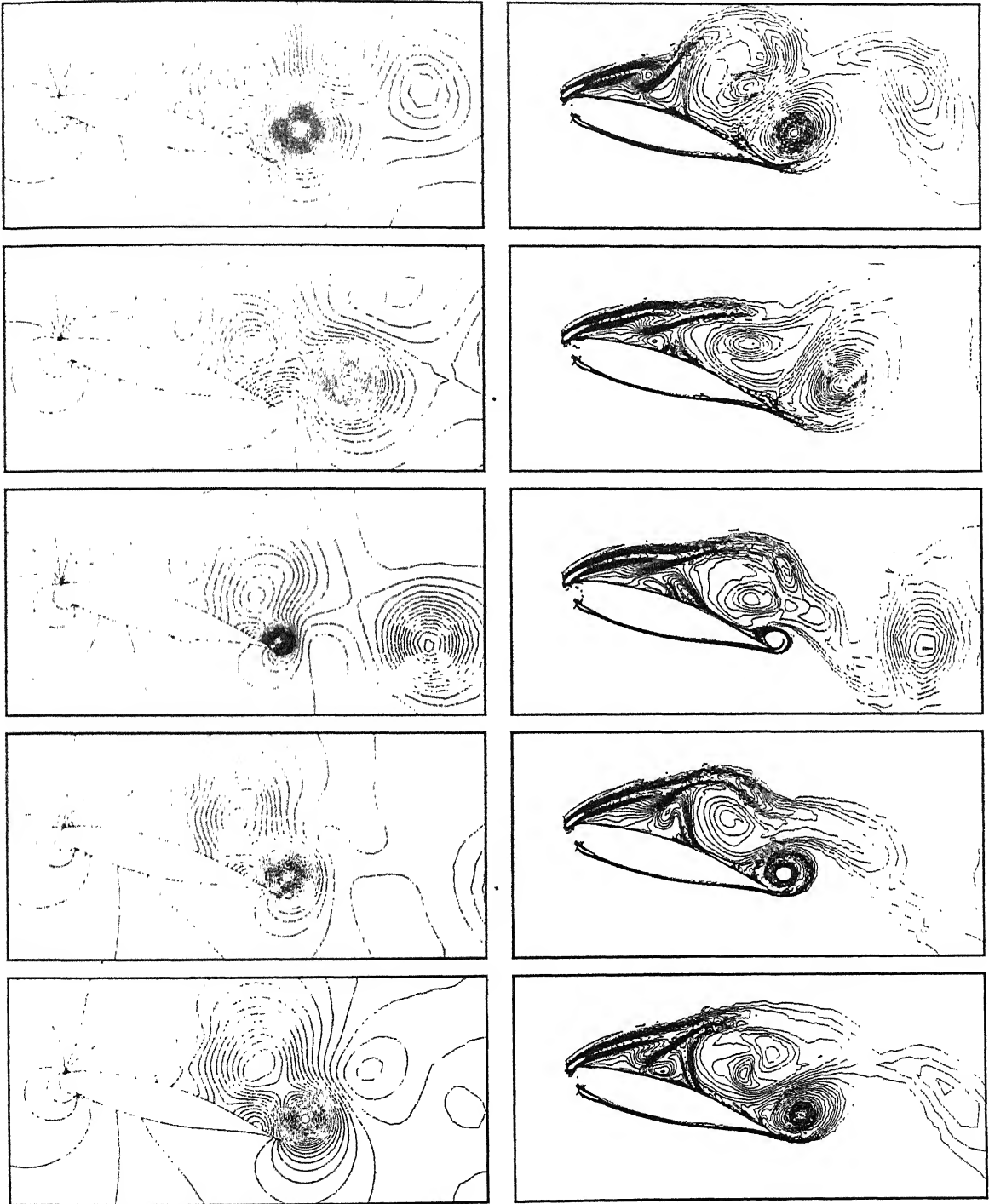


Figure 19:  $Re = 10^6$  turbulent flow past a ram air parafoil with modified lower surface LS(1)0417 section  $x_{cut} = 0.1c$  and  $\theta_{cut} = 135^\circ$  at  $\alpha = 15^\circ$ : pressure (left) and vorticity (right) fields during one cycle of the lift coefficient variation for the developed unsteady solution.

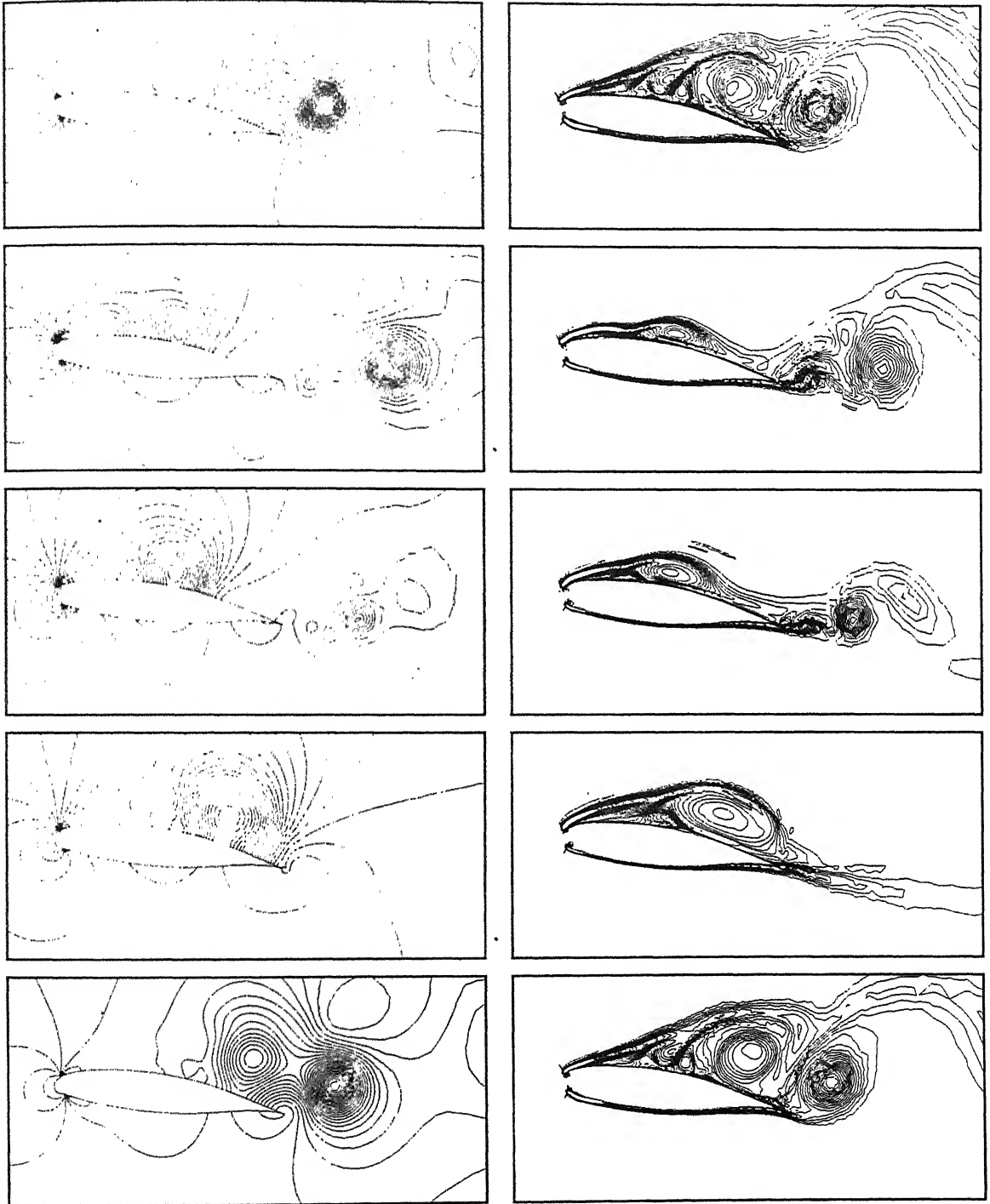


Figure 21:  $Re = 10^6$  turbulent flow past a ram air parafoil with LS(1)0417 section  $x_{cut} = 0.05c$  and  $\theta_{cut} = 135^\circ$  at  $\alpha = 7.5^\circ$ : pressure (left) and vorticity (right) fields during one cycle of the lift coefficient variation for the developed unsteady solution.

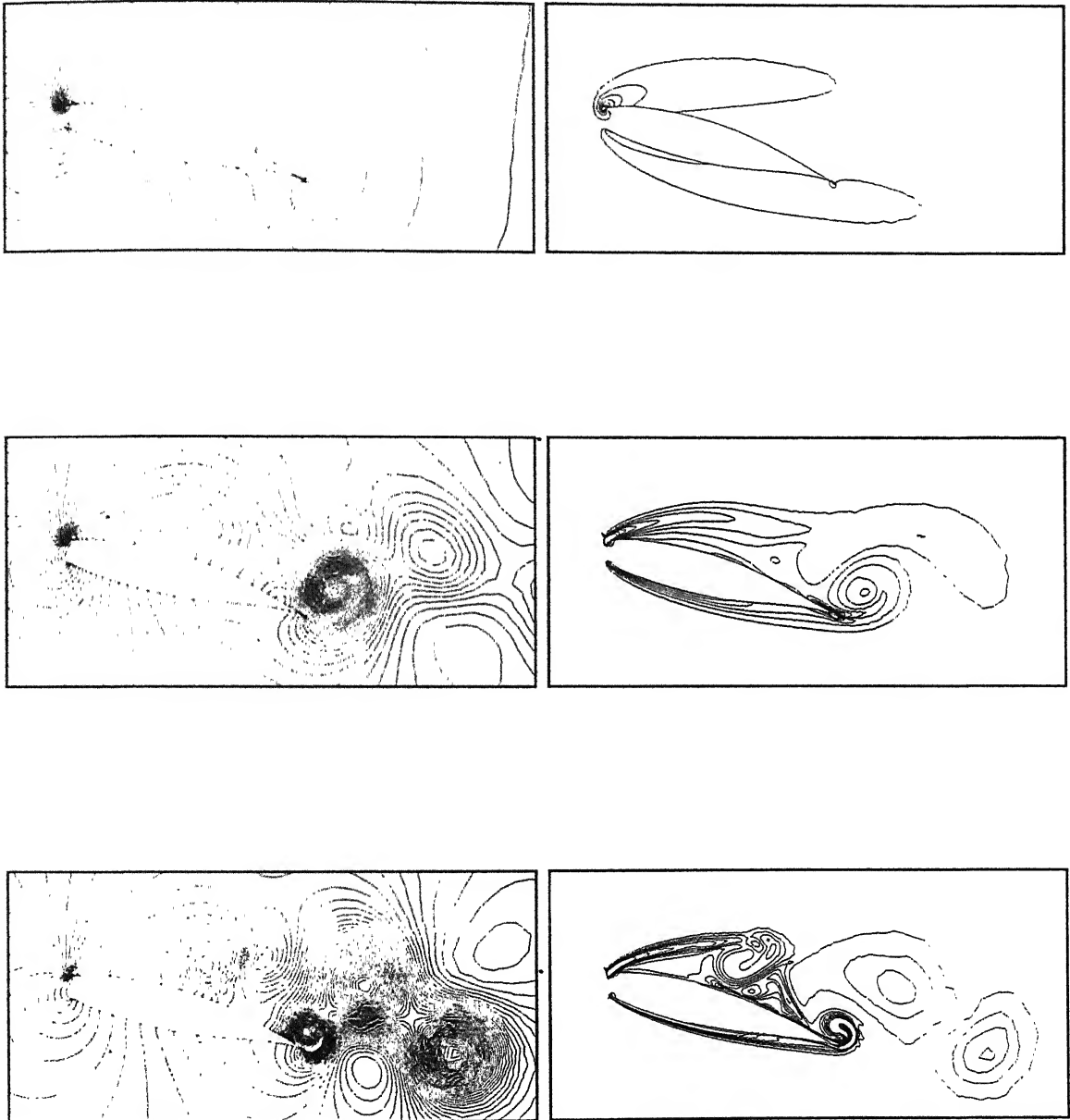


Figure 22:  $\alpha = 15^\circ$ , laminar flow past a ram air parafoil with LS(1) 0417 section: pressure(left), vorticity(right) fields from top to bottom  $Re = 500$ ,  $Re = 5000$  and  $Re = 10^4$ .

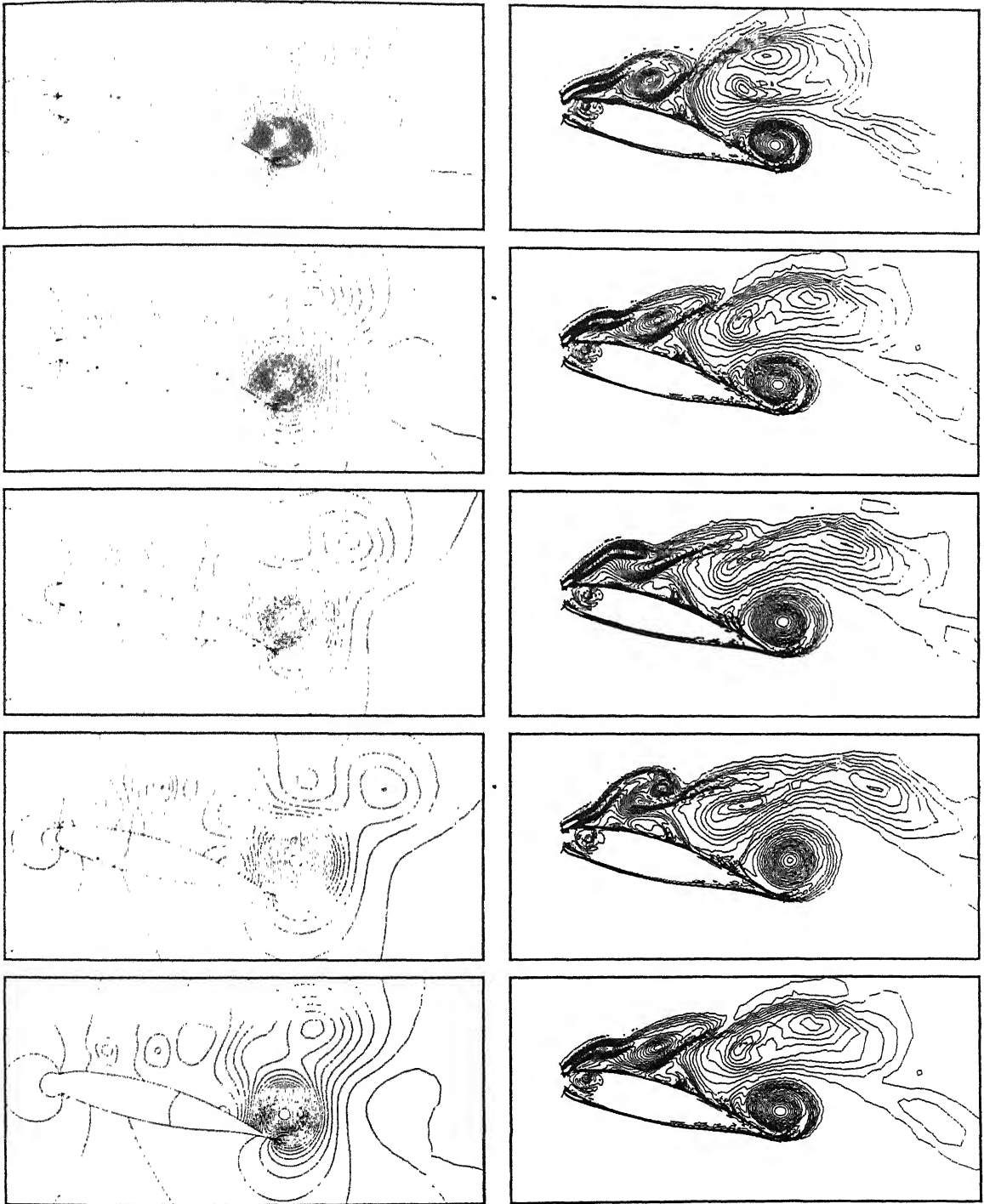


Figure 23:  $Re = 10^6$  turbulent flow past a ram air parafoil with LS(1)0417 section  $x_{cut} = 0.05c$  and  $\theta_{cut} = 135^\circ$  at  $\alpha = 15^\circ$ : pressure (left) and vorticity (right) fields during one cycle of the lift coefficient variation for the developed unsteady solution.

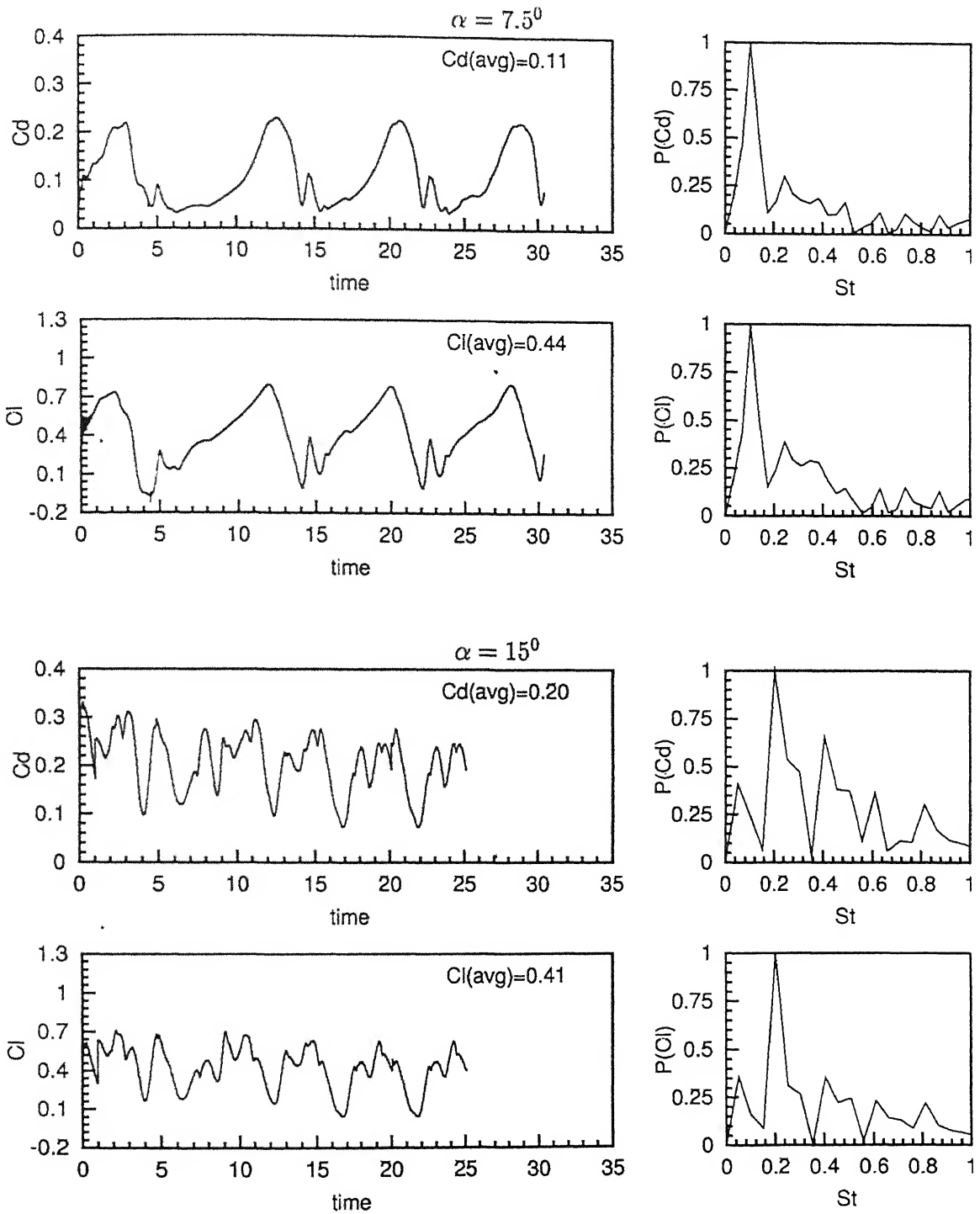


Figure 24:  $Re = 10^6$  turbulent flow past a ram air parafoil with modified lower surface LS(1)0417 section  $x_{cut} = 0.1c$  and  $\theta_{cut} = 135^\circ$  at  $\alpha = 7.5^\circ, 15^\circ$ : time histories of the lift and drag coefficients and their power spectra.



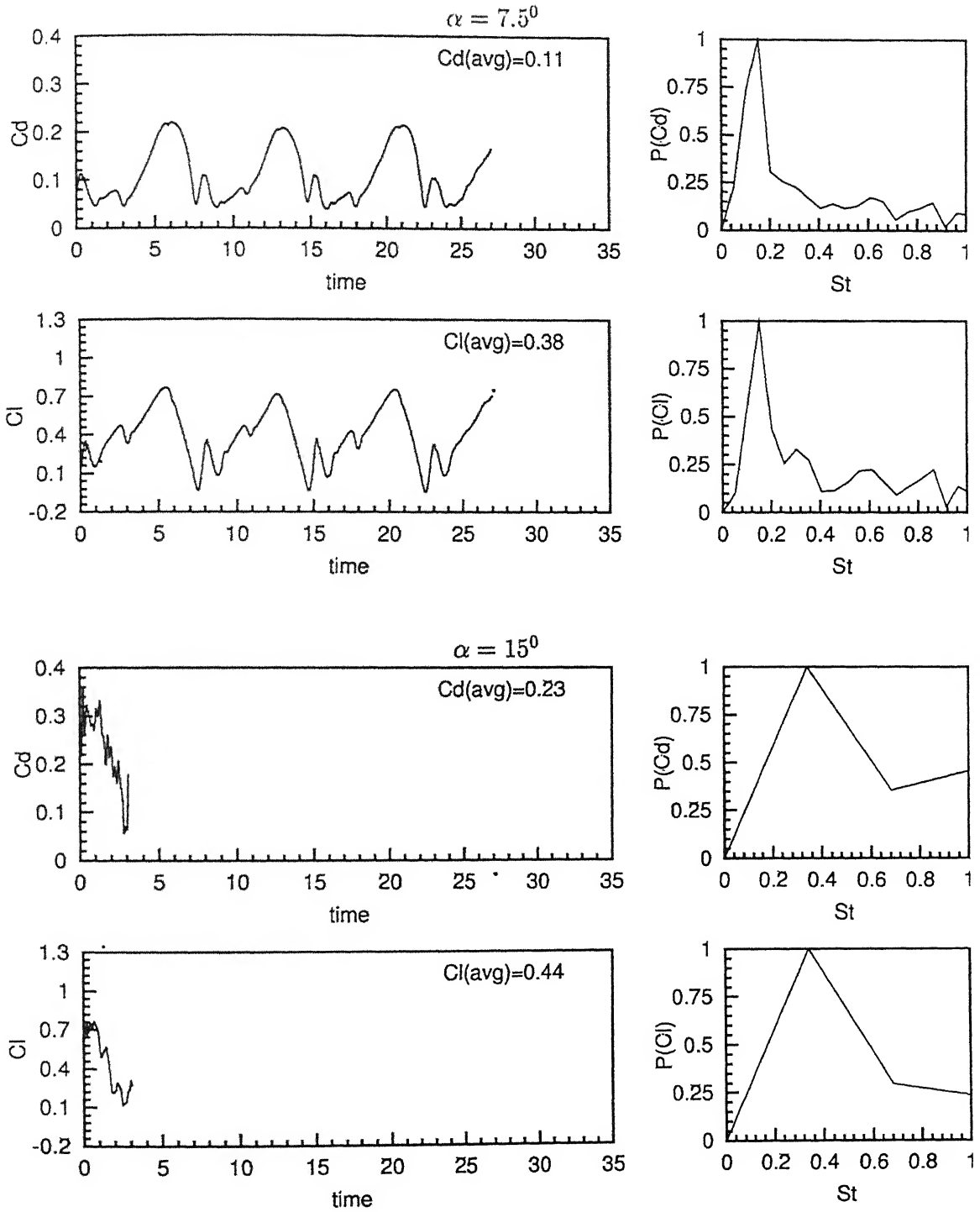


Figure 25:  $Re = 10^6$  turbulent flow past a ram air parafoil with LS(1)0417 section  $x_{cut} = 0.05c$  and  $\theta_{cut} = 135^\circ$  at  $\alpha = 7.5^\circ, 15^\circ$ : time histories of the lift and drag coefficients and their power spectra.

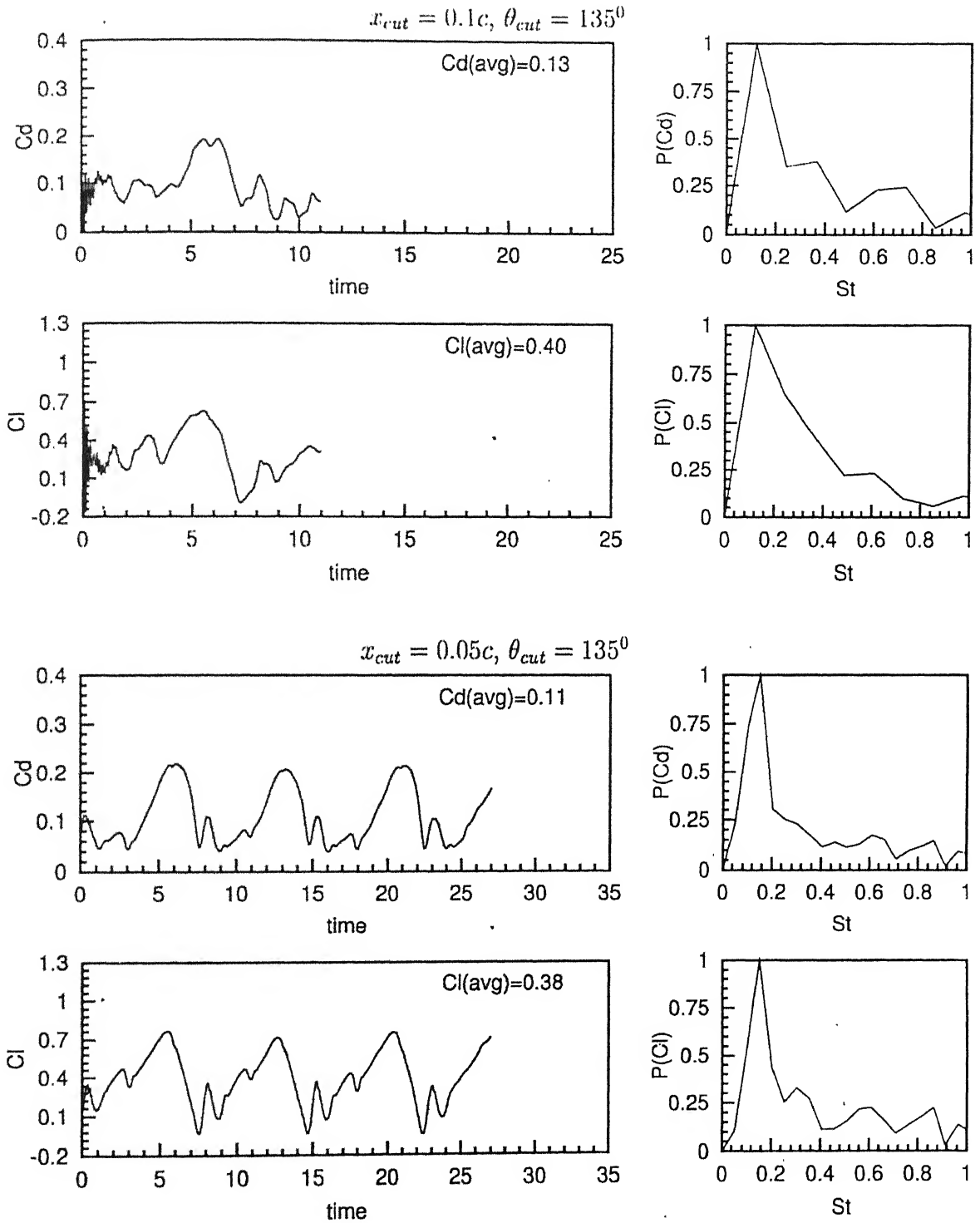


Figure 26:  $Re = 10^6$  turbulent flow past a ram air parafoil with LS(1)0417 section at  $\alpha = 7.5^\circ$ : time histories of the lift and drag coefficients and their power spectra for modified lower surface and exact LS(1)0417 for two configuration of leading edge cut.

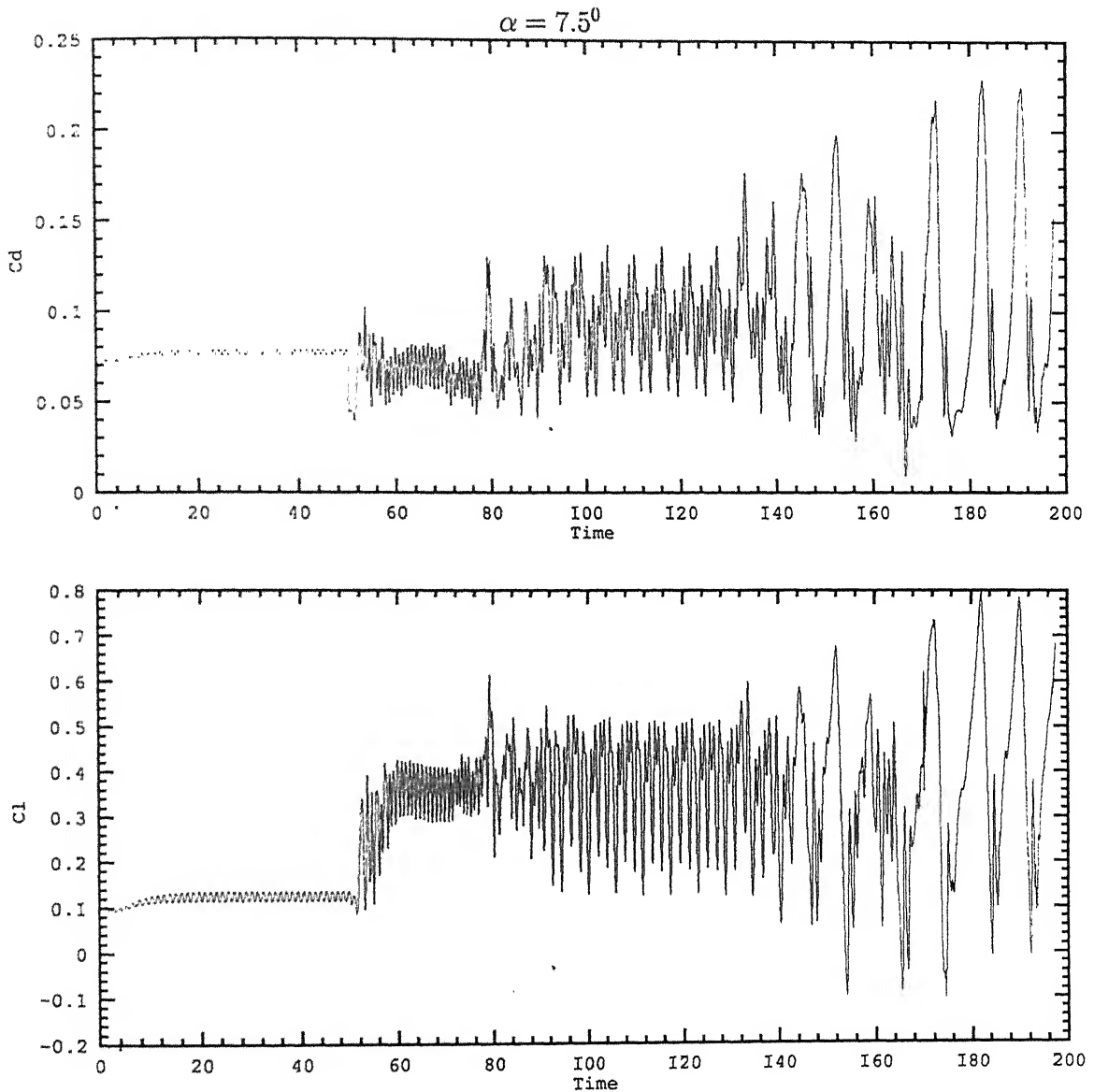


Figure 27: Flow past a ram-air parafoil with modified lower surface LS(1)0417 section  $x_{cut} = 0.1c$ ,  $\theta_{cut} = 135^\circ$ : time histories of the lift and drag coefficients,  $Re = 10^3$  for  $0 \leq t \leq 50$ ,  $Re = 5 \times 10^3$  for  $50 \leq t \leq 70$ ,  $Re = 10^4$  for  $70 \leq t \leq 90$ ,  $Re = 5 \times 10^4$  for  $90 \leq t \leq 130$ ,  $Re = 10^5$  for  $130 \leq t \leq 170$ ,  $Re = 10^6$  for  $170 \leq t \leq 198$ . The turbulence model was turned on at  $t = 90.0$ .

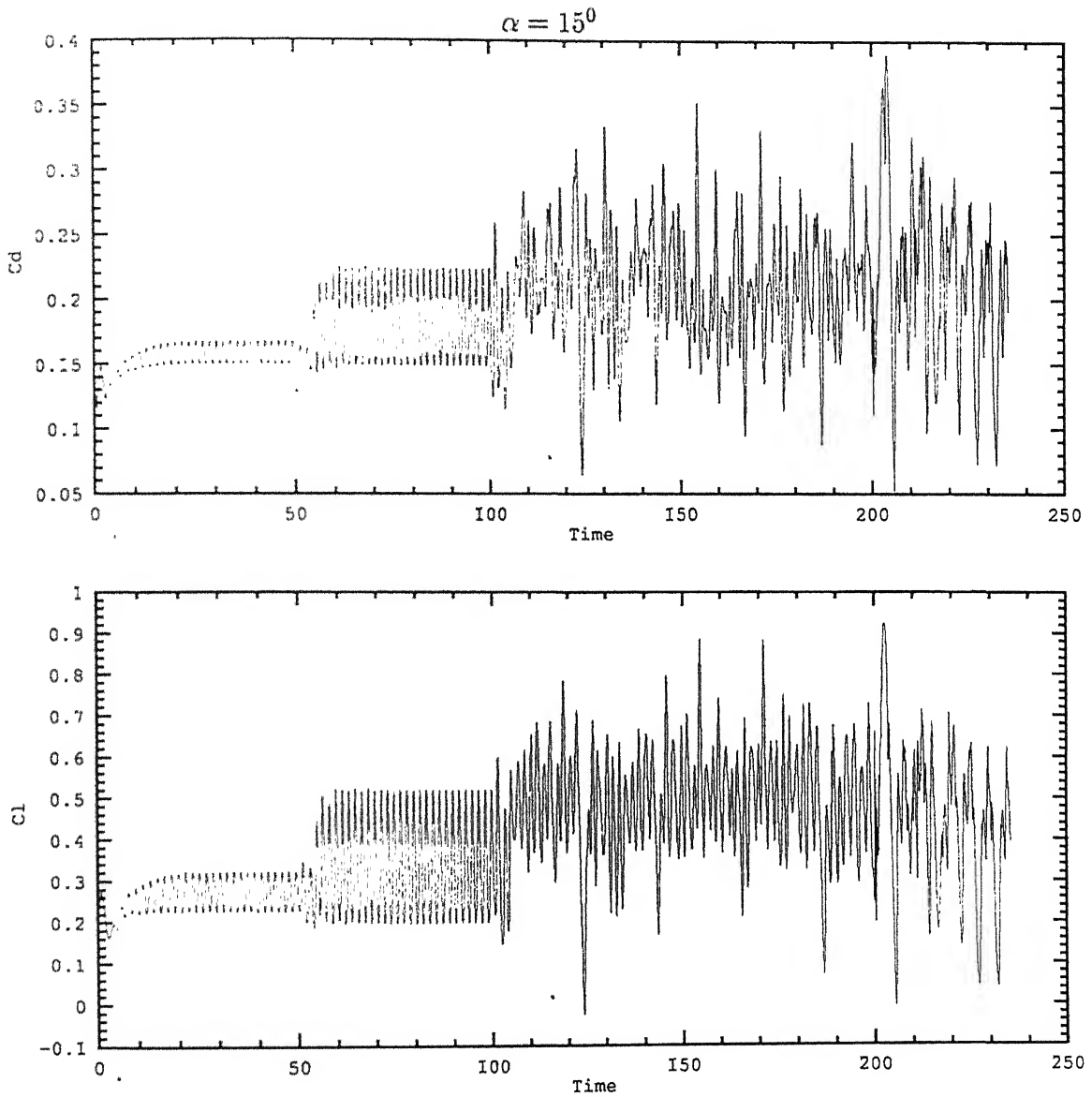


Figure 28: Flow past a ram-air parafoil with modified lower surface LS(1)0417 section  $x_{cut} = 0.1c$ ,  $\theta_{cut} = 135^\circ$ : time histories of the lift and drag coefficients,  $Re = 5 \times 10^2$  for  $0 \leq t \leq 50$ ,  $Re = 10^3$  for  $50 \leq t \leq 100$ ,  $Re = 5 \times 10^3$  for  $100 \leq t \leq 150$ ,  $Re = 10^4$  for  $150 \leq t \leq 200$ ,  $Re = 10^5$  for  $200 \leq t \leq 210$ ,  $Re = 10^6$  for  $210 \leq t \leq 235$ . The turbulence model was turned on at  $t = 200.0$ .

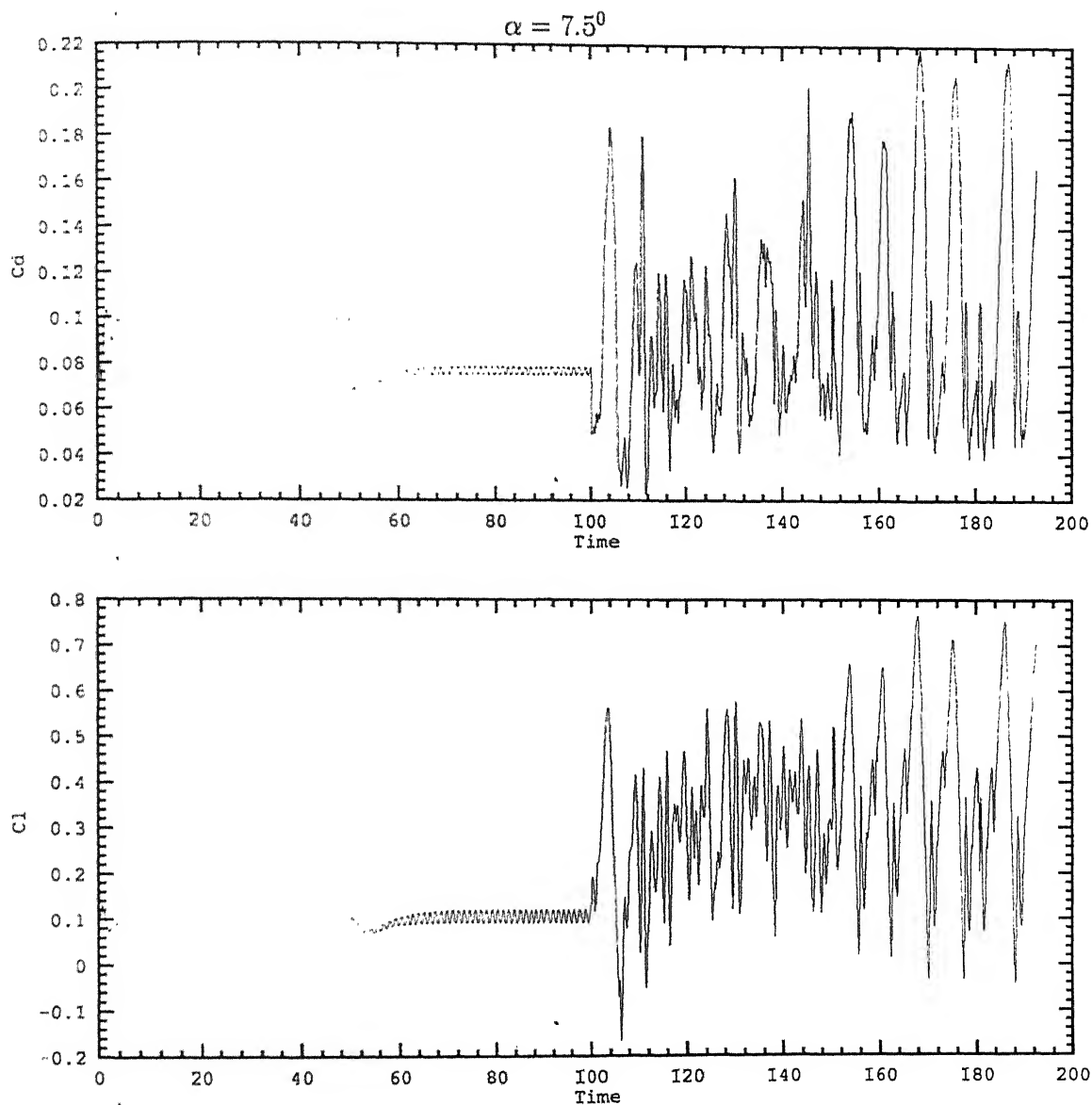


Figure 29: Flow past a ram-air parafoil with LS(1)0417 section  $x_{cut} = 0.05c$ ,  $\theta_{cut} = 135^\circ$ : time histories of the lift and drag coefficients,  $Re = 5 \times 10^2$  for  $0 \leq t \leq 50$ ,  $Re = 10^3$  for  $50 \leq t \leq 100$ ,  $Re = 10^4$  for  $100 \leq t \leq 150$ ,  $Re = 10^5$  for  $150 \leq t \leq 163$ ,  $Re = 10^6$  for  $163 \leq t \leq 190$ . The turbulence model was turned on at  $t = 150.0$ .

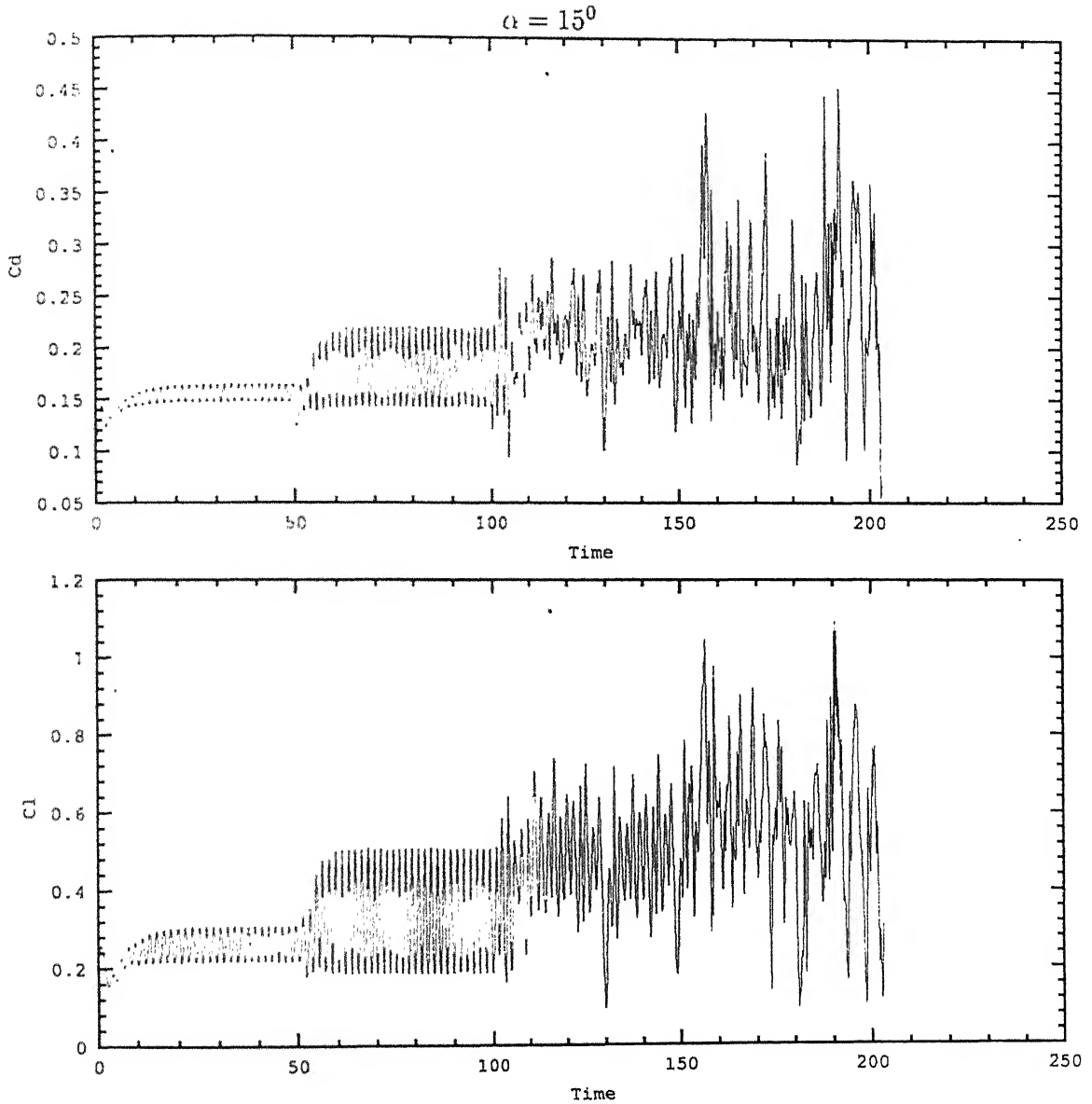


Figure 30: Flow past a ram-air parafoil with  $x_{cut} = 0.05c$ ,  $\theta_{cut} = 135^\circ$ : time histories of the lift and drag coefficients,  $Re = 5 \times 10^2$  for  $0 \leq t \leq 50$ ,  $Re = 10^3$  for  $50 \leq t \leq 100$ ,  $Re = 5 \times 10^3$  for  $100 \leq t \leq 150$ ,  $Re = 10^4$  for  $150 \leq t \leq 190$ ,  $Re = 10^5$  for  $190 \leq t \leq 200$ ,  $Re = 10^6$  for  $200 \leq t \leq 204$ . The turbulence model was turned on at  $t = 190.0$ .

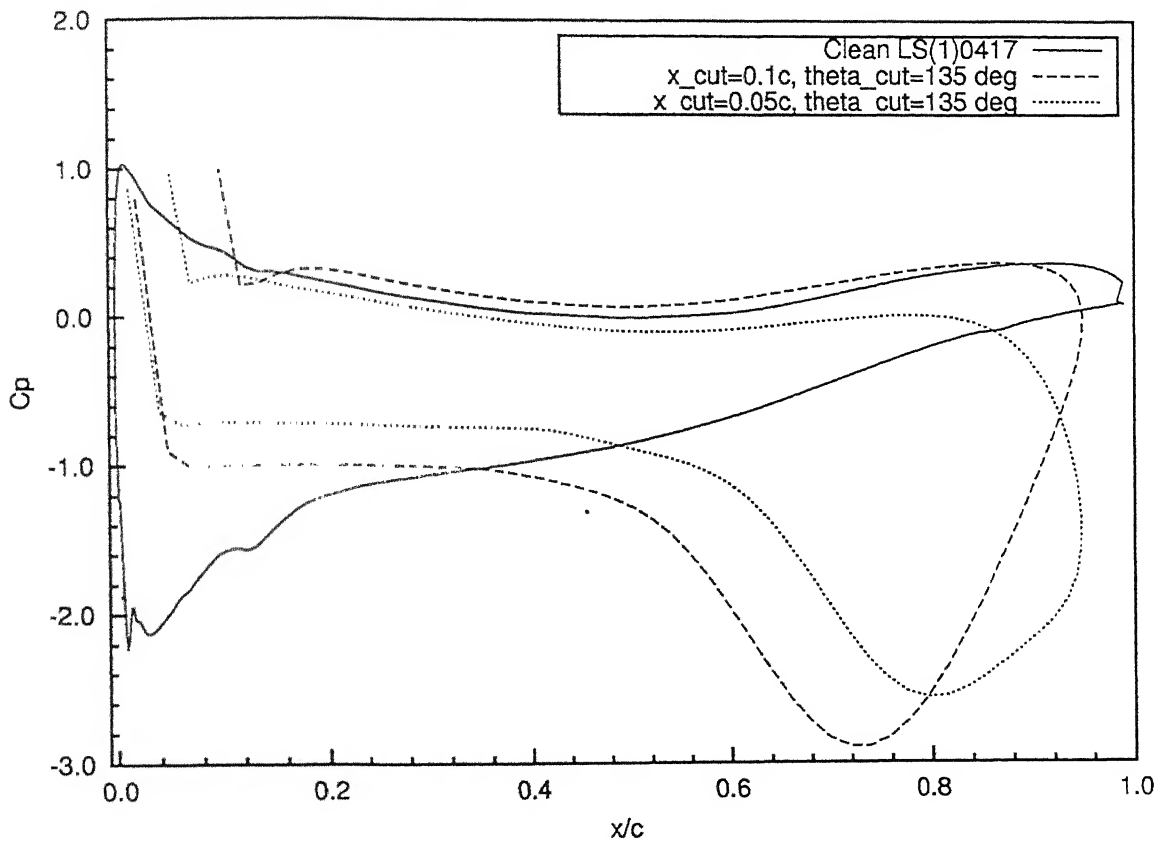


Figure 31:  $Re = 10^6$  turbulent flow past a ram-air parafoil with LS(1)0417 section and with modified lower surface at  $\alpha = 7.5^\circ$ : variation of the pressure coefficient along the outer surface of the parafoil corresponding to the peak value of the lift coefficient for two configurations of the leading edge cut.

nn-5821, ne-11410

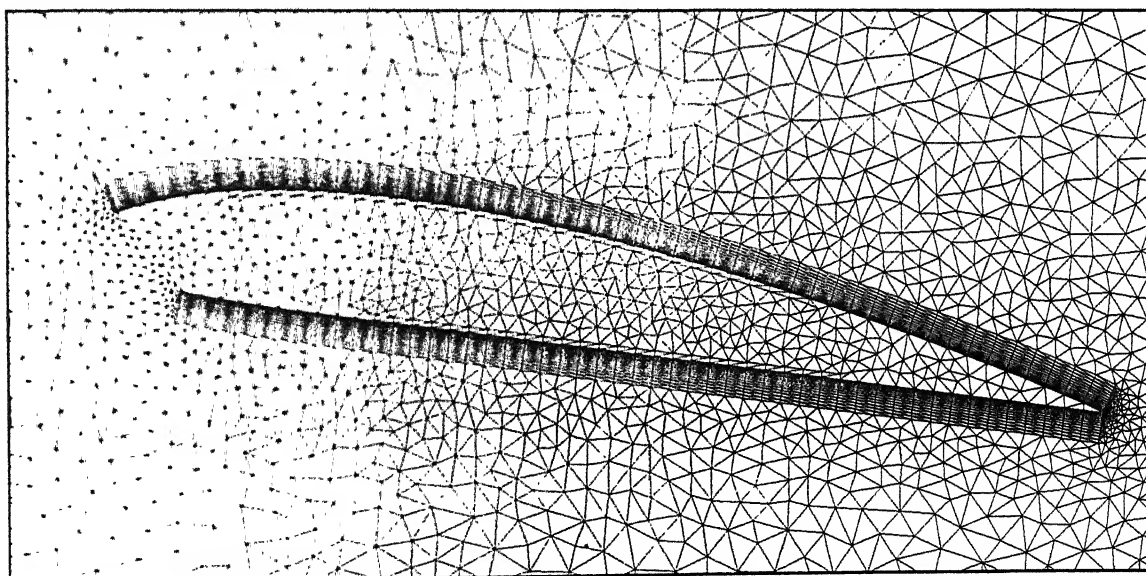
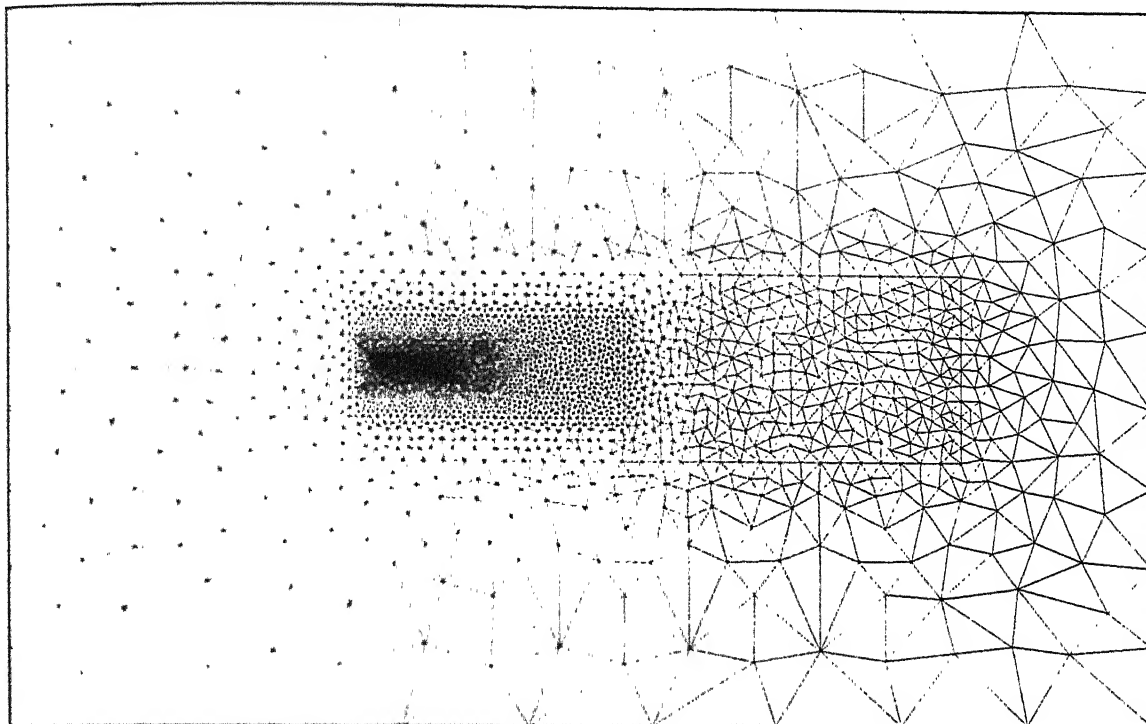
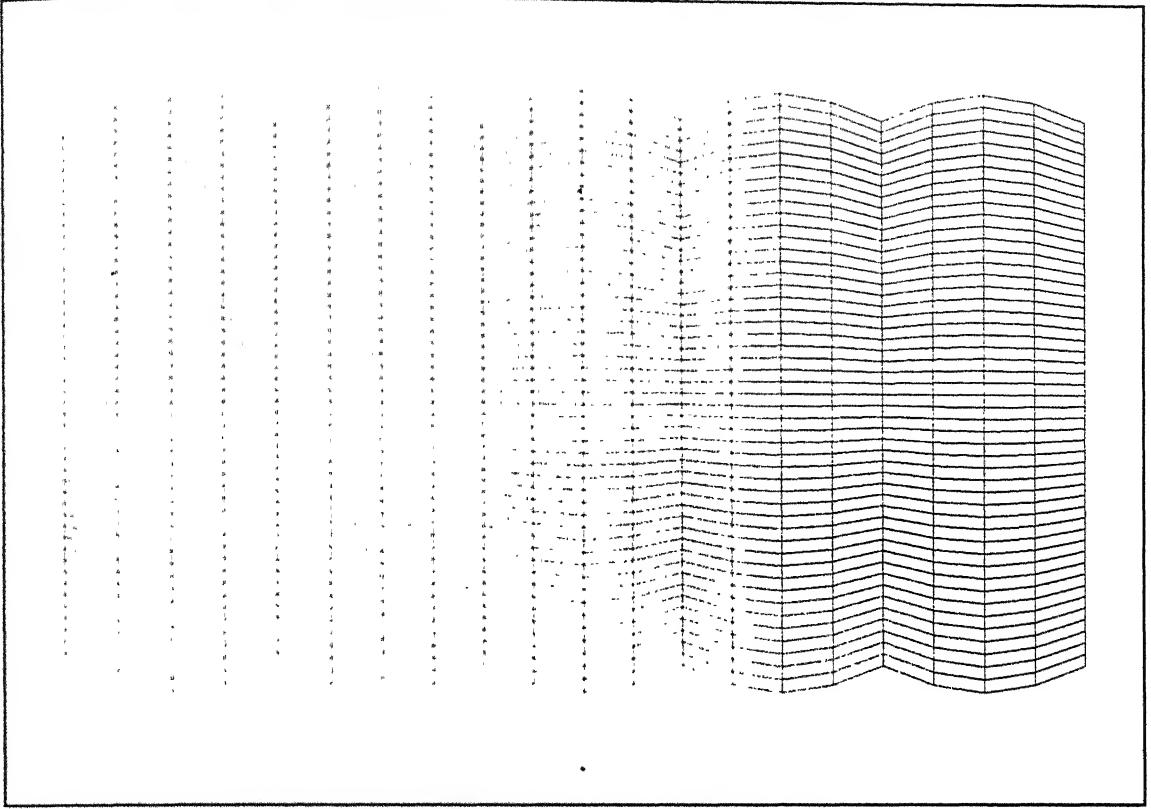


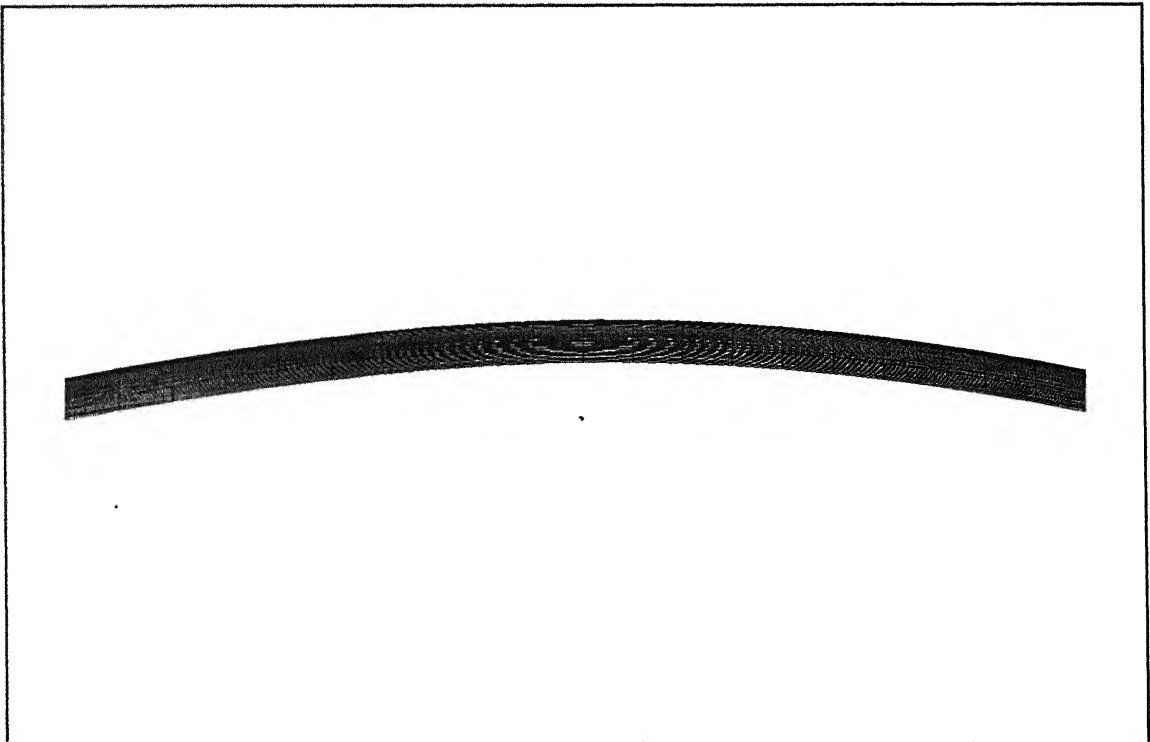
Figure 32: Flow past a Five cell ram-air parachute with Clark-Y section: a typical 2D section of the finite element mesh employed for the computations and its close-up view at  $\alpha = 7.5^\circ$ , each 2D section consists of 5,821 nodes and 11,410 triangular elements. The 3D mesh consists of 2,36,721 nodes and 4,56,400 wedge elements.

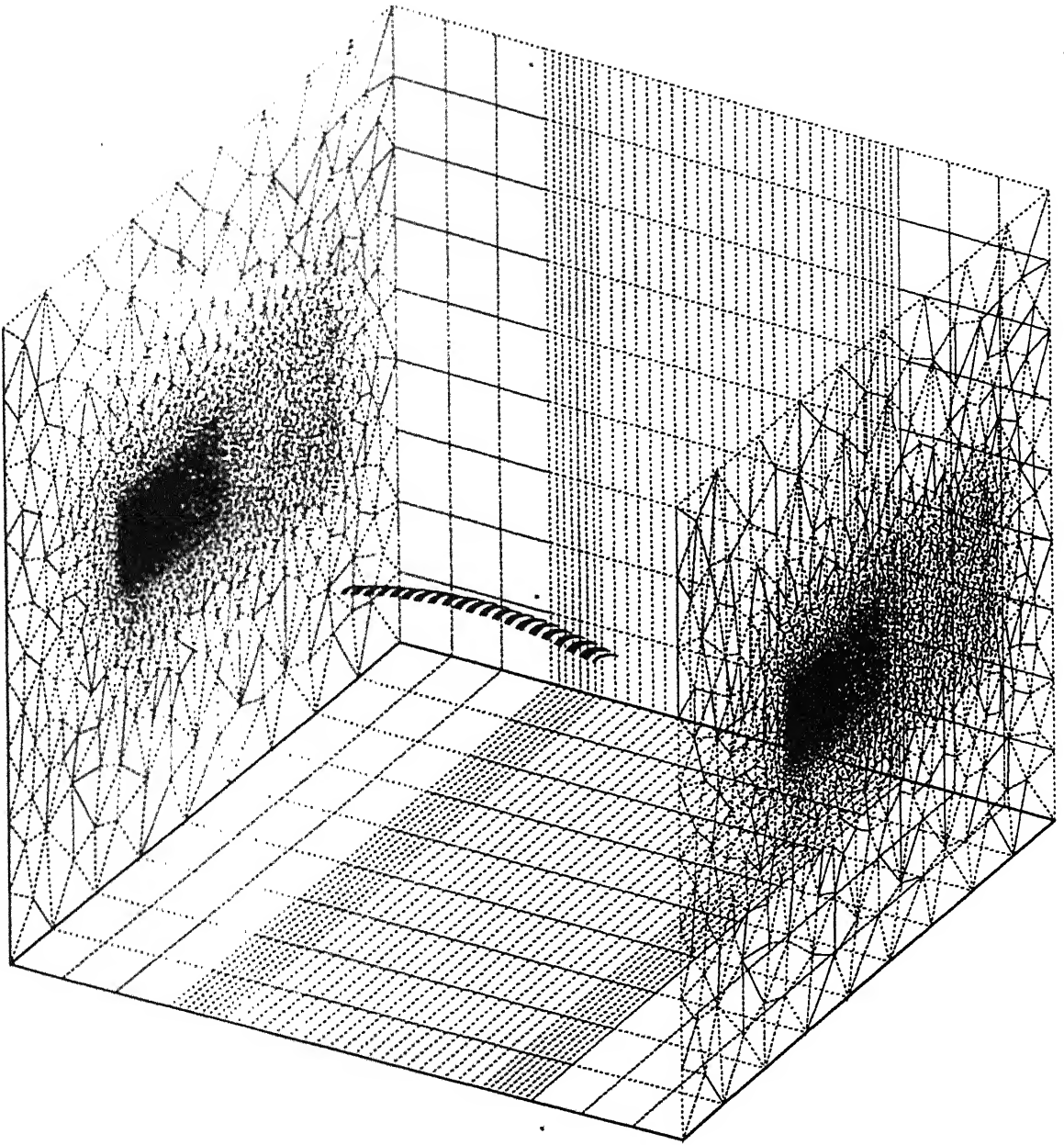


Top View of Parachute



Front View of Parachute





. Figure 34: Five cell Ram-air parachute lying in a rectangular box.

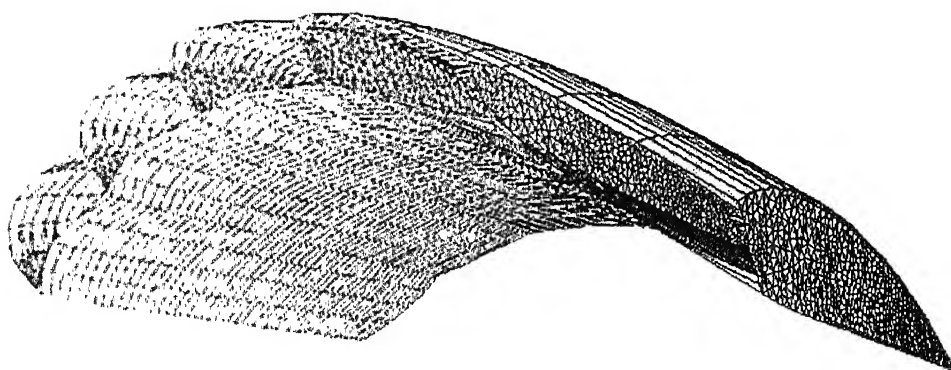


Figure 35: 3D view of Five cell Ram-air parachute: mesh on the parachute fabric.

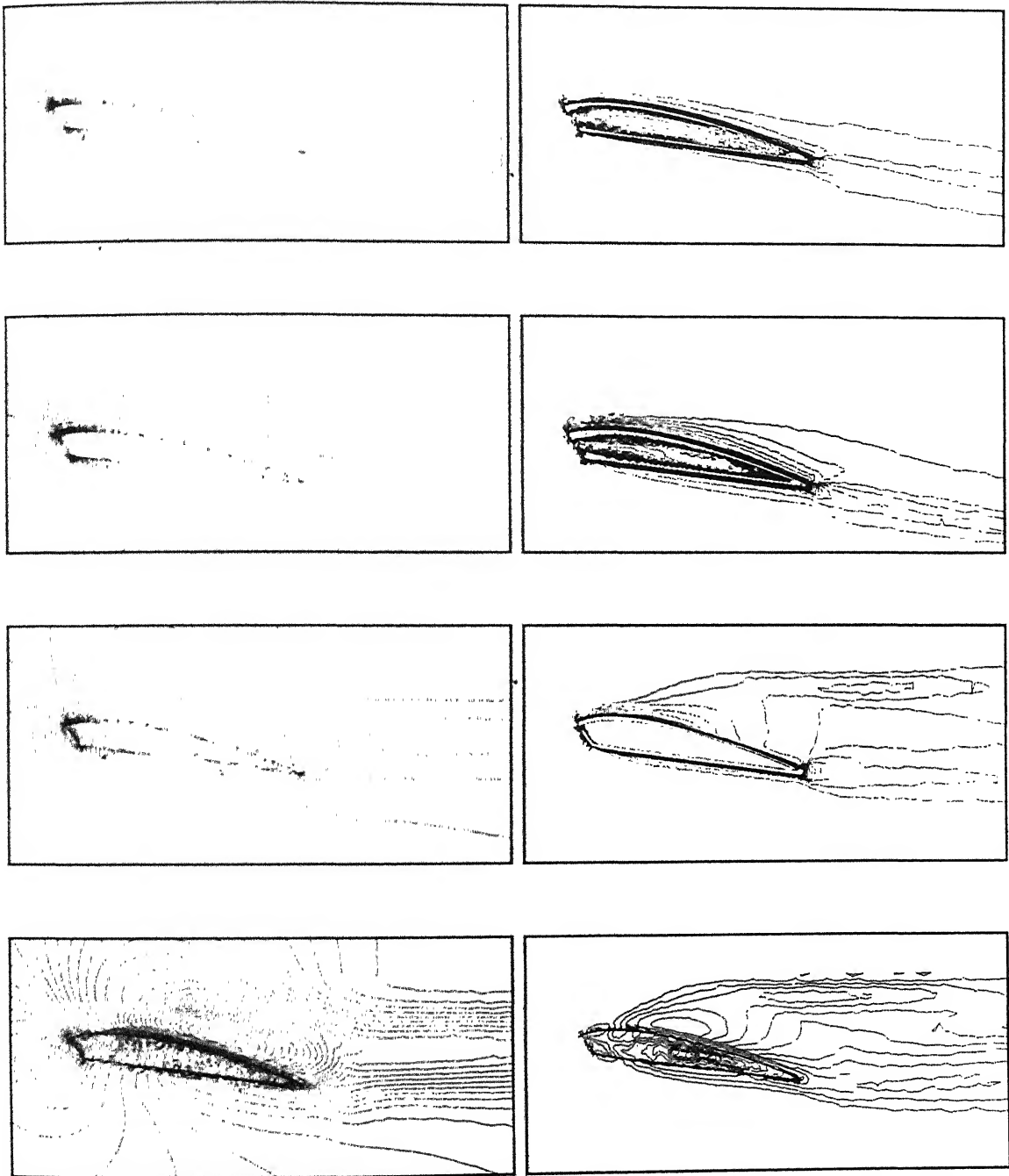


Figure 36:  $Re = 10^6$  turbulent flow past a Five cell ram-air parachute with Clarck-Y section: pressure(left) and z-vorticity(right) at mid span, quarter span, wing tip and close to wing tip away from the parachute surface.

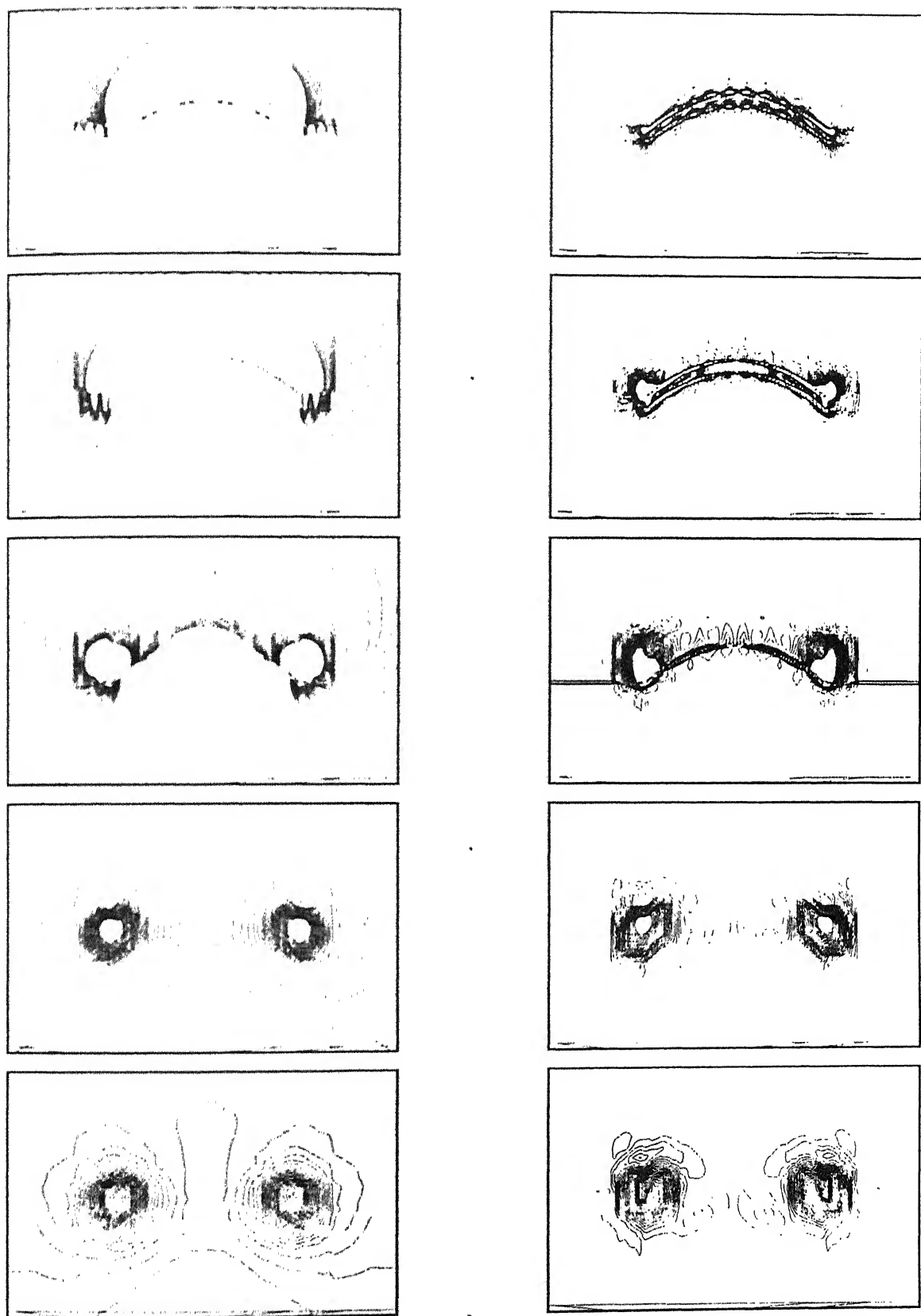


Figure 37:  $Re = 10^6$  turbulent flow past a Five cell ram-air parachute with Clark-Y airfoil. The left column shows velocity magnitude contours (right) at various y-z sections. The location of the

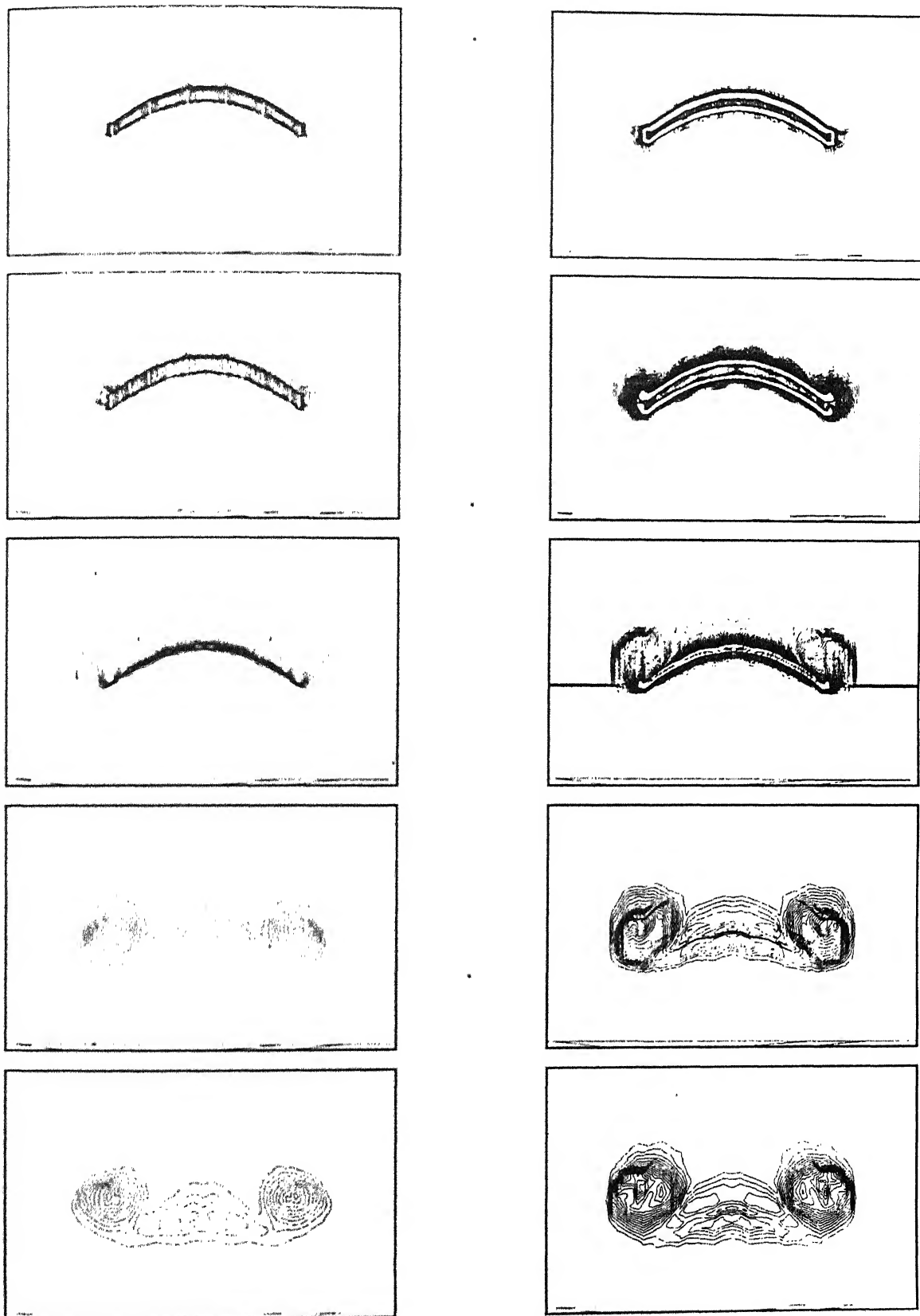


Figure 38:  $Re = 10^6$  turbulent flow past a Five cell ram-air parachute with Clark-Y airfoils. Left column shows velocity magnitude ( $u$ ) and right column shows vorticity magnitude at various  $y-z$  cross-sections.

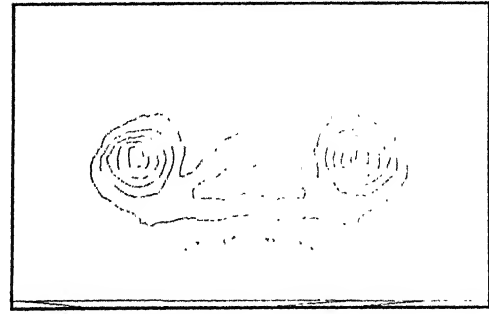
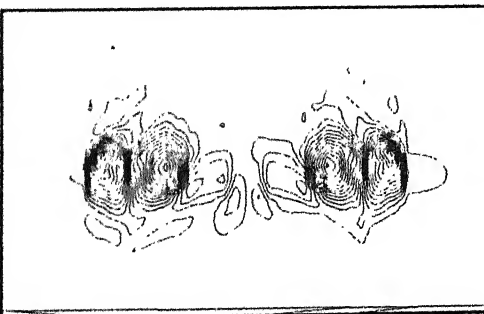
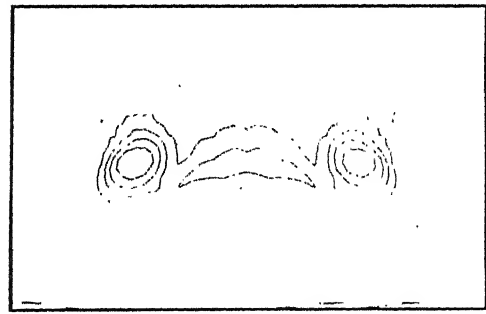
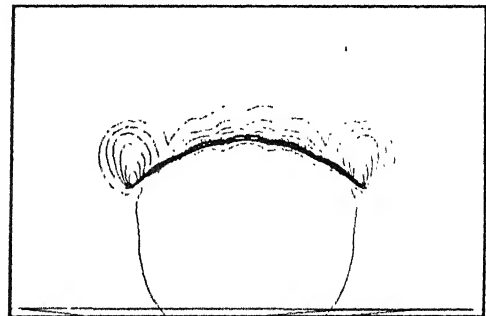
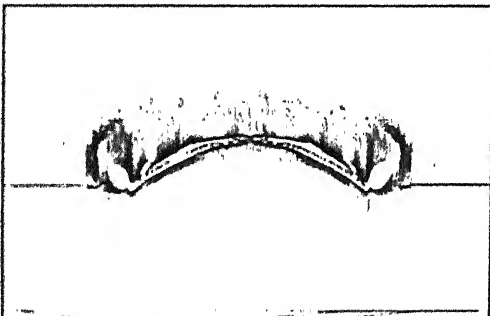
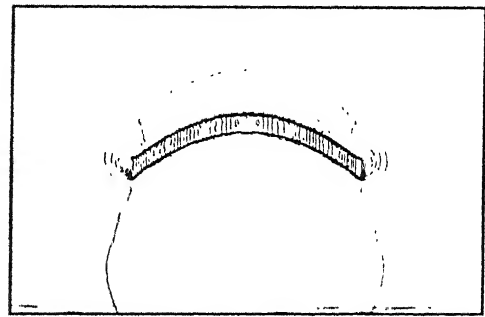
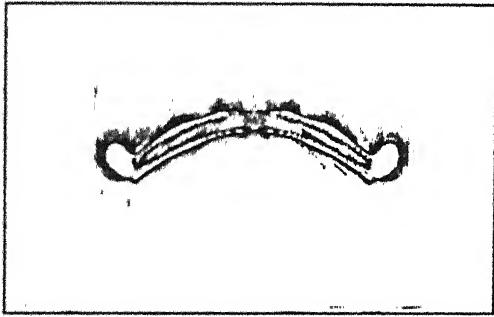
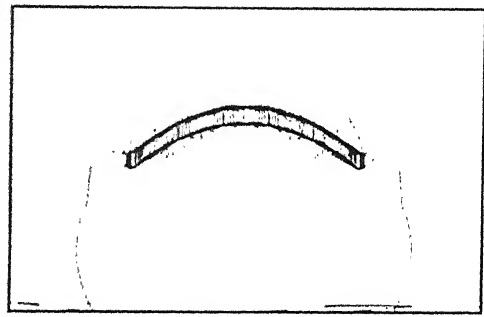
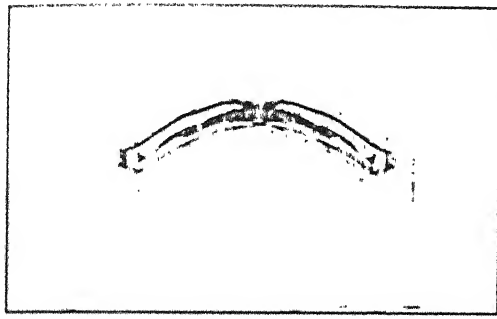


Figure 39:  $Re = 10^6$  turbulent flow past a Five cell ram-air parachute with Clark-Y section: y-vorticity(left) and z-vorticity(right) at various y-z sections. The location of the various section from top to bottom are  $x/c = -0.1, 0.5, 1.0, 2.0$  and  $3.0$ . The origin is at the leading edge of basic airfoil without cut.

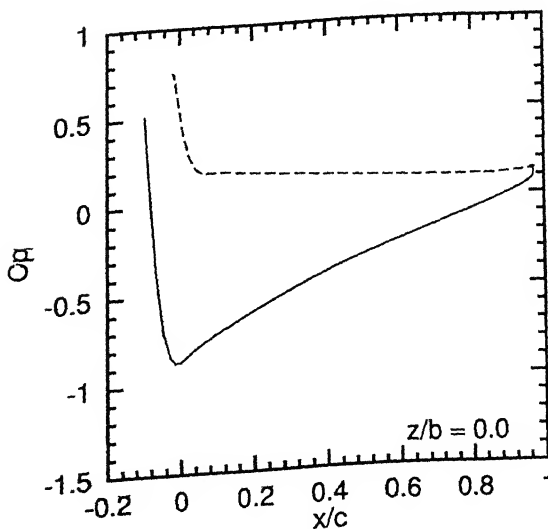
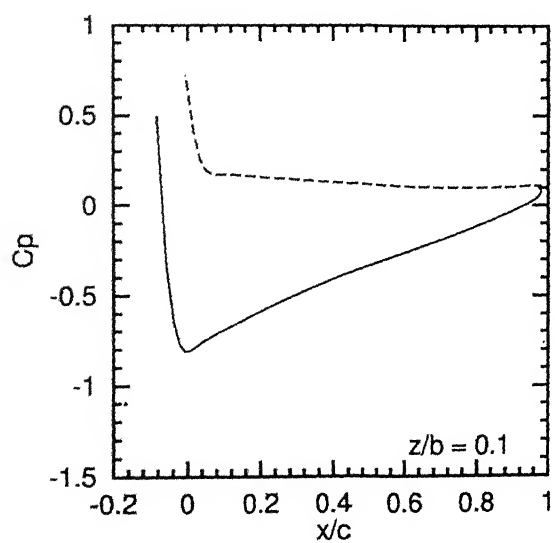
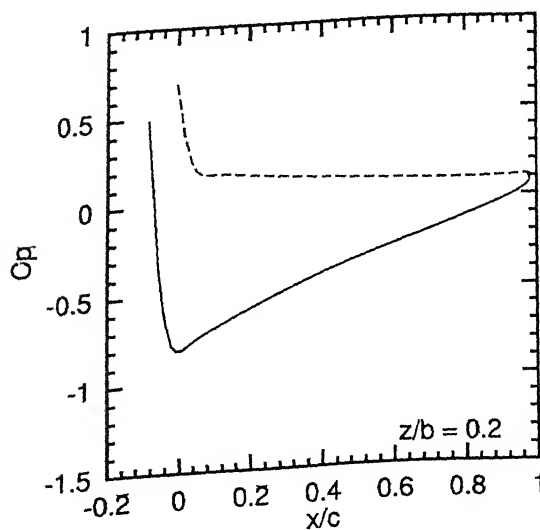
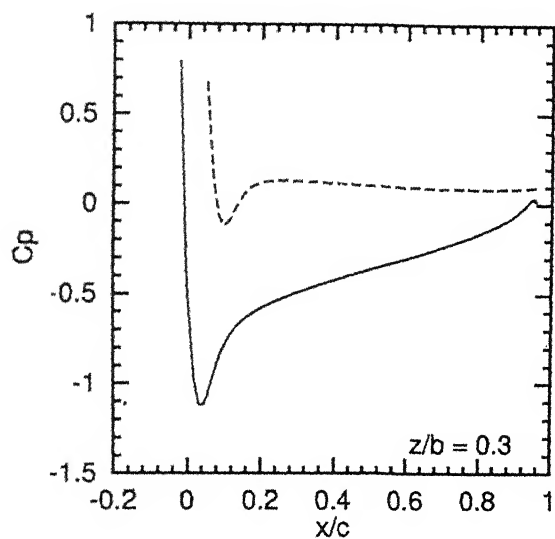
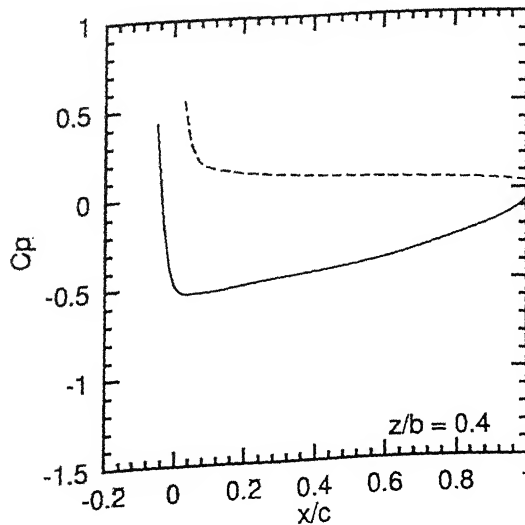
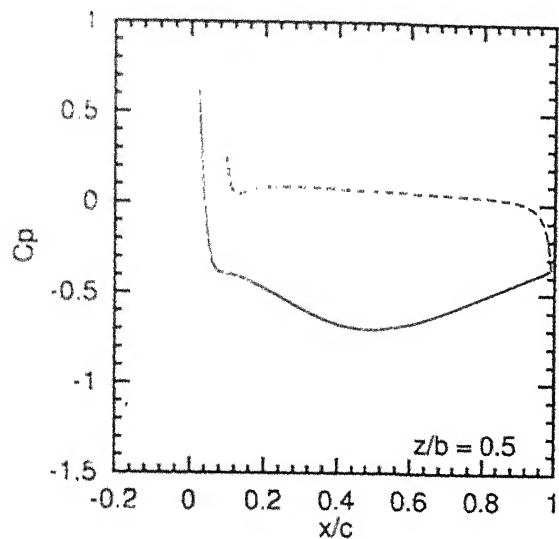


FIG. 10.  $Re = 10^6$  turbulent flow past a Five cell ram-air parachute with Clark-Y airfoil. Pressure coefficient along the



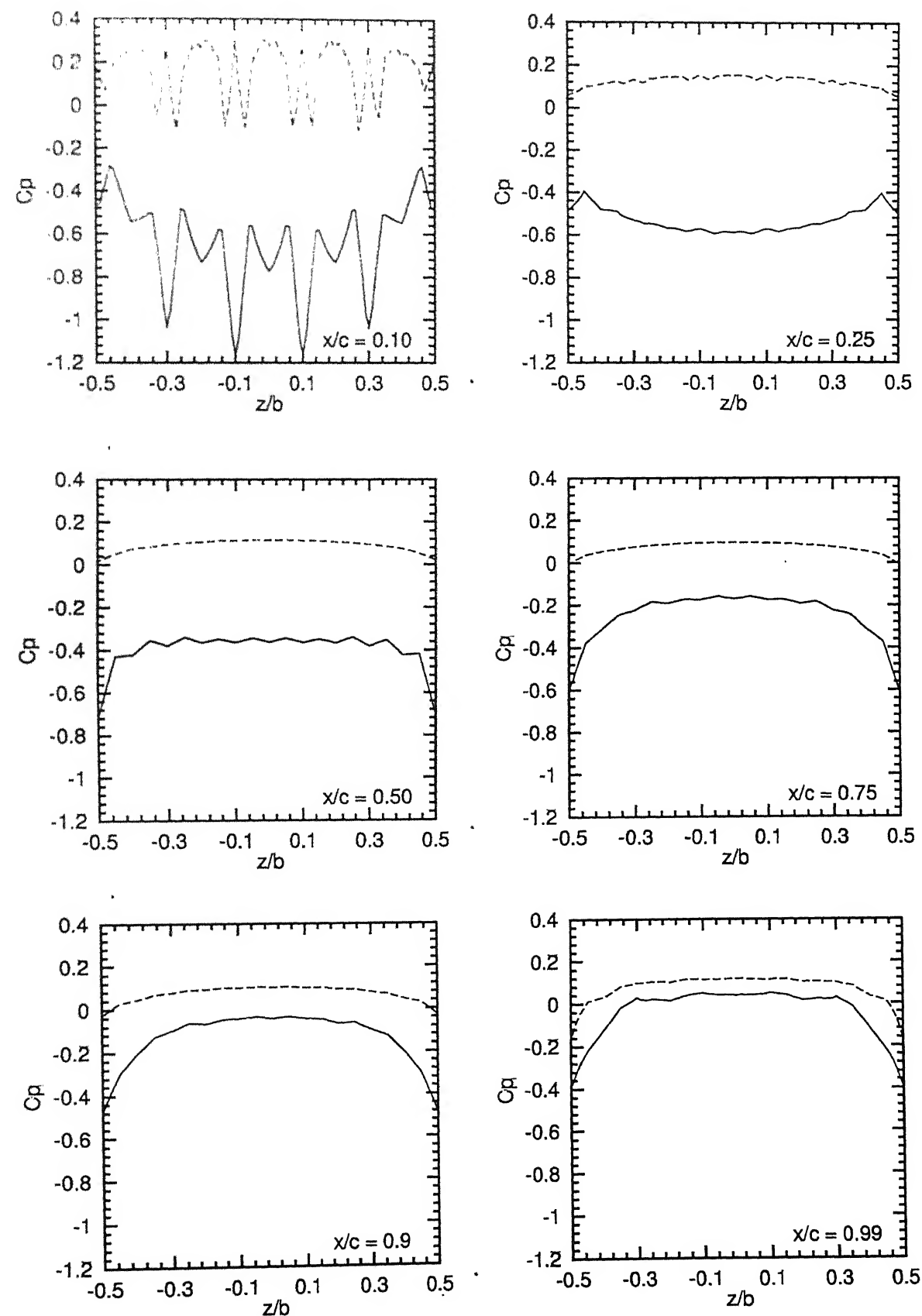


Figure 41:  $Re = 10^6$  turbulent flow past a Five cell ram-air parachute with Clark-Y

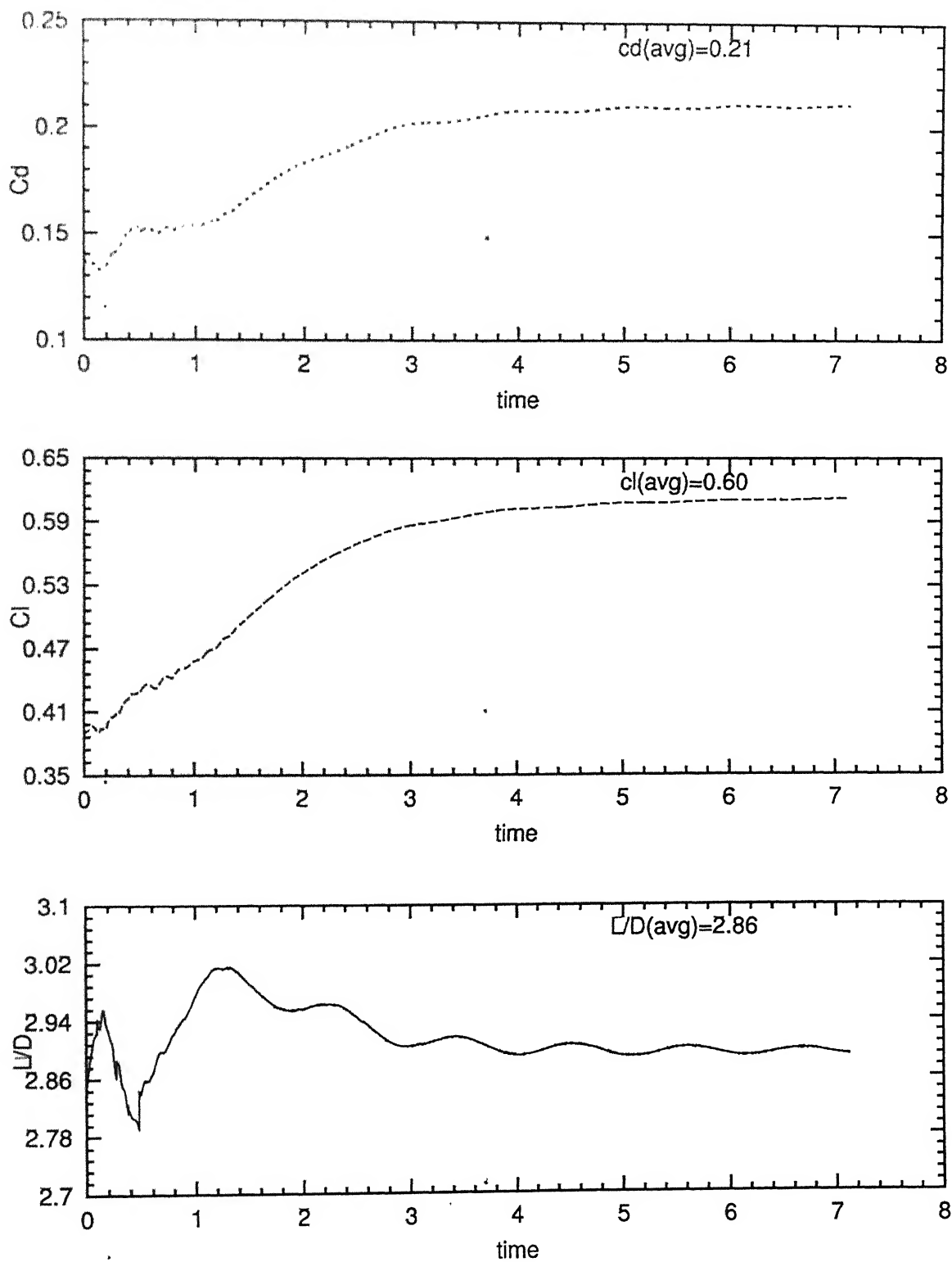


Figure 42:  $Re = 10^6$  turbulent flow past a five cell ram-air parachute with Clark-Y section: time histories of lift and drag coefficients and lift/drag ratio.

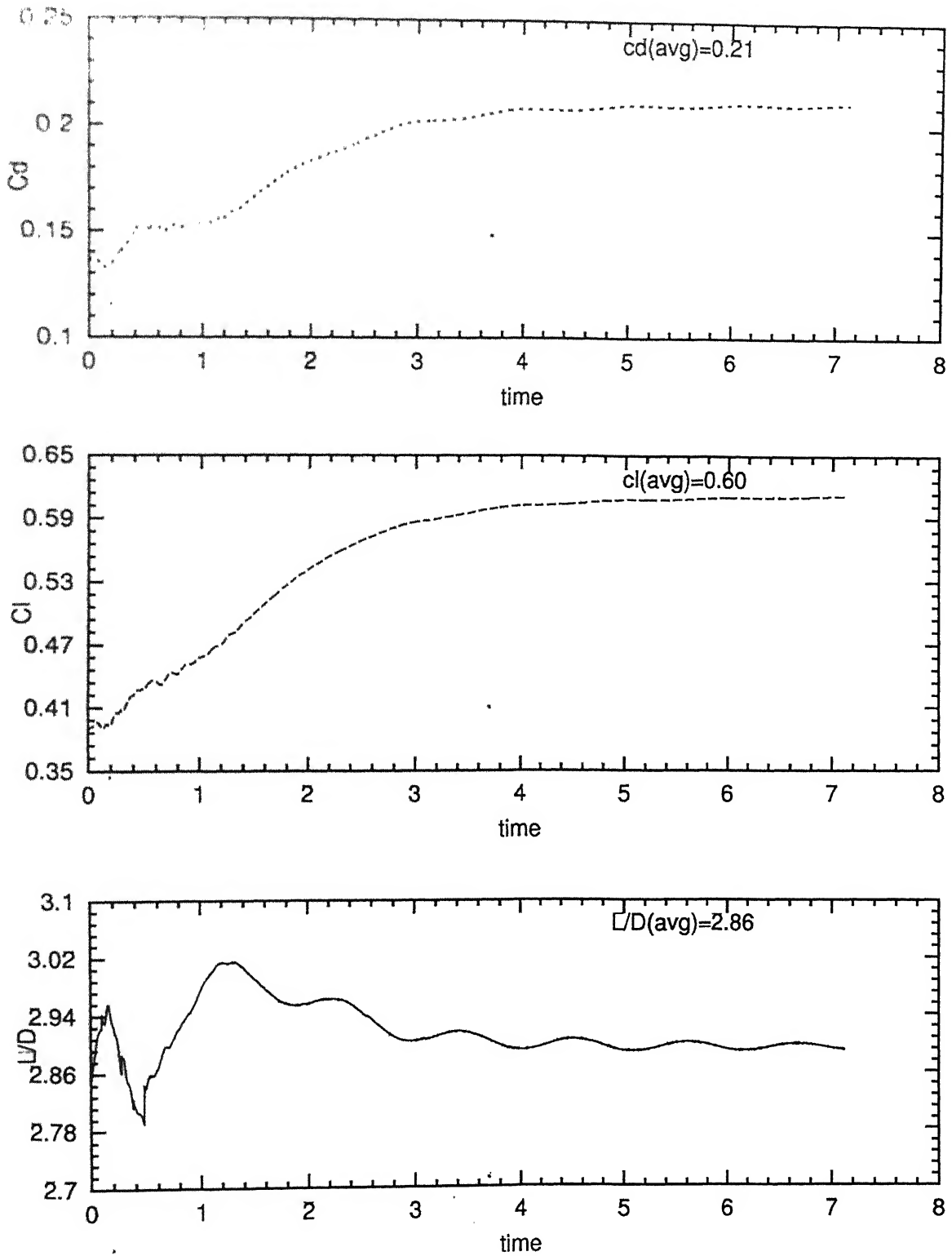


Figure 42:  $Re = 10^6$  turbulent flow past a five cell ram-air parachute with Clarck-Y section: time histories of lift and drag coefficients and lift/drag ratio.

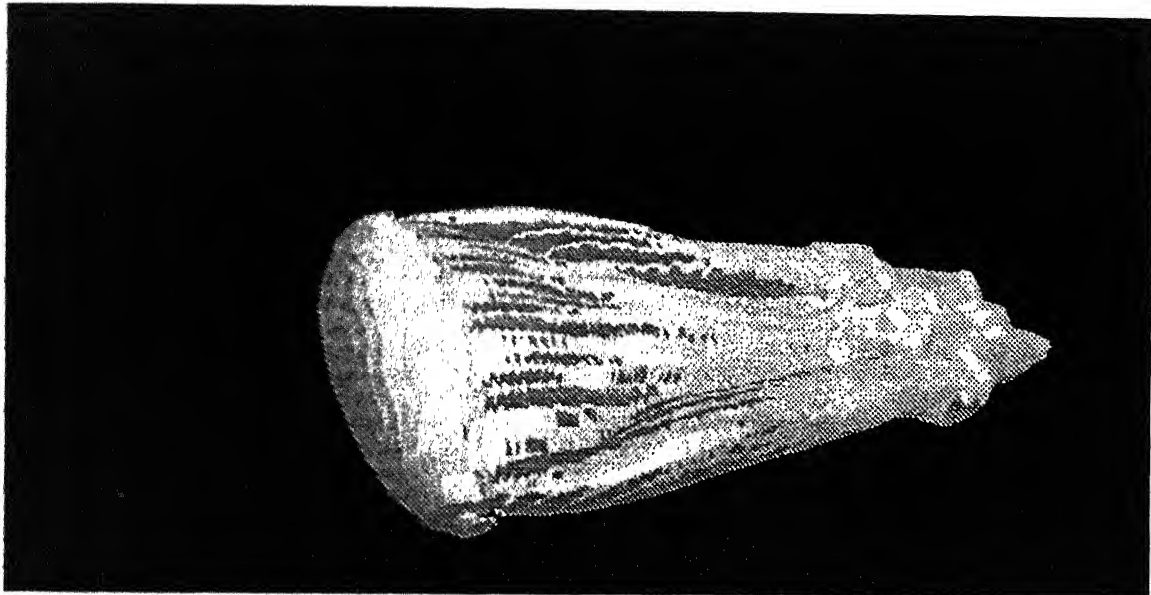


Figure 43:  $Re = 10^6$  turbulent flow past a five cell ram-air parachute with Clarck-Y section: isosurface corresponding to magnitude of velocity = 0.95.

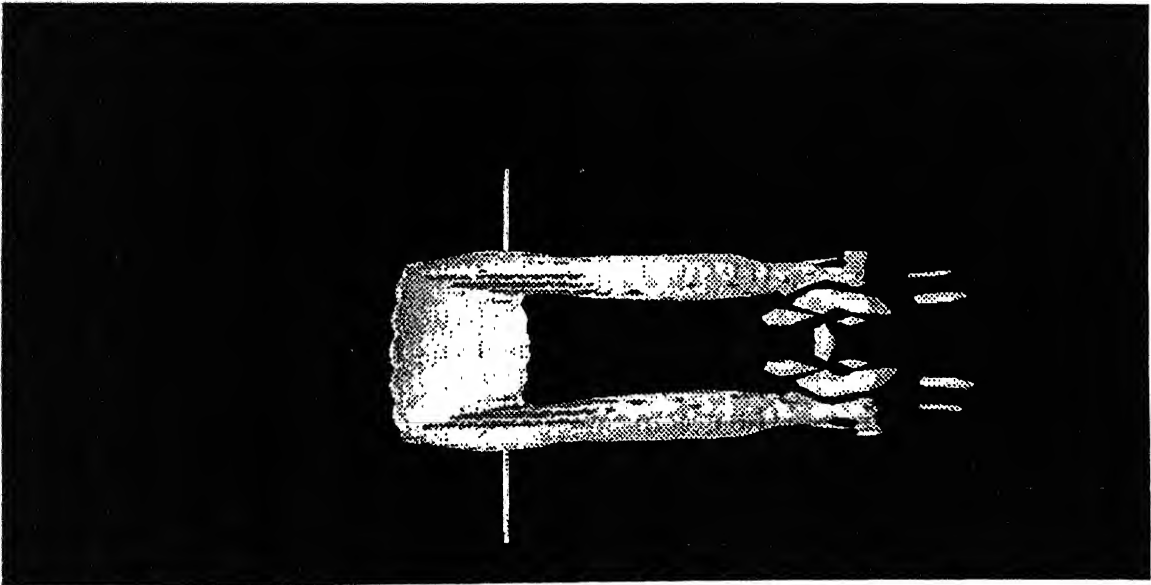


Figure 44:  $Re = 10^6$  turbulent flow past a five cell ram-air parachute with Clarck-Y section: isosurface corresponding to x-vorticity = 2.00.

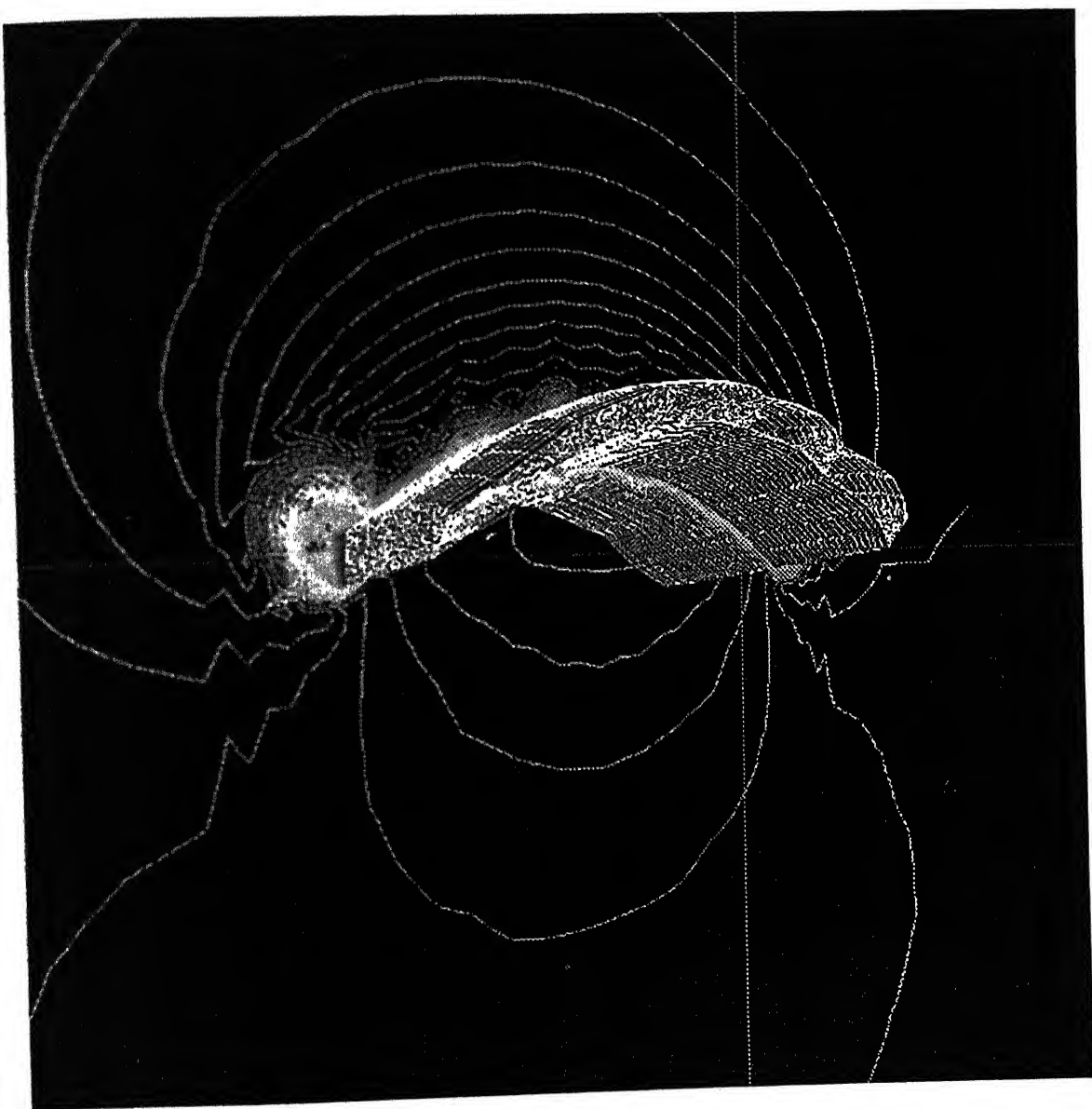


Figure 45:  $Re = 10^6$  turbulent flow past a five cell ram-air parachute with Clark-Y section: magnitude of velocity and parachute surface.

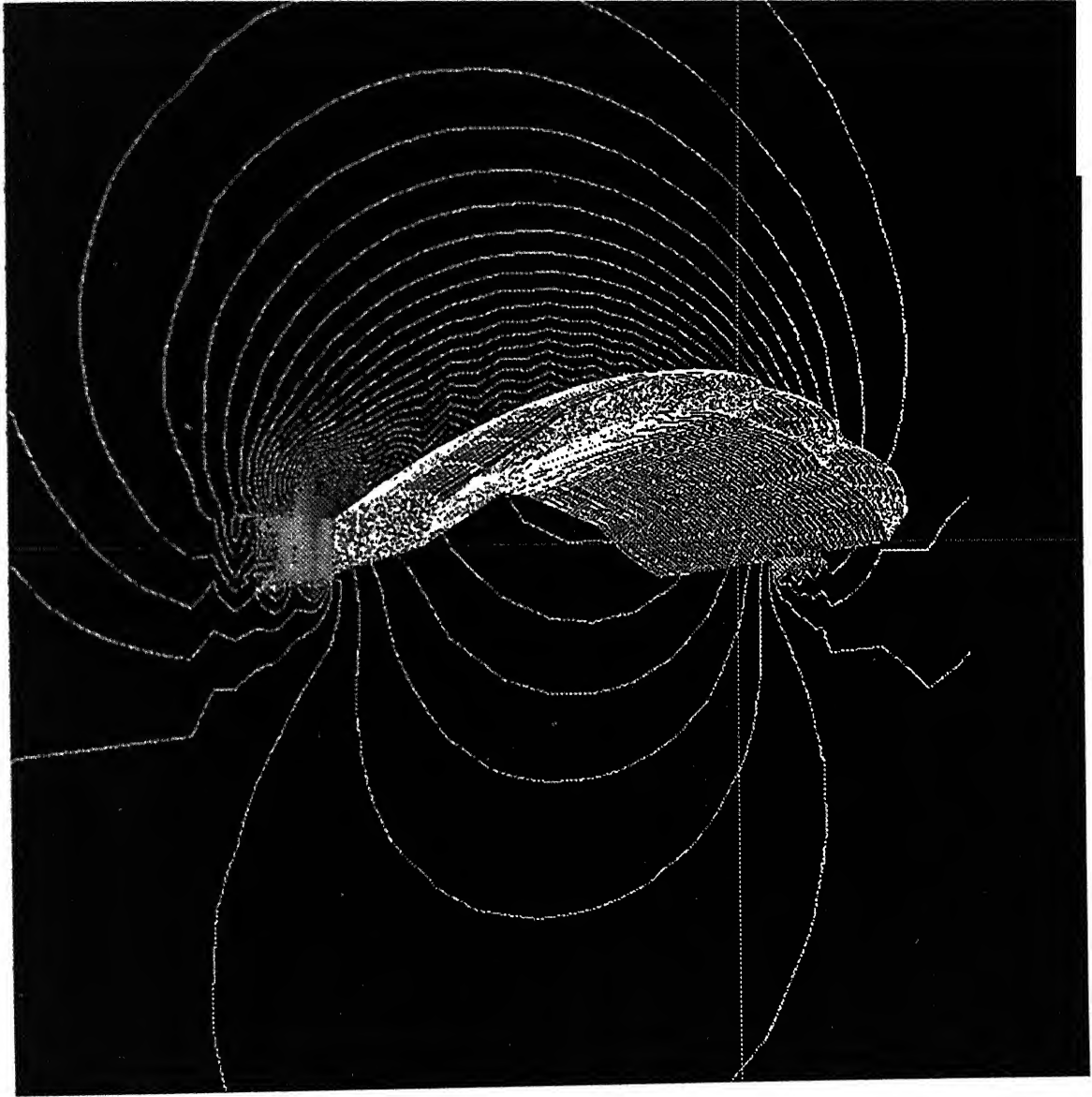


Figure 46:  $Re = 10^6$  turbulent flow past a five cell ram-air parachute with Clark-Y section: pressure and parachute surface.

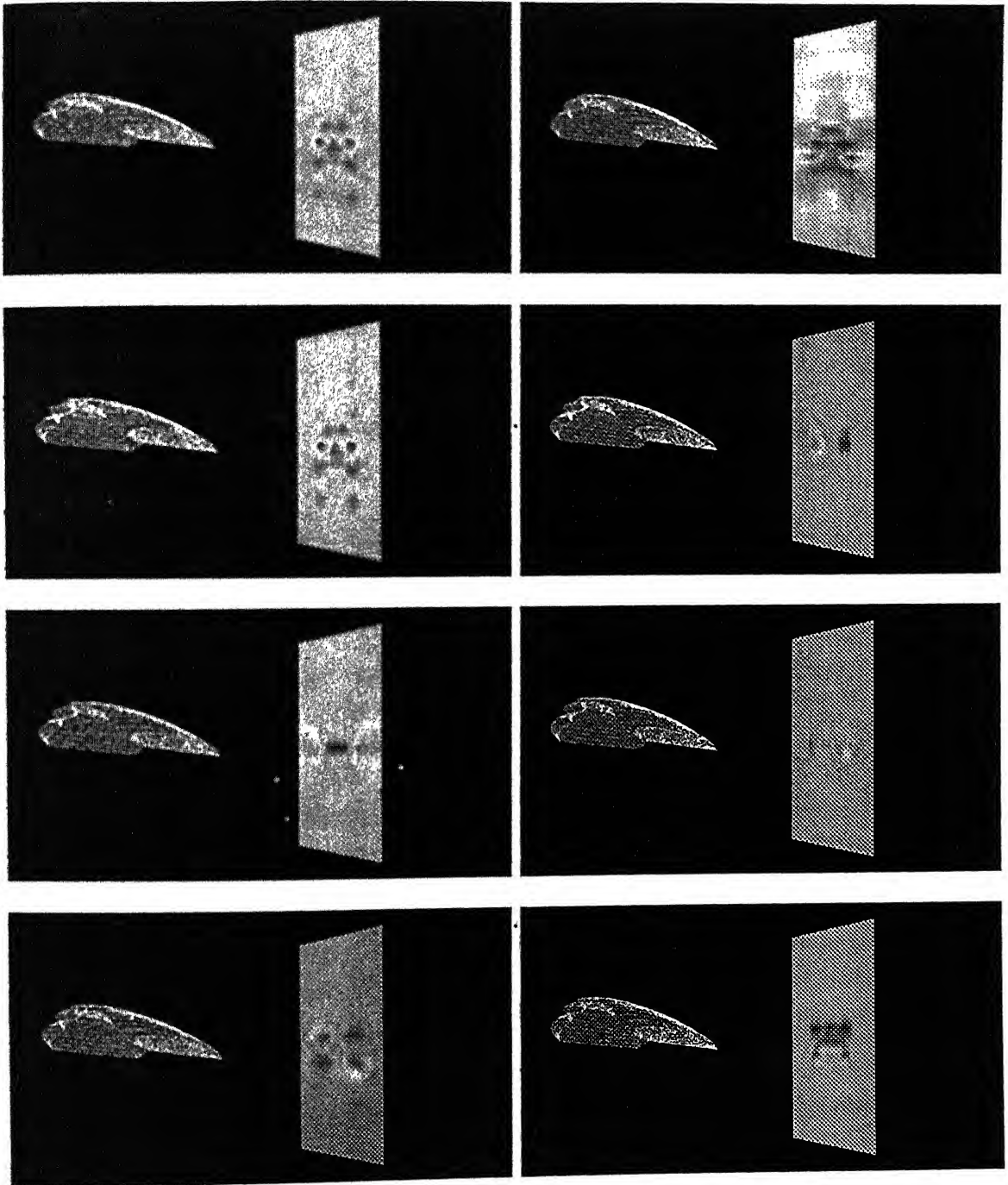


Figure 47:  $Re = 10^6$  turbulent flow past a five cell ram-air parachute with Clark-Y section, parachute fabric and shedding on y-z section plane away from the parachute surface, for various componenets: Left from top to bottom, magnitude of velocity, x-velocity, y-velocity, z-velocity, and Right from top to bottom pressure, x-vorticity, y-vorticity, z-vorticity.

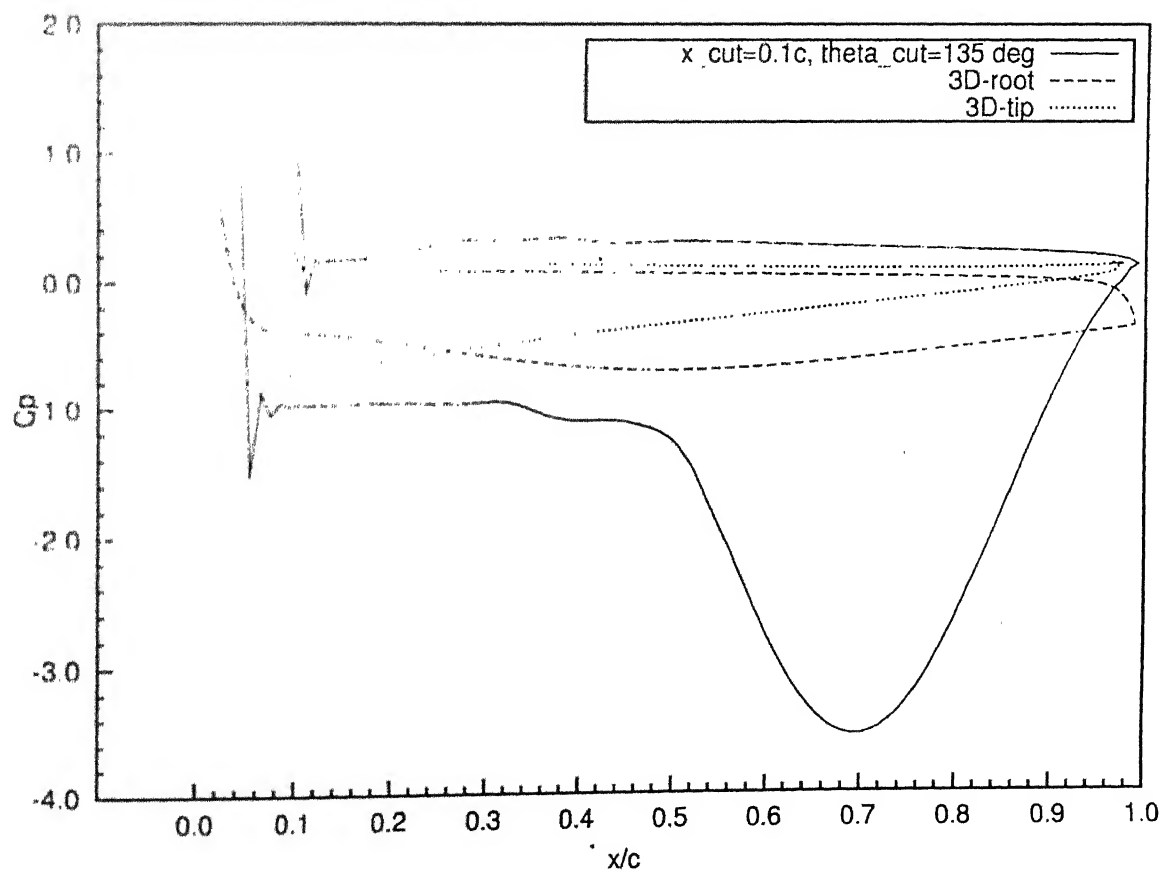


Figure 48: Turbulent flow ( $Re = 10^6$ ) past a Ram-air parachute: pressure coefficient variation on the outer surface for 2D Clark-Y parafoil along with 3D-tip and 3D-root section of Five-cell Ram-air parachute



A 141802



A141802